A COMPREHENSIVE COMBUSTION MODEL FOR BIODIESEL-FUELED ENGINE SIMULATIONS

by

Jessica L. Brakora

A dissertation submitted in partial fulfillment of the
requirements for the degree of

Doctor of Philosophy
(Mechanical Engineering)

at the
University of Wisconsin-Madison
2012

Date of final oral examination: 08/22/2012

The dissertation is approved by the following members of the Final Oral Committee:
Rolf D. Reitz, Professor, Mechanical Engineering
Christopher J. Rutland, Professor, Mechanical Engineering
David E. Foster, Professor, Mechanical Engineering
David A. Rothamer, Assistant Professor, Mechanical Engineering
Tracey Holloway, Associate Professor, Nelson Institute for Environmental Studies

Abstract

To date, much of the focus of engine models has been on the combustion of conventional fuels such as diesel and gasoline. Models for alternative fuels are available, but few are comprehensive, well-validated models that include accurate physical property data as well as a detailed description of the fuel chemistry. In this work, a comprehensive biodiesel combustion model was created for use in multi-dimensional engine simulations, specifically the KIVA3v-R2 code [1,2]. The model incorporates realistic physical properties in a vaporization model developed for multi-component fuel sprays and applies an improved mechanism for biodiesel combustion chemistry.

The main goals of this work were to create a well-validated model that can be used to guide future engine experiments fueled with biodiesel, and introduce a methodology that can be used when developing simulation models for new fuels. First, a representative kinetic mechanism was chosen. Researchers at Lawrence Livermore National Laboratory developed a detailed mechanism for two surrogate fuel species, methyl decanoate (MD) and methyl-9-decenoate (MD9D), capable of representing the saturated and unsaturated methyl ester components of real biodiesel fuel. Using a combination of the Directed Relation Graph method, isomer lumping, and limited reaction rate adjustments, the mechanism was reduced from 3299 species to 85 species, making it a more appropriate size for multi-dimensional simulations. The reduced mechanism accurately predicted ignition delay times of the detailed mechanism over a range of engine-specific operating conditions.

Next, the current physical property information for the five methyl ester components of biodiesel was added to the KIVA library. Spray simulations were performed to ensure that the KIVA models adequately reproduce the liquid penetration observed in biodiesel spray experiments. Distillation curves were created to ensure the fuel vaporization process was comparable to available data.

To validate the model under realistic engine operating conditions, two biodiesel experiments were chosen that cover a range of topics of interest related to biodiesel combustion. First, a low-speed, high-load, conventional combustion experiment was simulated and the model was able to predict the performance and NOx formation seen in the experiment. The mechanism was found to be inadequate for low-temperature combustion and a new biodiesel chemistry strategy was implemented utilizing n-heptane to improve ignition behavior. A second reduction was performed as well, further reducing the mechanism to 69 species. The high-speed, low-load, low-temperature combustion conditions were successfully modeled using the new strategy and the HC, CO, NOx, and fuel consumption were well-predicted for a sweep of injection timings. Also, comparisons were made between the results of biodiesel composition (palm vs. soy) and fuel blends (neat vs. B20). The model effectively reproduced the trends observed in the experiments including a *reduction* in NOx with neat biodiesel at these conditions.

Rolf D. Reitz, Professor, Mechanical Engineering Date

Acknowledgements

This work would not have been possible without the encouragement, guidance, patience and wisdom of my advisor, Rolf Reitz. Thank you for seeing my potential and giving me an opportunity to be part of the prestigious Engine Research Center. I owe a huge debt to my committee members as well. Thank you Chris Rutland, Dave Foster, Dave Rothamer and Tracey Holloway for the time you spent on your committee duties and, more importantly, for your support throughout my academic career.

Thank you to the ERC ladies who reminded me that engine research isn't just a boys club: Laine (Stager) Schrewe, Dr. Caroline Genzale, Helene Gorius, Qi Jiao, Ting Liang, Dipa Das Adhikary, and Jamie Jennings. Caroline, in particular, is a constant pillar of support, always encouraging me to be proud of my work and confident in my abilities.

And thanks to the ERC guys: Dr. Achuth Munnannur, Dr. Siddhartha Banerjee, Dr. Gokul Vishwanathan, Dr. Will (+ Deanne!) Glewen, Chris Meyer (+ Heather Wentler!). Reed Hansen, Derek Splitter, Huy Tran, Matt Blessinger, Cory Adams, and Dave Heuwetter. A special shout out to Sage Kokjohn and Adam Dempsey who's "Fox News Updates" will always hold a special place in my ERC memories.

Thanks to my sister, Kelley VanGemert, for helping me through my semi-annual wardrobe crisis, and to my parents, Deb and Bill Nichols and John and Julie Brakora, who were the first to encourage me to have big goals and remained supportive throughout my *long* college career. Finally, thank you to my boyfriend, Clint LeaTrea. No one has helped me through this process more than you. You are my favorite everything.

Table of Contents

List of Figures

List of Tables

Nomenclature

General Abbreviations (KIVA names shown in parentheses)

A	Pre-Exponential Factor in Arrhenius Expression
aTDC	After Top Dead Center
b	Exponential Rate Parameter in Arrhenius Expression
B_0	Breakup Size Constant, KH Spray Breakup Model (balpha)
B_1	Breakup Time Constant, KH Spray Breakup Model (cnst22)
BX	Biodiesel Blend with X Percent Biodiesel by Volume
C_3	Breakup Size Constant, RT Spray Breakup Model (cnst3rt)
CAD	Crank Angle Degrees
CAFE	Corporate Average Fuel Economy
CFD	Computational Fluid Dynamics
CI	Compression-Ignition
Cp	Specific Heat, $Cp°$ for Standard State
E	Activation Energy in Arrhenius Expression
EGR	Exhaust Gas Residual
EPA	Environmental Protection Agency
ERC	Engine Research Center
EVO	Exhaust Valve Opening
EVC	Exhaust Valve Closure
H	Enthalpy, $H°$ for Standard State
HCCI	Homogeneous Charge Compression Ignition
HRR	Heat Release Rate
IMEP	Indicated Mean Effective Pressure
IVC	Intake Valve Closure
IVO	Intake Valve Opening
k	Arrhenius Reaction Rate Constant
K3R2	KIVA3V-Release 2 Combustion Model
Kc	Equilibrium Constant in Concentration Units

Kp	Equilibrium Constant in Pressure Units
L_b	Breakup Length in KH-RT Hybrid Spray Breakup Model (distant)
LHV	Lower Heating Value
LLNL	Lawrence Livermore National Laboratory
LTC	Low Temperature Combustion
NHTSA	National Highway Traffic Safety Administration
P	Pressure
PCCI	Premixed Charge Compression-Ignition
PPM	Parts Per Million
PRF	Primary Reference Fuel
q	Rate of Progress Variable
r_o	Radius of the Parent Droplet
Rc	Universal Gas Constant
RCCI	Reactivity-Controlled Compression-Ignition
S	Entropy, S° for Standard State
SCORE	Sandia Compression-Ignition Optical Research Engine
SI	Spark-Ignition
SOI	Start of Ignition
SOC	Start of Combustion
T	Temperature
ULSD	Ultra Low Sulfur Diesel
V	Volume
W	Molecular Weight
X	Molar Concentration

Chemical Symbols and Emissions Abbreviations (CHEMKIN names shown in parentheses)

CO	Carbon Monoxide
CO_2	Carbon Dioxide
CH_2O	Formaldehyde
C_2H_2	Acetylene
C_7H_{16}	Normal Heptane, n-Heptane (nc7h16)
$C_{14}H_{30}$	Tetradecane

$C_{17}H_{34}O_2$	Methyl Palmitate (mpalm)
$C_{19}H_{38}O_2$	Methyl Stearate (mstear)
$C_{19}H_{36}O_2$	Methyl Oleate (molea)
$C_{19}H_{34}O_2$	Methyl Linoleate (mlinl)
$C_{19}H_{32}O_2$	Methyl Linolenate (mlinln)
CX:Y	Methyl Ester with X Carbons in Chain and Y Double Bonds
HC	Hydrocarbons, General
H_2O	Water
H_2O_2	Hydrogen Peroxide
HO_2	Hydroxyl Radical
NO	Nitrogen Oxide
NO_2	Nitrogen Dioxide
O_2	Oxygen Molecule
OH	Hydroxide Radical
NOx	Oxides of Nitrogen (NO + NO_2)
PM	Particulate Matter
M	Third Body
MB	Methyl Butanoate
MD	Methyl Decanoate
MD9D	Methyl-9-Decenoate
ME	Methyl Ethanoate
MF	Methyl Pentanoate
QOOH	Hydroperoxyalkyl Radical
R	Alkyl Radical

Greek Symbols

ϕ	Equivalence Ratio
ρ	Density
ν	Stoichiometric Coefficient
ω	Production Rate
σ	Surface Tension
τ	Breakup Time, KH Spray Breakup Model

Ω	Frequency
Λ	Wavelength

Chapter 1: Introduction

1.1 Motivation

The United States relies heavily on the combustion of fossil fuels as a source for its energy needs. Internal combustion engines are the dominant machines used to convert the fuel energy to useable power in both stationary (e.g., power plants, factories) and mobile (e.g., automobiles, farm and construction equipment) applications. Ideally, the hydrocarbon fuels in these machines would have access to the perfect amount of oxygen (i.e., “stoichiometric”) and be allowed ample time to completely oxidize to carbon dioxide (CO_2) and water (H_2O). However, this ideal is rarely achieved in engines, particularly the mobile engines of this research, where reaction times are limited to milliseconds, varying temperatures change reaction rates, and on-demand performance causes operating conditions to fluctuate lean or rich of stoichiometric. Inadequate conditions result in incomplete combustion and undesirable combustion products (i.e., pollutants). Hydrocarbons (HC), carbon monoxide (CO), particulate matter (PM), and oxides of nitrogen (NOx) are identified as the significant air pollutants from mobile sources and strict regulations of these emissions have been set forth by the United States government [3].

The U.S. Environmental Protection Agency (EPA) established Tier I and Tier II emissions standards for light-duty engines through the Clean Air Act Amendments of 1990 [4]. In two stages between 1994 and 2009, light-duty diesel engine manufacturers were required to reduce their NOx and soot emissions by over 90%. In 2000, the EPA signed emissions standards for heavy-duty engines as well. These standards required a 90% reduction in NOx and soot between 2007 and 2010 [5]. While CO_2 is a desirable product of efficient combustion, it is also a greenhouse gas. To address this issue, the EPA and the Department of Transportation's National Highway Traffic Safety Administration (NHTSA) adopted greenhouse gas rules for both light-duty and heavy-duty engines [6]. The rules affect model years 2012 through 2016 for light-duty [7] and model years 2014 to 2018 for heavy-duty engines [8]. In conjunction with the CO_2 regulations, the Corporate Average Fuel Economy (CAFE) standards have also increased; each with the goals of achieving a fleet-wide fuel economy of nearly 35 miles per gallon by 2020 [9]. Both the CAFE and CO_2 standards are efforts to reduce energy consumption and improve the efficiency (i.e., fuel economy) of mobile engines.

Exhaust emissions regulations drive much of the research and development for today's mobile engines. The higher efficiency of compression-ignition, or diesel, engines makes them an attractive alternative to the spark-ignition, or gasoline, as a means of reducing CO_2 and improving fuel economy. However, diesel engines have not significantly gained in popularity in the United States, partially due to the traditionally higher NOx and soot emissions with the conventional compression-ignition combustion process. This conventional strategy involves injection near top dead center (TDC), resulting in a relatively rich diffusion flame and high temperatures. These hot, rich conditions are ideal for NOx and PM (soot) formation. Diesel engine experiments performed in laboratory settings are used extensively to test new operating regimes and discover new strategies to reduce these emissions and also improve the efficiency of these engines.

Early experiments of Kamimoto and Bae [10] identified the NOx-soot trade-off for diesel engines and the small window of operating conditions available to simultaneously reduce NOx and soot. This operational window, characterized by low equivalence ratios and low temperatures, is denoted the low temperature combustion (LTC) regime. The LTC strategy is generally achieved with high levels of exhaust gas recirculation (EGR) to reduce temperatures [11,12]. Other strategies have been identified that focus more on reducing the equivalence ratio of the combustion mixture. These include homogeneous charge compression-ignition (HCCI), which uses early injection timings to create a nearly-homogeneous mixture, and partially-premixed charge compression-ignition (PCCI), which uses two injections (one early and one at conventional diesel injection timings) to create a highly-mixed charge.

Experimental engine research is often performed using metal engines, which can provide valuable performance and emissions data. Unfortunately, due to their restricted view, researchers can only hypothesize regarding spray behavior, or locations of key species formation and the onset of combustion. Optical access is possible by installing windows into the combustion chamber. Through use of sophisticated lasers and camera diagnostics, researchers can then “see” the spray or combustion event taking place inside the engine. Optical engines have helped researchers make valuable contributions to our understanding of diesel spray and combustion processes [13-17]. However, such facilities are expensive and, like most experiments, set-up and data collection can be a time-consuming process. In this regard, computational models can play a significant role in engine development. Engine simulation results can be coupled with post-processing software to provide a view into the combustion chamber without modifying an experimental engine, while often reducing much of the time and expense associated with engine testing in the laboratory.

The KIVA3v-Release 2 (KIVA3v-R2) computational fluid dynamics (CFD) code is an updated version of one of the pioneer codes for engine simulations [1,2]. It is a combination of many sub-models that have been extensively validated against a variety of spray and engine experiments. A large number of the models within the KIVA3v-R2 code are designed for diesel combustion and these models have greatly contributed to our understanding of the processes occurring within the engine. Recently, the models have been used to identify optimal spray targeting [18-20], injection strategies [20-23], and piston geometries [24,25] to improve engine performance and reduced emissions. More recently, Kokjohn et al. [26,27] used computational modeling of two fuels to guide experiments that confirmed the benefits of an innovative reactivity-controlled compression-ignition (RCCI) strategy as a means of achieving very low emissions and improved efficiencies.

As new combustion strategies arise and computer capabilities improve, it is important to expand computational models by including a variety of fuel options, and a more realistic representation of fuels, both in terms of physical properties and chemistry. To date, much of the focus of engine models has been on the combustion of conventional fuels such as diesel and gasoline. Models for alternative fuels are available, but few are comprehensive, well-validated models that include accurate physical property data as well as a detailed description of the fuel chemistry.

1.2 Objective

The objective of this work is to create a comprehensive biodiesel combustion model for use in multi-dimensional engine simulations, specifically the KIVA3v-R2 code [1,2]. The model will incorporate realistic physical properties in a vaporization model developed for multi-component fuel sprays. It will also apply an improved mechanism for biodiesel combustion chemistry. While this work focuses on validating a model for biodiesel fuel, the methodology introduced next, and described in detail in the following chapters, is applicable to the development of *any* new fuel model. A second, equally important goal of this work is to serve as a guide for researchers who wish to develop new simulation models for future fuels.

Model development was achieved in three stages. First, detailed reaction mechanisms were investigated to improve accuracy of a previous biodiesel fuel chemistry model. Once an appropriate mechanism was identified, it was necessary to reduce the number of species in order to make it applicable to CFD simulations. Homogeneous reactor studies were simulated using the programs CHEMKIN [28] and Senkin [29] to assess the ignition timing and species concentrations of the reduced mechanism compared to those predicted by the detailed mechanism. By applying the mechanism in these completely mixed environments, chemistry was isolated from the physical processes (i.e., spray) and properties of the fuel.

Next, current biodiesel physical property information for the five components of biodiesel was added to the KIVA library. Once the fuel was accurately described, spray simulations were performed to ensure that the KIVA models adequately reproduced the behavior observed in biodiesel spray experiments. Non-reacting spray cases were modeled to assess the physical processes such as injection, break-up, and vaporization of the fuel. Comparisons were made between the model predictions and experimental results, and model inputs were adjusted to assess sensitivity to spray model parameters and fuel composition.

Once these individual models were validated, the comprehensive model was applied in engine simulations. To ensure effectiveness, the model must be able to reproduce results from a variety of biodiesel-fueled engine experiments. Two validation experiments were chosen to cover a range of topics of interest related to biodiesel combustion:

- Conventional and low-temperature combustion regimes
- NOx, soot, HC, and CO emissions
- Biodiesel-diesel blends
- Heavy- and light-duty engines
- High- and low-speed operation
- High- and low-load operation
- Injection timing and combustion phasing
- Effect of exhaust gas recirculation (EGR)

Chapter 2: Literature Review

2.1 Simulation Models

2.1.1 CHEMKIN II Chemistry Solver

The CHEMKIN II chemistry solver is a Fortran-based software package that assists in the solution of problems related to elementary gas-phase chemical kinetics [28]. The solver consists of a library of subroutines used in conjunction with another program that describes the governing equations related to the problem. The CHEMKIN solver is called to calculate the equations of state, thermodynamic properties, and chemical production rates requested by the main program.

In order to use CHEMKIN, a kinetic reaction mechanism must be provided which includes the species, reactions, and reaction rates that describe the chemistry related to the fuel oxidation. The production rate of the kth species, ω_k, is found by summing the rate-of-progress variables for all the reactions that involve the kth species, as shown in Equation (1),

$$\omega_k = \sum_{i=1}^{I} \nu_{k,i}\, q_i \tag{1}$$

where ν_{ki} is the difference between stoichiometric coefficients for the products (double quotes) and the reactants (single quotes) as follows:

$$\nu_{k,i} = \nu''_{k,i} - \nu'_{k,i} \tag{2}$$

The rate-of-progress variable, q_i, for the ith reaction is found from the difference between the forward and reverse rates of reaction as seen in Equation (3).

$$q_i = k_{f,i}\prod_{k=1}^{K}[X_k]^{\nu'_{k,i}} - k_{r,i}\prod_{k=1}^{K}[X_k]^{\nu''_{k,i}} \tag{3}$$

In the above equation, $[X_k]$ is the molar concentration of the k^th^ species, and k_{fi} and k_{ri} are the forward and reverse rate constants for the i^th^ reaction, respectively. The forward rate constants are assumed to be described by the Arrhenius rate expression:

$$k_{f,i}=A_i T^{b_i} e^{\frac{-E_i}{R_c T}} \tag{4}$$

where A_i is the pre-exponential factor, b_i is the temperature exponent, and E_i is the activation energy for the i^th^ reaction; T and R_c are the temperature and universal gas constant, respectively. It should be noted that the rate constant's units vary depending on the order of the given reaction. For example, the reaction rate for species A (i.e., d[A]/dt) might depend on species B and C as $k_A[B]^m[C]^n$ where the reaction order is m+n and brackets ([ ]) signify a concentration. Obtaining values for the three rate parameters A_i, b_i, and E_i, requires an extensive knowledge of molecular theory and application of advanced numerical programs and techniques [30]. Once discovered, the rate parameters are included as essential components of the mechanism.

The reverse rate constant is related to the forward rate constant through the equilibrium constant, K_{ci}, where

$$k_{r,i}=\frac{k_{f,i}}{K_{c,i}} \tag{5}$$

The equilibrium constant above, which is given in units of concentration, is found from Equation (6), which is simply a conversion from the equilibrium constant in units of pressure, K_{pi}, using the atmospheric pressure, P_{atm}.

$$K_{c,i}=K_{p,i}\left(\frac{P_{atm}}{R_cT}\right)^{\sum_{k=1}^{K}\nu_{k,i}} \tag{6}$$

K_{pi} is easily calculated from thermodynamic properties using Equations (7)-(9), where S_k and H_k are the species entropy and enthalpy, respectively.

$$K_{p,i}=e^{\left(\frac{\Delta S_i^o}{R_c}-\frac{\Delta H_i^o}{R_cT}\right)} \tag{7}$$

$$\frac{\Delta S_i^o}{R_c}=\sum_{k=1}^{K}\left(\nu_{k,i}\frac{S_k^o}{R_c}\right) \tag{8}$$

$$\frac{\Delta \mathrm{H}_i^o}{R_cT}=\sum_{k=1}^{K}\left(\nu_{k,i}\frac{H_k^o}{R_cT}\right) \tag{9}$$

In order to determine the appropriate standard state specific heat (C_{pk}), enthalpy (H_k), and entropy (S_k) for each species in the mechanism, a thermodynamic database is also included. The database contains seven coefficients that establish the polynomial curve-fits for each of two specified temperature ranges. The following equations show how the seven coefficients are applied in the equations for specific heat, enthalpy, and entropy.

$$\frac{C_{p,k}^o}{R_c}=a_{1,k}+a_{2,k}T+a_{3,k}T^2+a_{4,k}T^3+a_{5,k}T^4 \tag{10}$$

$$\frac{H_k^o}{R_cT}=a_{1,k}+\frac{a_{2,k}}{2}T+\frac{a_{3,k}}{3}T^2+\frac{a_{4,k}}{4}T^3+\frac{a_{5,k}}{5}T^4+\frac{a_{6,k}}{T} \tag{11}$$

$$\frac{S_k^o}{R_c}=a_{1,k}\ln(T)+a_{2,k}T+\frac{a_{3,k}}{2}T^2+\frac{a_{4,k}}{3}T^3+\frac{a_{5,k}}{4}T^4+a_{7,k} \tag{12}$$

The structure of CHEMKIN can be seen in Figure 2-1. The CHEMKIN interpreter reads the kinetic reaction mechanism provided by the user and combines the information with that from the thermodynamic database. The interpreter creates a new binary file that will be used to link this information to the CHEMKIN library. This library consists of gas-phase subroutines that contain the equation of state, and thermodynamic relationships associated with the species and reactions found in the mechanism. This library is used in conjunction with an application code to solve the given reacting flow problem.

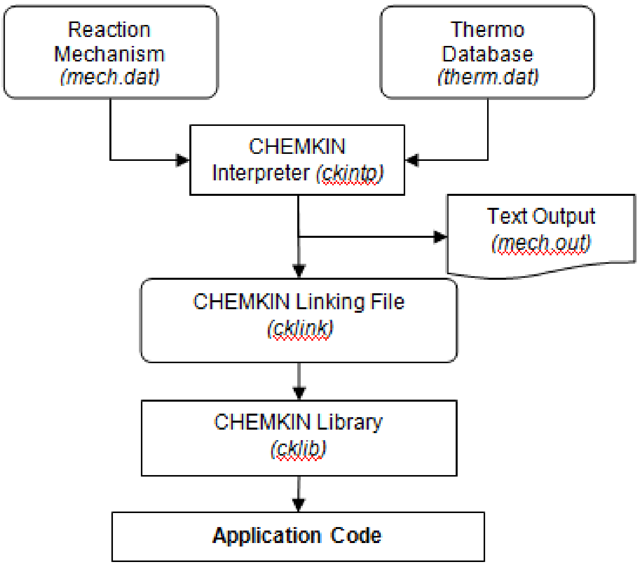

Figure 2-1: Structure of the CHEMKIN package [29]

2.1.2 SENKIN

Senkin is a Fortran-based application code that makes use of the CHEMKIN library described previously. The program is designed to analyze homogeneous gas mixtures in closed systems [29]. Six systems are available for analysis: (a) adiabatic constant pressure, (b) adiabatic constant volume, (c) adiabatic time-dependent volume, (d) constant pressure and temperature, (e) constant volume and temperature, and (f) time-dependent pressure and temperature. Once the problem is specified, Senkin uses the same differential equations as those in the CHEMKIN-II solver [28] to provide species and temperature histories of the mixture based on the given mechanism.

Each of the available Senkin systems is considered a closed environment in which no mass crosses the boundary. Therefore, the total mass of the mixture remains constant and does not change with time. The mass of individual species, however, changes within the system based on the following equation:

$$\frac{dm_k}{dt} = V\omega_k W_k \tag{13}$$

where t is time, ω_k is the molar production rate of the k^{th} species, W_k is the molecular weight of the k^{th} species and V is the volume of the system. Depending on the system chosen for analysis, Equation (13) can be used to derive the energy equation and various other thermodynamic relationships.

2.1.3 CHEMKIN-PRO

CHEMKIN-PRO is a commercial software package that couples a variety of reacting flow applications with the CHEMKIN II library in a user-friendly Graphical User Interface (GUI) environment. The solver algorithms are also upgraded from the original CHEMKIN package to improve efficiency for complex models that include large kinetic mechanisms. Of notable interest for this work, CHEMKIN-PRO includes a Reaction Path Analyzer post-processing feature that creates an interactive visual display of the interconnections between species.

Figure 2-2 below shows an example of the display. The Reaction Path Diagram, labeled “a”, displays the connections between species of interest. The arrow widths indicate the rate-of-production from Equation (3) for a species at the base of the arrow with respect to the connecting species at the arrow head. The Rate of Production window (b) depicts the numerical values for each reaction related to a highlighted species. Additional descriptions of the remaining windows can be found in Appendix B.

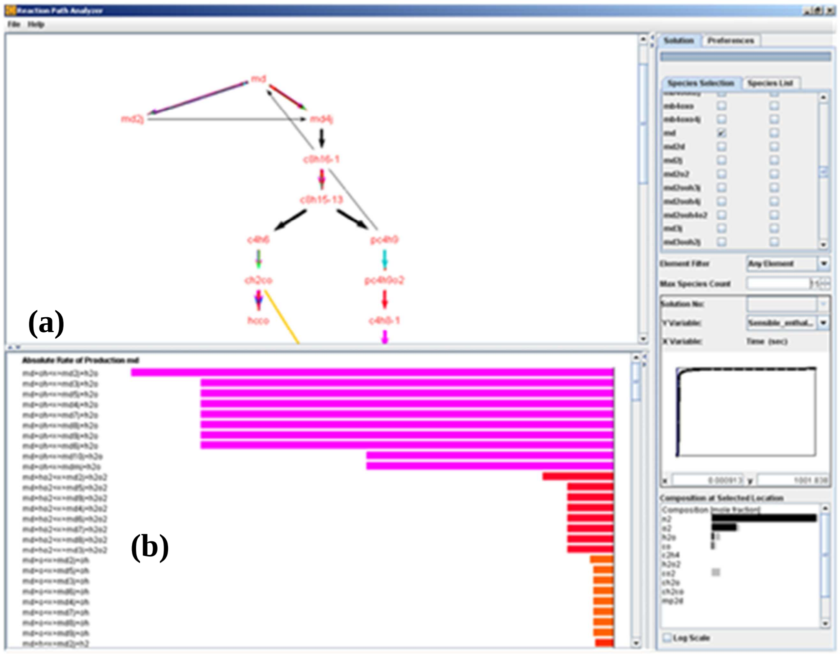

Figure 2-2: CHEMKIN-PRO Reaction Path Analyzer window, (a) Reaction Path Diagram and (b) Rate of Production display

2.1.4 KIVA3v-Release 2 Models

The biodiesel engine model was developed as part of the KIVA3v-Release 2 code used by the Engine Research Center (ERC). This multi-dimensional CFD code is coupled with the CHEMKIN II library, where KIVA accounts for flow and fuel preparation effects in the engine, and CHEMKIN describes the fuel chemistry. The CHEMKIN solver is called for each cell and the IVC temperature, pressure and species concentrations are supplied to the chemistry model. Within CHEMKIN, each cell of the computational grid is considered a well-stirred reactor.

Production rates for each species are calculated and used with the mass fraction, density, and molecular mass to form new species based on the reactions in the mechanism. Species concentration changes are returned to KIVA and these values are used to calculate the energy release [31,32]. The process of exchanging and updating species information between KIVA and CHEMKIN is repeated for each species in every cell at each time step in the calculation.

Turbulence was accounted for using the RNG κ-ε model. However, turbulence-chemistry interactions were not considered in this work. Previous researchers [33-35] have found that energy release is dominated by chemistry effects and not by sub grid-scale turbulent transport. A phenomenological nozzle flow model was used to account for flow losses and cavitation. Using a given nozzle configuration, the injection pressure, discharge coefficient, effective injection velocity and initial drop sizes are calculated for the injected fuel [36]. Once the fuel droplets are injected, an improved spray model that uses gas-jet theory was applied to reduce grid dependencies and improve both the relative velocity of the droplets and gas, and the entrainment rate [37].

The injected fuel droplets experience break-up according to the hybrid Kelvin-Helmholtz (KH)/Rayleigh-Taylor (RT) spray model [38]. The KH model predicts the primary break-up stage by evaluating the break-up time, τ_{KH}, using Equation (14), in which B_1 is an adjustable parameter, and Ω_{KH} and Λ_{KH} are the calculated frequency and wavelength of the fastest growing wave, respectively. In KIVA, B_1 is termed “cnst22” and given a value 40. As seen in the equation, a larger B_1 results in a longer break-up time.

$$\tau_{KH}=\frac{3.726B_1r}{\Omega_{\mathrm{KH}}\Lambda_{\mathrm{KH}}} \tag{14}$$

The radius of a child droplet in the KH model is calculated using Equation (15), where B_0 is also adjustable (B_0 is “balpha” in KIVA and assigned a default value of 0.6).

$$r_c = \mathrm{B}_0 \Lambda_{\mathrm{KH}} \tag{15}$$

A break-up length, L_b, is calculated using Equation (16),

$$L_b = C_{\mathrm{b}} d_0 \sqrt{\frac{\rho_f}{\rho_a}} \tag{16}$$

where ρ_f and ρ_a are the fluid and air densities, respectively, and d_0 is the parent droplet diameter. C_b (known as “distant” in KIVA) is an adjustable parameter with a default value of 1.9. Beyond this break-up length, the RT model is utilized to model secondary break-up of individual drops.

When the wavelength of the fastest growing wave on a given droplet is smaller than the droplet diameter, RT waves grow on the droplet surface. When the waves grow for a time greater than the break-up time, the droplet breaks up into child droplets. The radius of each child droplet is given in Equation (17), where C_{RT} is adjustable (“cnst3rt” in KIVA with a value of 0.10) and K_{RT} is the calculated wave number. In general, a smaller C_{RT} value will produce smaller child droplets.

$$r_c = \frac{\pi C_{RT}}{\mathrm{K}_{\mathrm{RT}}} \tag{17}$$

These droplets vaporize according to the physical properties found in the fuel library for the selected fuel. Ra and Reitz [39,40] expanded the KIVA3v-R2 package to include discrete multi-component (DMC) fuel considerations. The DMC code allows preferential evaporation based on nine temperature-dependent physical properties. The Design Institute for Physical Property Research (DIPPR), through the American Institute of Chemical Engineers, maintains an online database known as Project 801 [41]. This database includes correlations for a wide range of critically-evaluated thermophysical data. Table 2-1 shows the physical properties required by the DMC vaporization model and the correlation for each property. These correlations, along with correlation coefficients, molecular mass, critical temperature, and boiling temperature for each fuel species, are hardcoded into the KIVA3v-R2 model.

Table 2-1: Temperature-dependent physical property correlations used in the DMC model of KIVA3v-R2 [39,40]

Thermophysical Property	**DIPPR Correlation** [41]
Liquid density	$Y = \frac{A}{B^{\left[1+\left(1-\frac{T}{C}\right)^{D}\right]}}$
Vapor pressure	$Y = exp\left[A + \frac{B}{T} + C\ ln(T) + DT^{E}\right]$
Surface tension	$Y = A[1 - T_r]^{\left(B + CT_r + DT_r^2 + ET_r^3\right)}$
Liquid viscosity	$Y = exp\left[A + \frac{B}{T} + C\ ln(T) + DT^{E}\right]$
Liquid thermal conductivity	$Y = A + BT + CT^2 + DT^3 + ET^4$
Heat of vaporization	$Y = A[1 - T_r]^{\left(B + CT_r + DT_r^2 + ET_r^3\right)}$
Liquid heat capacity	$Y = A + BT + CT^2 + DT^3 + ET^4$
Vapor thermal conductivity	$Y = A + BT + CT^2 + DT^3 + ET^4$
Vapor viscosity	$Y = \frac{AT^{B}}{1 + \frac{C}{T} + \frac{D}{T^2}}$

** T_r is the reduced temperature, T/T_c*

The number of physical property surrogates used to represent a given fuel's composition is only limited by the available data and computational cost. The proportion of each property surrogate is estimated from an experimental composition, or selected to achieve appropriate vaporization (i.e., match a distillation curve) for a given fuel. Once the fuel is vaporized, the individual physical property surrogates can be coupled with representative chemistry species to account for component-specific chemistry.

The vaporized fuel chemistry is modeled using a kinetic reaction mechanism that contains species and thermodynamic data for a given fuel, as well as reactions and reaction rate information that describe the oxidation process. Realistic fuels are often complex mixtures of many species, and it is common to choose a surrogate species from a chemical family to represent the fuel mixture. For example, diesel fuel is largely composed of alkanes, and is often represented by n-heptane for chemistry. These fuel surrogates are chosen for their similar chemical properties and ignition behavior compared to the real fuel.

The reaction mechanism inherently contains reactions that produce pollutants such as CO, CO_2 and unburned hydrocarbons. However, unless the fuel of interest contains nitrogen, it is uncommon for NOx formation to be included. NOx formation in this model is accounted for by adding four species and 12 reactions to the mechanism. This 12-step NOx model was adapted from a mechanism developed by the Gas Research Institute (GRI) [42,43]. It includes thermal (extended Zeldovich) NOx reactions as well as reactions for NO_2 and N_2O.

2.2 Biodiesel Characteristics

An accurate engine model requires that both the combustion chemistry and the physical processes (spray break-up, atomization, vaporization, etc.) are well represented. These two aspects of the model depend on the fuel's composition. Biodiesel is made from the transesterification of fatty acids with an alcohol [44]. The exact composition (percentage of each methyl ester) depends on the feedstock used to produce it. Some common biodiesel vegetable oil feedstock includes rapeseed, peanut, canola, palm, coconut and soy [45]. More recently, the use of algae [46] has been proposed as a way to produce biodiesel in response to the controversial "food vs. fuel" and land-use issues associated with biofuel production [47].

In the United States, soy is a common feedstock, which is processed with methanol, resulting in a biodiesel fuel that is mainly composed of five methyl esters: methyl palmitate ($C_{17}H_{34}O_2$), methyl stearate ($C_{19}H_{38}O_2$), methyl oleate ($C_{19}H_{36}O_2$), methyl linoleate ($C_{19}H_{34}O_2$), methyl linolenate ($C_{19}H_{32}O_2$). As seen in Figure 2-3, methyl palmitate and methyl stearate are saturated, while methyl oleate, methyl linoleate, and methyl linolenate contain one, two, and three double-bonds, respectively. A common short-hand notation for these methyl esters is simply Cx:y, where 'x' represents the number of carbon atoms in the alkyl chain and 'y' represents the number of carbon-carbon double-bonds (e.g., C16:0 for methyl palmitate).

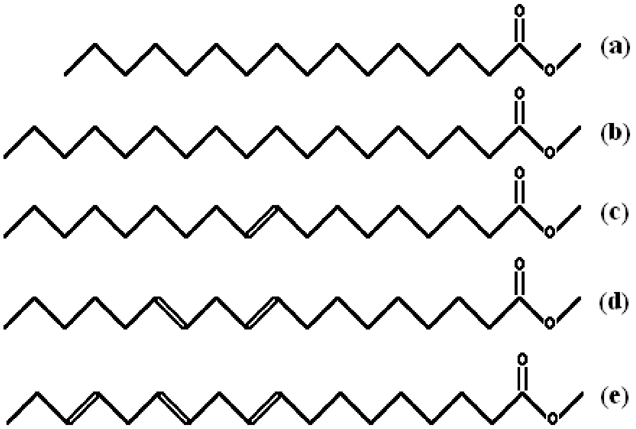

Figure 2-3: Five common components of soy-based biodiesel: (a) methyl palmitate, (b) methyl stearate, (c) methyl oleate, (d) methyl linoleate, and (e) methyl linolenate [48]

2.2.1 Biodiesel Physical Properties

Researchers at the University of Illinois – Urbana-Champaign [49] developed methods to accurately calculate biodiesel property values based on mixing rules and the known chemical composition of the fuel. Property predictions for biodiesel derived from soybean oil were found to be consistent with available experiments. The composition of the fuel was adjusted to see the effect on the properties. An increase in the amount of highly-unsaturated methyl esters (those with multiple double-bonds) caused high critical temperature and high heat of vaporization, but low vapor pressure and low liquid density. High fractions of nearly-saturated methyl esters resulted in high critical volume, surface tension and liquid viscosity.

Yuan et al. [50] later applied these biodiesel properties in engine simulations using KIVA3v. The code used the KH-RT model to describe break-up of the injected fuel. This model includes several constants that can be tuned for a given fuel, but the standard values were used for this work. The Shell model [51], which uses a generic eight-step mechanism to simulate the auto-ignition of hydrocarbons, was combined with a single-step combustion model to represent the fuel chemistry. These models were calibrated for both diesel and a soy biodiesel by adjusting reaction rate constants in the models. Pressure and heat release rate for the two fuels were consistent with experimental results. Biodiesel was found to ignite sooner, have higher in-cylinder temperatures, and longer fuel penetration compared to the diesel.

Stringer et al. [52] used the methods of Yuan et al. [49] to determine physical properties for biodiesel from a variety of feedstocks: soybean, coconut, palm and lard. The study used the KIVA3v-R2 code with the KH-RT break-up model (standard constants), and a multi-component model for the fuel vaporization [53]. The focus of the work was on understanding the break-up and vaporization characteristics of biodiesel and therefore, fuel chemistry was not considered. Five biodiesel blends were tested: B0 (pure diesel), B2, B5, B20, and B100, where the number represents the percent (by volume) of soy biodiesel in the mixture. The pure soy biodiesel was then compared to pure coconut, pure palm and pure lard biodiesels. Fuel sprays were analyzed in a three-dimensional, constant volume cylinder under conditions typical of an engine at the time of injection. The results for the biodiesel blends showed that an increased percentage of soy biodiesel caused decreased volatility (reduced vapor mass) and increased spray tip penetration. When the pure biodiesels were compared, it was shown that the soy biodiesel was the slowest to vaporize and had the largest droplet diameters. Coconut biodiesel, which had the lowest boiling point, vaporized the fastest.

Chakravarthy et al. [54] used correlations and mixing rules similar to Yuan et al. [49] to calculate average physical and thermodynamic properties for soy biodiesel. In some instances the properties of methyl oleate, one of the five main constituents of biodiesel, were used. Property information for methyl oleate is readily available in databases such as DIPPR [41].

These average properties were added to the KIVA3v-R2 fuel library and applied in engine simulations. Two operating regimes were considered: conventional diesel combustion with injection near top dead center (TDC), and premixed charge compression-ignition (PCCI) combustion with early injection and reduced O_2 to simulate exhaust gas recirculation (EGR). In both cases, the KIVA3v-R2 code was coupled with CHEMKIN II [28,31] for a more detailed representation of the fuel chemistry than that offered by the Shell ignition model. A reduced n-heptane mechanism [32] was used to represent fuel. For the conventional combustion case, it was found that the physical property differences caused delayed ignition for biodiesel compared to diesel. However, in the PCCI case, where the chemistry is more important, the two fuels produced similar results due to their identical fuel mechanism.

Ra et al. [55] expanded on the work of Chakravarthy et al. by identifying the fuel properties responsible for the differences in combustion. The study first considered non-reacting, single-droplet evaporation and it was found that the fuel liquid density and vapor pressure had the greatest effect on evaporation. Combustion simulations in both a heavy- and light-duty diesel engine were performed and in general, the biodiesel properties delayed vaporization and ignition, increased liquid penetration, and lowered peak in-cylinder gas pressure compared to diesel fuel properties. However, no single biodiesel property could be linked to the differences. Instead, a coupled effect of liquid fuel density, vapor pressure and surface tension appeared to be responsible.

These studies were able to apply accurate physical properties and gain insight into the effect of certain properties. However, they either did not consider chemistry, relied on overly-simplified reaction kinetics (the Shell model), or used detailed chemistry, but applied a hydrocarbon (n-heptane) instead of a methyl ester. While these studies are valuable, they do not consider the unique chemical structure of biodiesel and as a result, may be neglecting important intermediate species that could be responsible for some of biodiesel's characteristic differences in emissions.

2.2.2 Biodiesel Mechanisms

In order to adequately represent the combustion chemistry of biodiesel fuel, an accurate chemical kinetic mechanism must be available. Previous work has explored the use of methyl butanoate ($C_5H_{10}O_2$) as a biodiesel fuel surrogate [56], but studies have shown that this species does not adequately capture the ignition delay or the species history (e.g., CO_2) seen in biodiesel [57-60]. These results have been attributed to the insufficient length of the carbon chain in methyl butanoate (MB). In response to this issue, a combination of 1/3 MB and 2/3 n-heptane was proposed by Brakora et al. [61]. A mechanism was developed for this two-fuel biodiesel surrogate by reducing the number of species of the comprehensive MB mechanism and combining it with a well-tested mechanism for n-heptane oxidation [32]. NOx chemistry was represented by the adapted GRI mechanism [23,42].

The biodiesel mechanism, ERC-bio, and the physical property data from Ra et al. [55] were applied in an engine simulation using KIVA3v-R2 coupled with CHEMKIN II [62]. The biodiesel model was validated against experiments performed at Sandia National Laboratories [63] and was found to match ignition time, pressure, and heat release rate, which suggests that the fuel oxidation chemistry was well-represented. However, NOx was significantly under-predicted.

More recently, researchers at the Lawrence Livermore National Laboratory (LLNL) have proposed methyl decanoate ($C_{11}H_{22}O_2$) as a biodiesel fuel surrogate, arguing that its longer carbon chain would provide a better prediction of the ignition and species history [60]. The mechanism was tested against a limited number of ignition and jet-stirred reactor (JSR) experiments, and it was found to be more representative of biodiesel fuel chemistry.

Hoffman and Abraham [64] used single-zone HCCI simulations and detailed reaction mechanisms to compare n-heptane (a common surrogate for diesel fuel chemistry), methyl decanoate (a proposed biodiesel surrogate) and dimethyl ether (a biofuel). Their work investigated the impact of EGR on NO formation. As expected, the addition of EGR increased ignition delay and decreased NO formation for the three fuels, which was attributed to the decreased O_2 concentration and decreased temperatures. However, the authors were unable to make a definitive comparison of NO formation between fuels, since the n-heptane required higher initial temperatures to match ignition times. The higher initial temperatures resulted in higher peak temperatures and higher NO for the diesel surrogate, which is contrary to observations in many engine experiments.

In another study, Song et al. [65] experimentally compared the effect of intake air oxygen enrichment and fuel oxygenation on soot and NOx emissions in a diesel engine. Both cases resulted in decreased soot and only the intake oxygen enrichment caused significant NOx increases. The authors suggest that the NOx increase with oxygen enrichment was due to the more readily available atomic oxygen or the higher temperatures that enhance thermal NOx.

Brakora and Reitz [66] also performed HCCI simulations in order to investigate the effect of chemistry on the prediction of NOx. The previous biodiesel surrogate (MB + n-heptane) was compared to the traditional diesel surrogate (n-heptane) over a range of equivalence ratios in single-zone HCCI simulations. It was found that only a small (< 3%) increase in NOx was observed with the use of biodiesel for equivalence ratios below stoichiometric. Additionally, it was found that the fuel-bound oxygen in biodiesel did not increase NOx to the extent that the same amount of oxygen created if it were available in the surrounding air.

Studies have shown that the appearance and location of double-bonds can have a significant effect on the fuel chemistry [59,67]. Since biodiesel is typically composed of several unsaturated methyl esters, the methyl decanoate mechanism was expanded to include methyl-9-decenoate ($C_{11}H_{20}O_2$), which has a double-bond at the ninth position on the carbon chain [59]. Figure 2-4 compares the chemical structure of biodiesel fuel surrogates that have available detailed chemistry mechanisms. The figure also depicts the numbering scheme applied to the carbons, as implemented in the LLNL mechanisms. Note that the species contain the similar methyl ester structure seen in Figure 2-3, and the methyl-9-decenoate double-bond is in the same location as that of the first double-bond in the methyl oleate, methyl linoleate, and methyl linolenate components of real biodiesel fuels.

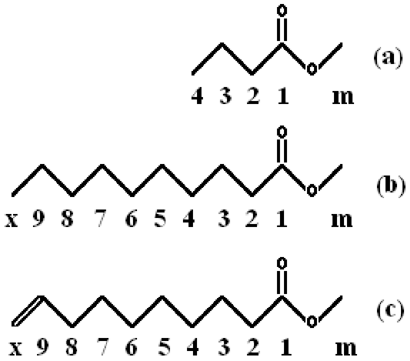

Figure 2-4: Chemical structure of three biodiesel surrogate species with available mechanisms: (a) methyl butanoate, (b) methyl decanoate, and (c) methyl-9-decenoate

As a result of their long carbon chains, the combined methyl decanoate (MD) and methyl-9-decenoate (MD9D) reaction mechanism from LLNL contains 3299 species and 10806 reactions, which also includes n-heptane for use as an alkane surrogate for biodiesel blending. While this mechanism was found to adequately represent biodiesel chemistry, its size restricts its ability to be directly applied in engine CFD models due to computational limitations. Instead, mechanisms of this size are limited to completely mixed, zero-dimensional models that can be used to predict ignition times and species concentrations, but are not representative of the transient behavior observed in actual engines. It is necessary to use a reduced mechanism for application in CFD models.

2.2.3 Mechanism Reduction Techniques

The general procedure for mechanism reduction involves identifying species and reactions that do not significantly contribute to the specific desired results (e.g., ignition delay time) of a given operating condition and removing them from the mechanism. For detailed mechanisms on the order of 100 species, it is possible to use a simple reaction flux analysis to identify which species are insignificant [32,61]. Seiser et al. [68] created a reduced n-heptane mechanism using a sensitivity analysis based on ignition delay. Constant pressure, homogeneous reactor simulations were performed using the comprehensive mechanism under several conditions. Species and all reactions in which the species appeared were systematically removed and the ignition delay time was measured. If the ignition delay did not deviate from that of the comprehensive mechanism by more than 0.84%, that species and its corresponding reactions were removed from the mechanism. This process resulted in an intermediate mechanism of 282 species and 1282 reactions. The mechanism was reduced further by assessing the chemical pathways related to the fuel breakdown and oxidation. Species were neglected if they only appeared in pathways where the rate of fuel breakdown and oxidation were small. The final reduced mechanism had 160 species and 770 reactions.

Golovitchev [69] created a skeletal n-heptane mechanism containing 40 species and 165 reactions. This method utilized sensitivity analysis and atom conservation. Ignition times of the resulting mechanism were validated against experimental shock tube data and some reaction rates were adjusted to improve the predicted ignition delay times. The mechanism captured the negative temperature coefficient behavior of n-heptane and accurately reproduced its ignition delay timing for 13.5 bar and 41 bar pressure conditions.

The Golovitchev skeletal mechanism was further reduced by Patel et al. [32]. In a similar method to that of Seiser, a sensitivity analysis was performed on species over a range of initial conditions. Species and reactions were removed based on ignition delay time comparisons. This method included application of a micro-genetic algorithm to optimize reaction rate constants in order to improve the agreement with more comprehensive mechanisms. The final reduced mechanism included 29 species and 52 reactions and was successfully applied to diesel engine simulations over a wide range of operating conditions.

When mechanism sizes exceed 1000 species, it can be time consuming to manually evaluate every possible pathway. Several automated reduction techniques are available, which have been shown to drastically reduce the size of mechanisms, while maintaining much of the fidelity of their detailed counterparts.

Lu and Law [70-72] applied the theory of directed relation graph (DRG) to the process of mechanism reduction. This method identifies unimportant species by considering how they are coupled to other species in the mechanism. A normalized contribution parameter, r_{AB}, is calculated to quantify the contribution of species B to the production rate of species A. In Equation (18), I is the total number of reactions, $\nu_{A,i}$ is the overall stoichiometric coefficient for species A, ω_i is the production rate, and $\delta_{B,i}$ is a delta function that is unity if reaction i contains species B, and zero otherwise.

$$r_{AB} \equiv \frac{\sum_{i=1,I} \left| \upsilon_{A,i} \omega_i \delta_{B,i} \right|}{\sum_{i=1,I} \left| \upsilon_{A,i} \omega_i \right|} \tag{18}$$

The nodes in the directed relation graph are linked to individual species in the mechanism and an edge is formed between two species if r_{AB} is larger than some user-specified tolerance ε. Key species of interest (i.e., fuel and desired products) are identified and r_{AB} is calculated with respect to those species. The DRG can then be used to identify which species are strongly coupled to those key species and eliminate the rest. Using a threshold value of $\varepsilon = 0.16$, the authors demonstrated that a detailed ethylene reaction mechanism of 70 species could be reduced to 33 species without a significant effect on performance. The reduced and detailed mechanisms were well matched in terms of auto-ignition and temperature profiles from perfectly stirred reactor simulations.

Perpiot-Desjardins and Pitsch [73] made several improvements to the DRG method. They noted that the original version considered production and consumption reactions of equal weight, but that a species that only consumes A would not have the same effect as one that produces and consumes it. This error-propagating (DRGEP) method considers the net contribution of species B to species A, giving a more appropriate indication of the strength of the relationship between the two species. Using this idea, Equation (18) was reformulated into Equation (19).

$$r_{AB,PDP} = \frac{\sum_{i=1,I}\left|\nu_{A,i}\omega_i\delta_{B,i}\right|}{\max(P_A, C_A)} \tag{19}$$

where P_A and C_A are the max production and consumption of each species defined as follows:

$$\mathrm{P_A} = \sum_{\mathrm{i}=1}^{\mathrm{I}} \max\left(0, \nu_{\mathrm{A,i}}\omega_{\mathrm{i}}\right) \tag{20}$$

$$\mathrm{C_A} = \sum_{\mathrm{i}=1}^{\mathrm{I}} \max\left(0, -\nu_{\mathrm{A,i}}\omega_{\mathrm{i}}\right) \tag{21}$$

Other modifications have been made to the DRG reduction method and several studies have applied the method to reduce the methyl decanoate mechanism. Shi et al. [29,74] developed an automatic reduction code based on the DRGEP method that used a Senkin-based model for single-zone HCCI engine simulations. The mechanism reduction procedure compared three performance parameters (CA50, peak pressure and peak heat release) of the reduced mechanism to those of the detailed mechanism. Additional details of this model are included in following section. Using this code, the original MD mechanism (no MD9D) was reduced from 3036 species and 8555 reactions to 435 species and 1098 reactions with validation against the detailed mechanism in single-zone HCCI simulations.

Seshadri et al. [75] used DRG to reduce the MD mechanism to 125 species and 713 reactions with validation against the detailed mechanism in perfectly stirred reactor (PSR) simulations and against extinction experiments in a counterflow reactor. Luo et al. [76] focused on the high-temperature chemistry and used a combination of DRG and chemical lumping to reduce the MD+MD9D+n-heptane mechanism to 118 species and 837 reactions. The results were well-matched to the detailed mechanism in PSR simulations and to jet-stirred reactor experiments with rape seed oil methyl ester. Luo et al. [77] later used a similar reduction technique to develop a 123 species (394 reactions) mechanism that included low-temperature chemistry. The mechanism was validated against experimental flame lift-off data from Sandia National Laboratories. The mechanisms developed by Luo et al. [76,77] were reduced using mixtures of 25% MD, 25% MD9D and 50% n-heptane. The results are given for this mixture only, and the authors do not indicate the accuracy of results using the individual fuels compared to the detailed mechanism.

DRG has shown promise as a means of significantly reducing biodiesel surrogate mechanisms. However, current computational resources still require mechanisms to be less than 100 species to ensure efficient computational times for use with multi-dimensional engine models. To address the limitations of DRG, a combination of DRG and manual isomer lumping was applied to achieve the desired mechanism size for this work.

Chapter 3: Chemistry Model Formulation and Validation

It was of interest to thoroughly document the reduction and optimization process for future mechanism reduction efforts. This chapter describes the reduction process applied to the LLNL MD/MD9D mechanism. In addition to the description here, a Mechanism Reduction Manual was created to outline general reduction steps for any mechanism of interest. The manual includes detailed instructions for using the automated DRG code and strategies for performing sensitivity analysis on and adjusting reaction rate constants. A copy of the manual is included in Appendix B and a directory is available that contains input files, example cases and source codes, as well as the semi-automated scripts and post-processing files to analyze new mechanisms.

3.1 Mechanism Reduction

The single-zone, Senkin-based DRGEP model developed by Shi et al. [74] was used in this work for the initial mechanism reduction. For the current work, the code was modified to include a constant volume reactor model to test the mechanism's performance over a wider range of conditions. The code calculates the DRG contribution index using $r_{AB,PDP}$ in Equation (19) for each species in the mechanism and compares the value to a given contribution tolerance, ε. Species with indices below ε are deemed to have an insignificant effect on the key species and can be reliably removed from the mechanism. A reduced mechanism is generated and a second simulation is run to compare the performance parameters (ignition delay, peak pressure, and peak key species concentration) predicted by the reduced mechanism to those of the detailed mechanism at given conditions. If the reduced mechanism results do not exceed a specified error tolerance, DRG is repeated with an increased (less stringent) ε value. The process continues until either the error tolerance is exceeded or the mechanism size no longer changes. A diagram of the process can be seen in Figure 3-1.

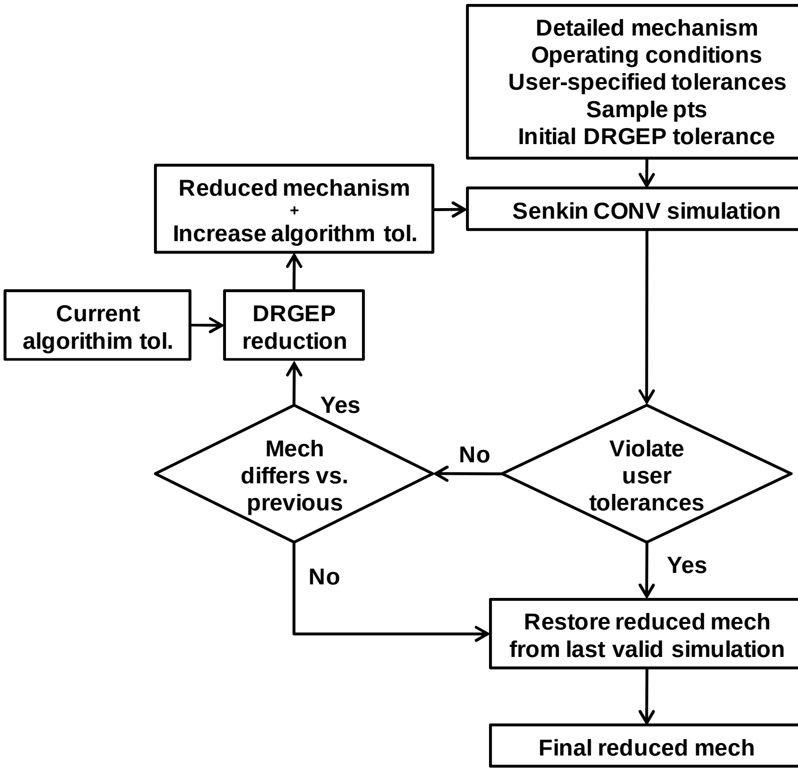

Figure 3-1: Flow chart describing the automated DRGEP reduction process [74]

Mechanism reduction was performed in four main steps. In the first step, DRGEP was applied to the detailed mechanism using the MD fuel and MD9D fuels separately, which was done to ensure that each fuel is properly modeled. A lean equivalence ratio (ϕ=0.5) and low temperature (T=800K) condition was chosen for the DRG reduction, because these conditions require the greatest number of reactions. The initial DRGEP contribution tolerance was set to 0.0001 as recommended by Ref. [74]. The key species to track were the fuel, CO and HO_2 to ensure that the fuel decomposition, CO oxidation and H_2-O_2 chemistry were well represented. The error tolerance for comparison to the detailed mechanism's ignition delay time was set to 50% for this step in order to obtain a very small mechanism. This step resulted in two separate intermediate mechanisms, with 271 species (753 reactions) for MD fuel and 173 species (554 reactions) for MD9D fuel. Figure 3-2 shows reduction history and associated errors for the two fuels. After more than 20 iterations, the ignition error exceeded the tolerance for each fuel.

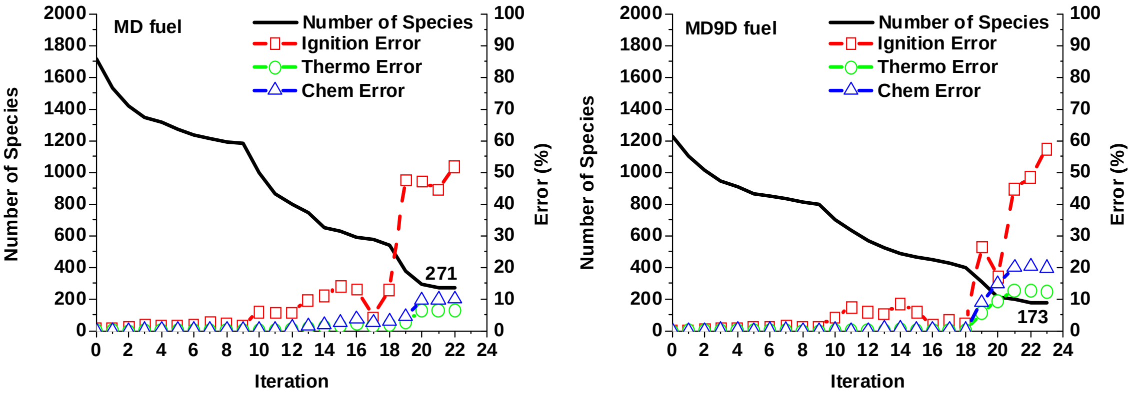

(a) (b)

Figure 3-2: Reduction history for step 1: (a) methyl decanoate and (b) methyl-9-methyl decenoate

The intermediate mechanisms were compared to the detailed mechanism over a range of temperatures and equivalence ratios for the 60 bar pressure condition to ensure that there were no major changes in ignition delay during the reduction process. Figure 3-3 shows the ignition delay time results under lean (ϕ=0.5), stoichiometric, and rich (ϕ=2.0) conditions for each fuel. The right axis shows the crank angle for each time assuming an engine speed of 1000 rev/min.

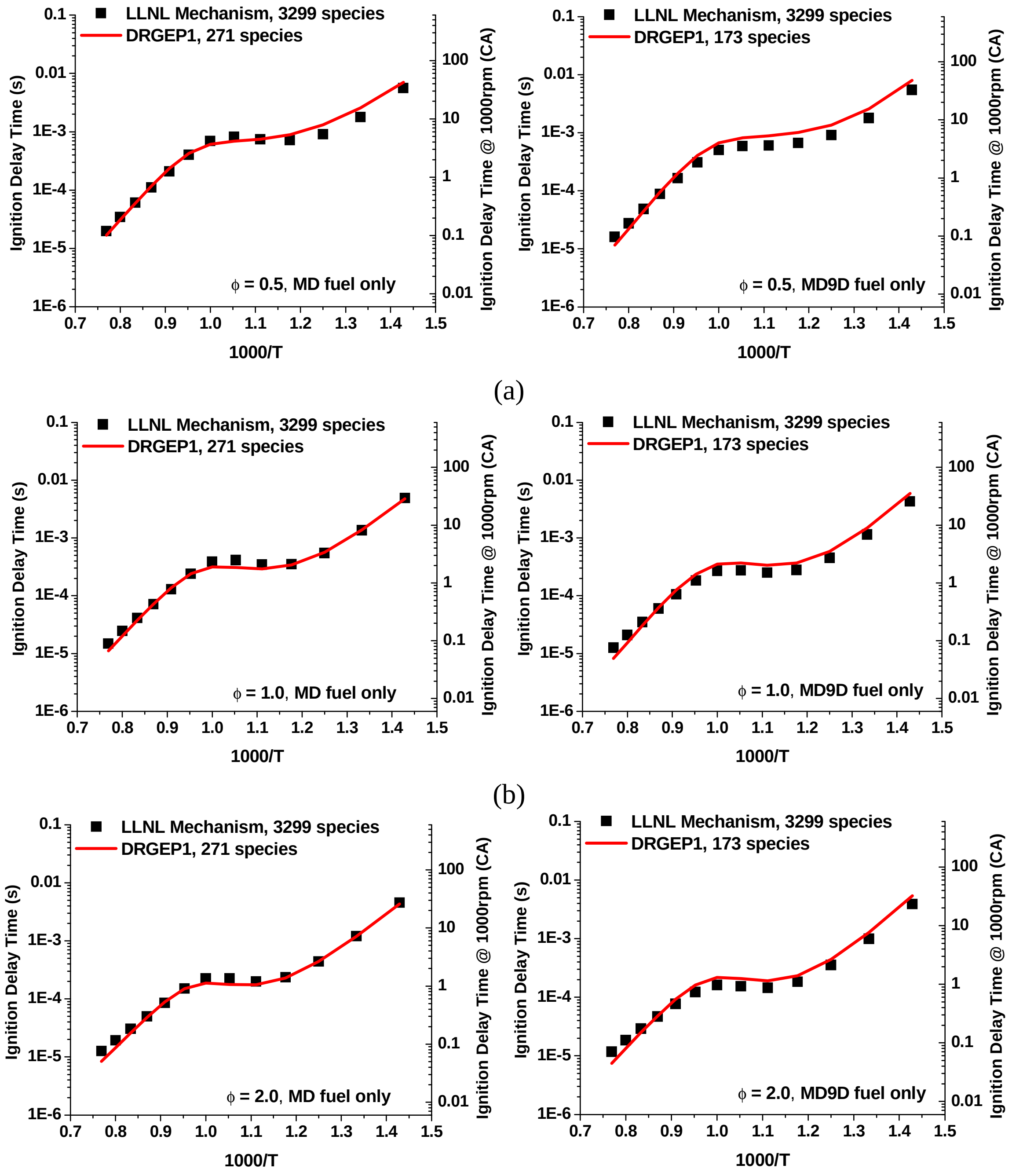

(a)

(b)

(c)

Figure 3-3: Ignition delay times (detailed mechanism [59] in symbols, reduced mechanism as a line) for each fuel under P=60 bar and (a) lean, (b) stoichiometric, and (c) rich equivalence ratio conditions.

The intermediate mechanisms were both limited by the error tolerance for ignition time. The largest relative error occurred in the lean equivalence ratio condition for both fuels. The largest error for the intermediate MD mechanism was 45% (corresponding to 2.5 CA) at 800K, and was 50% (2.0 CA) at 850K for the intermediate MD9D mechanism. These errors were within the allowable range for this major reduction step and the general trend of the ignition delay time curves remained intact.

In the second step, the Reaction Pathway Analysis tool in the CHEMKIN-PRO computer package [78] was used to identify isomer species from the H-abstraction reactions in each mechanism. These isomers tend to have common thermodynamic data and often share the same reaction rate constants in reaction mechanisms. Figure 3-4 shows the H-abstraction isomers produced when MD is the fuel. The “j” represents a radical site on the carbon numbered according to the convention shown in Figure 2-4. To avoid making rate constant adjustments at this early stage, only isomers that did not have a large impact on ignition were removed. Three H-abstraction isomers were retained in each mechanism: md3j, md6j and md8j for MD, and md9d2j, md9d6j and md9d8j for MD9D.

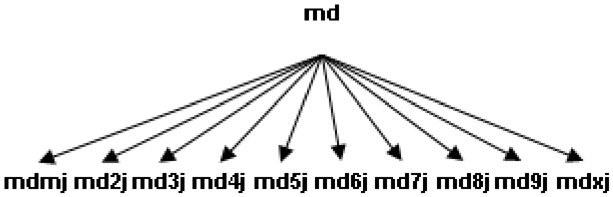

Figure 3-4: Example H-abstraction isomers formed from oxidation of the MD fuel species

Once the isomers were removed, the DRG procedure was repeated to remove species that lost pathways connecting them to the key species. The second DRG reduction resulted in mechanisms containing 132 species for MD and 129 species for MD9D. Figure 3-5 shows the lean equivalence ratio ignition delay results for the first DRG reduction (solid), manual isomer removal (dash), and second DRG reduction (dash-dot).

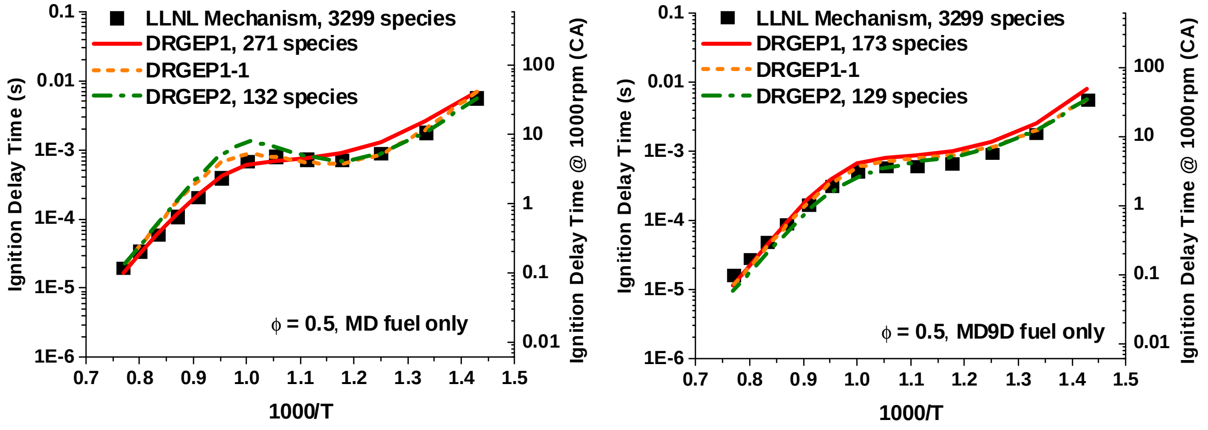

(a) (b)

Figure 3-5: Ignition delay time after the second DRG reduction step. Detailed mechanism (symbols), first DRG reduction (solid), manual H-abstraction isomer removal (dash), second DRG reduction (dash-dot)

Additional insignificant species were identified using the CHEMKIN-Pro reaction pathway tool and manually removed from the mechanism. The individually-reduced MD and MD9D mechanisms contained 83 and 71 species, respectively. The mechanisms were combined into a single mechanism that contained 111 species and 331 reactions. It was found that eight reactions could be assimilated into four to remove four species without altering the ignition time. Table A-1 in the Appendix shows the reactions that were combined. Additional species that did not directly contribute to the flow from fuel through the main pathways were also removed. This resulted in errors beyond 50% but the errors were accepted as long as the general shape of the ignition delay curve remained intact. It was expected that rate constants would be adjusted to improve the ignition predictions.

The combined MD+MD9D mechanism contained 85 species and 280 reactions; a reduction of over 98% compared to the comprehensive mechanism. Figure 3-6 shows the key pathways identified in the mechanism reduction process. The final species in each branch leads to C_4 and smaller species. A description of the naming convention can be found in Appendix A.

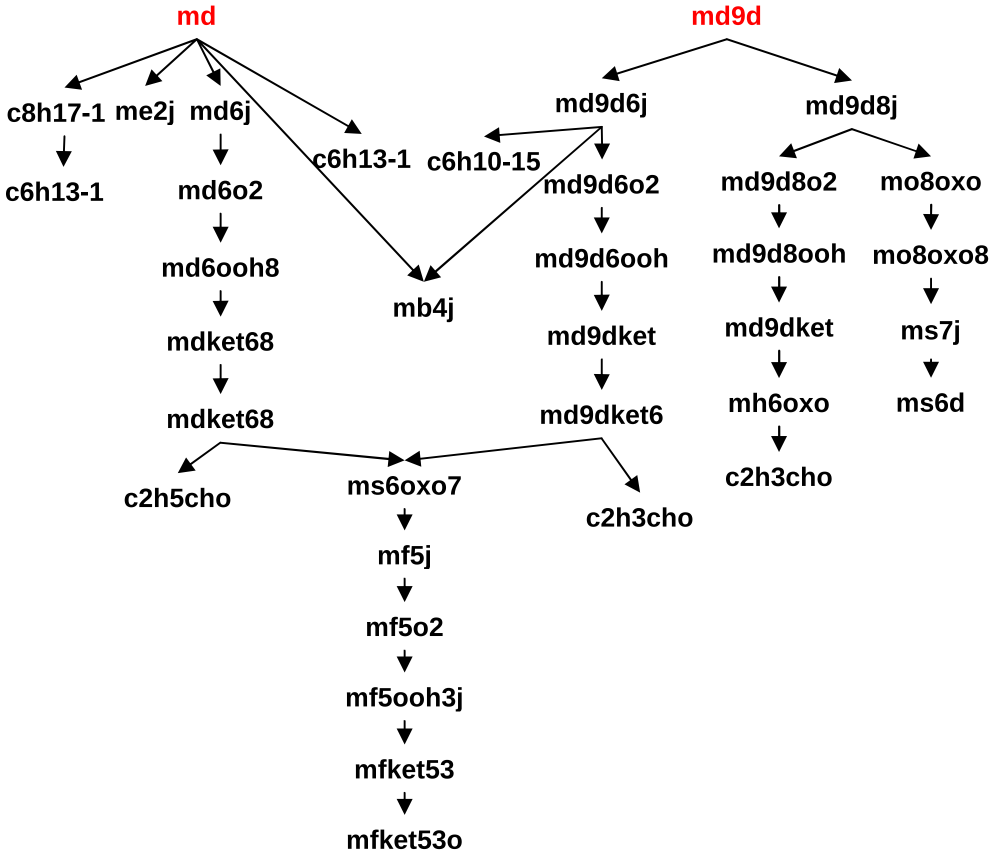

Figure 3-6: Key pathways in the MD-MD9D mechanism as identified in the reduction process.

Finally, the MD-MD9D reduced mechanism was combined with a multi-chemistry mechanism (ERC-MultiChem) that contains oxidation reactions for a variety of fuel species [40]. This mechanism was chosen as a base anticipating that future biodiesel applications may include fuels such as ethanol or multi-component diesel or gasoline. In this work, however, only single-component diesel was necessary. All fuel oxidation reactions except n-heptane were removed from the mechanism in order to save computation time. Only the fuel oxidation steps for the MD and MD9D fuels (essentially the reactions corresponding to the pathways in Figure 3-6) were transferred to the new mechanism. In doing so, the n-heptane, MD and MD9D fuels share common lower-level reaction pathways that contain C_4 species and smaller. The resulting model, henceforth referred to as ERC-MultiChem+MD/MD9D, contained 77 species and 216 reactions, including those for NOx formation and n-heptane oxidation.

3.2 Reaction Rate Constant Adjustments

When a large fraction of the total species is removed from a mechanism, the production rate of key species can be affected. This can be accounted for by adjusting reaction rate constants for the remaining reactions. First, however, it is necessary to identify appropriate reactions to adjust. Curran et al. [30] developed the first LLNL n-heptane reaction mechanism, and outlined 25 major classes of elementary reactions that are important for n-heptane oxidation. These reaction classes are now the basis of most mechanisms developed at LLNL, including the MD/MD9D and ERC-MultiChem mechanisms. Each class has a different effect on the ignition delay time predictions of mechanisms. Reactions in the first nine classes are dominant at high temperatures (above about 900K). The remaining classes are considered low-temperature reactions. Table 3-1 identifies the reaction classes that remained after reducing the MD/MD9D mechanism.

Table 3-1: Reaction classes from Curran et al. [30] remaining in reduced MD/MD9D mechanism

Class	Description	Example
1	Unimolecular fuel decomposition	md6j+h=md
2	H-atom abstraction from the fuel	md+oh=md6j+h2o
3	Alkyl* radical decomposition	c6h13-1+mb4j=md6j (rev)
4	Alkyl* radical + O_2 to produce olefin** + HO_2 directly	c6h13-1+o2=c6h12-1+ho2
10	Addition of alkyl* radicals to O_2	md6j+o2=md6o2
12	Alkyl peroxy radical isomerization: RO_2 <=> QOOH	md6o2=md6ooh8j
22	Addition of QOOH to O_2	md6ooh8j+o2=md6ooh8o2
23	Isomerization of O_2QOOH to ketohydroperoxide + OH	md6ooh8o2=mdket68+oh
24	Ketohydroperoxide decomposition to oxygenated radical + OH	mdket68=mdket68o+oh

** also includes alkyl ester; ** also includes unsaturated esters*

As shown previously in Equation (4), the rate constants are Arrhenius expressions. Two of the three rate parameters provided in the mechanism file (i.e., A and E) were chosen as candidates to adjust the rate constants. The pre-exponential factor, A, is directly related to the rate constant, and increasing A will increase the constant equally over the entire temperature range. Figure 3-7(a) shows the effect of increasing and decreasing A by an order of magnitude; the entire curve is shifted up or down. Figure 3-7(b) shows the effect of increasing and decreasing the activation energy by 20%. The activation energy, E, is a temperature-dependent energy barrier. Changes to E indirectly affect the rate constant and change the slope of the curve.

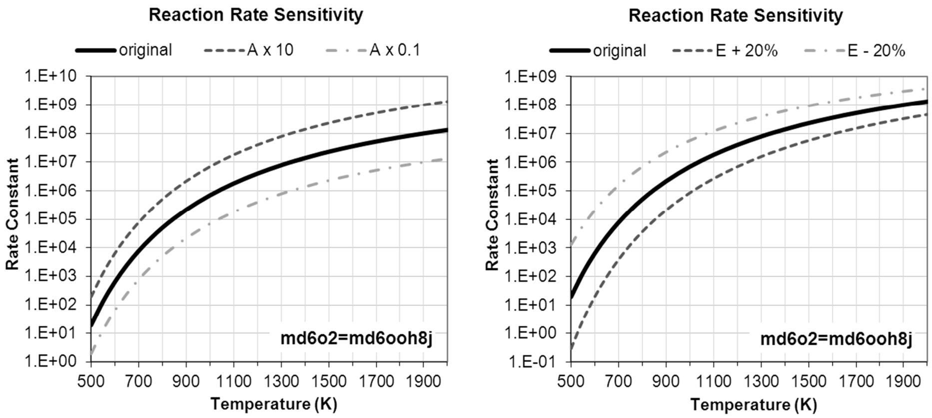

(a) (b)

Figure 3-7: The effect of changes to the (a) pre-exponential "A", and (b) activation energy, "E" rate parameters for an example reaction

In this work, a systematic approach was used to adjust the rate parameters. A sensitivity study was performed on the key classes to assess the effect of rate adjustments on ignition delay time. To evaluate the sensitivity of a given reaction, six rate adjustments were made according to Table 3-2.

Table 3-2: Description of the six adjustments in the reaction rate parameter sensitivity analysis

Test	**Reaction Rate Parameter Adjustment**	
	Pre-exponential factor (A)	**Activation Energy (E)**
(a)	Increase by a factor of 2.0	No change
(b)	Decrease by a factor of 2.0	No change
(c)	Increase to match at 2000K	Increase x 20%
(d)	Increase to match at 500K	Increase x 20%
(e)	Decrease to match at 2000K	Decrease x 20%
(f)	Decrease to match at 500K	Decrease x 20%

Figure 3-8 displays how the rate constant of the important MD isomerization reaction changed in the sensitivity analysis. This reaction has a large (negative) activation energy and the small changes have a noticeable effect on the reaction rate constant. The pre-exponential factor was doubled and halved and Figure 3-8(a) shows that the entire rate constant shifts up and down equally. The activation energy was increased and decreased by 20% in Figure 3-8(b) and (c), respectively. For activation energy adjustments, the two extreme values of A (matching the original rate constant at the 500K and 2000K temperature points) provided suggested limits for the pre-exponential value. These limits allowed some change to the temperature dependence, but kept the rate constant within about an order of magnitude of its original value. In general, there is less confidence in the pre-exponential factor value, and therefore a larger range of adjustment was allowed.

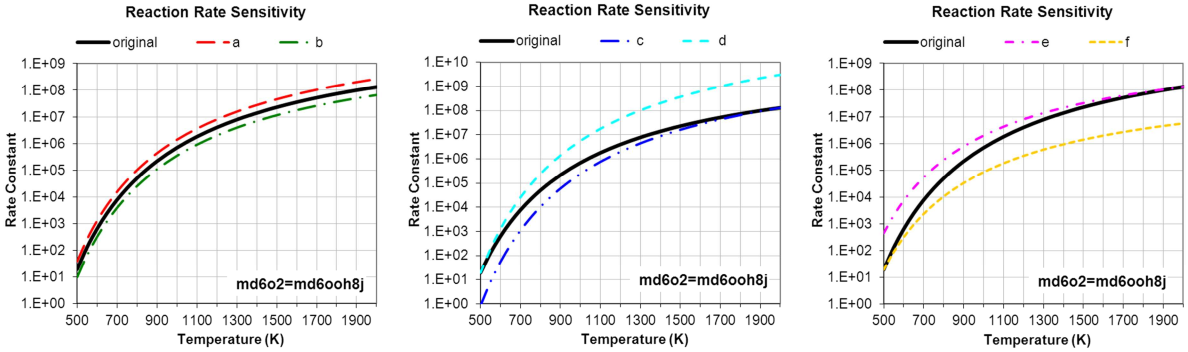

(a) (b) (c)

Figure 3-8: Effect of reaction rate parameter adjustments from Table 3-1 on the rate constant for the MD isomerization reaction

The remaining MD/MD9D reactions that were members of the classes found in Table 3-1 were tested to assess the effect that each reaction had on ignition delay time. These sensitivity tests were performed at 60 bar and stoichiometric ($\phi = 1.0$) conditions. The five reactions with the largest effects are shown in for MD fuel Figure 3-9 and MD9D fuel in Figure 3-10. The corresponding reaction rate constant changes for each of these sensitivity adjustments are provided in Appendix A.

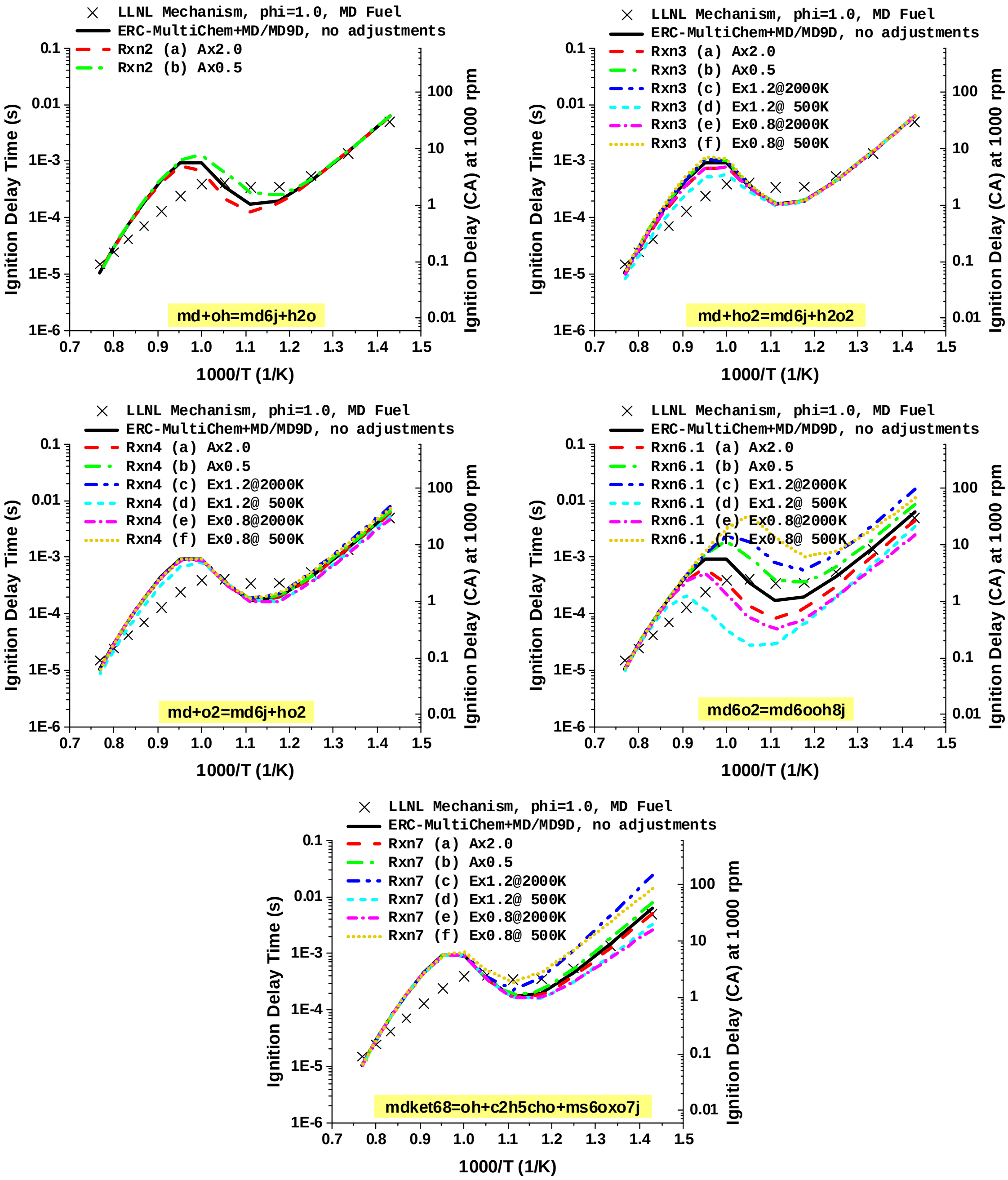

Figure 3-9: Ignition delay time sensitivity analysis for MD reactions

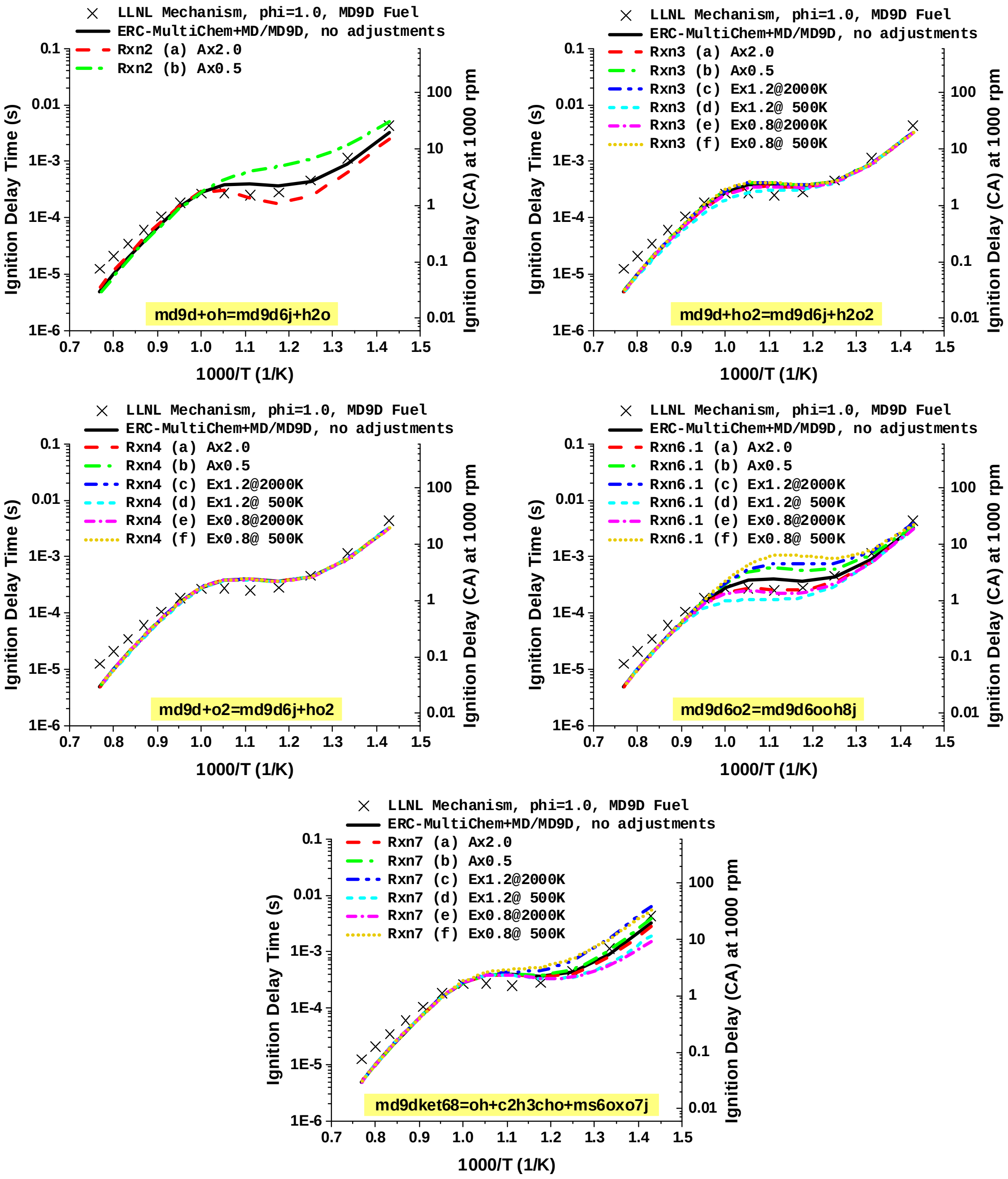

Figure 3-10: Ignition delay time sensitivity analysis for MD9D reactions

The MD portion of the mechanism required adjustment of three reactions to improve the ignition delay time. As shown in Figure 3-11(a), the *md+ho2* reaction was first adjusted to advance ignition at high temperatures. Then the *md+oh* reaction was used to delay ignition at the intermediate temperatures. Finally, the *md+o2* reaction slightly advanced ignition at the lowest temperatures. Two reactions were adjusted to improve the MD9D ignition. It is not clear from the sensitivity analysis how one might improve the high temperature, but closer inspection of the *md+oh* figure suggests that the ignition curve actually "pivots" around the 1000K point (1.0 on the plot). Adjustments to advance ignition at low temperatures will also slightly delay high temperature ignition and *vice versa*. Instead of showing the sequence of rate adjustments in Figure 3-11(b), the individual adjustments are shown to distinguish their effects. Table A-2 in the Appendix displays the original and new rate constants for the five adjusted reactions in the reduced mechanism.

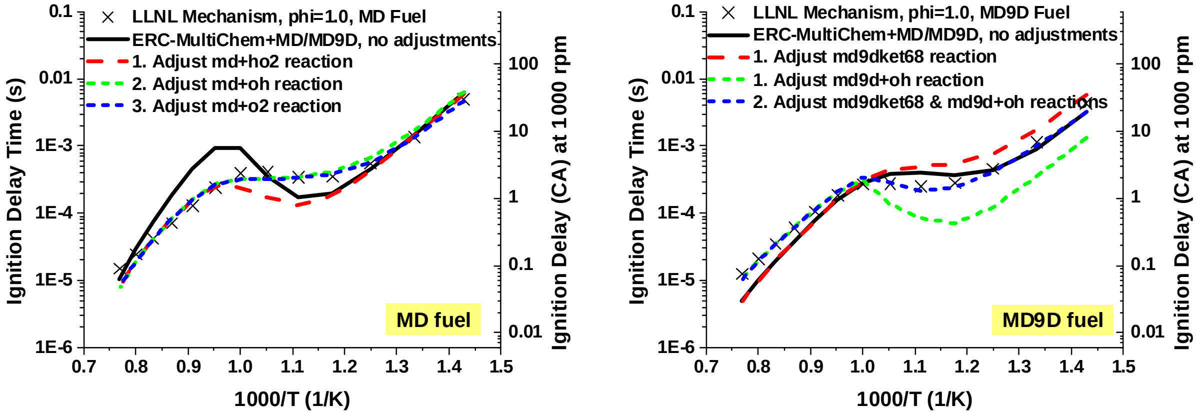

(a) (b)

Figure 3-11: Effect of final reaction rate constant adjustments on ignition delay time at P=60 bar, stoichiometric conditions

3.3 Ignition Delay Time Validation

Once the mechanism was adjusted, it was necessary to repeat the full validation process. The ultimate goal of this mechanism was to apply it in engine simulations. Table 3-3 outlines the representative engine conditions used to validate the mechanism's ignition delay predictions.

Table 3-3: Constant volume conditions used to test reduced mechanism performance

Parameter	**Range Considered**
Equivalence ratio, ϕ	0.5, 1.0, 2.0
Initial Temperature (K)	700-1300 (50K increments)
Initial Pressure (bar)	40, 60, 80

Figure 3-12 shows the ignition delay predictions for the range of conditions in Table 3-3. Limited biodiesel ignition delay data is available and at present, the validation against the detailed mechanism was deemed sufficient until relevant ignition data becomes available. Each figure depicts three initial pressure conditions for a given equivalence ratio and fuel. Excellent agreement is seen in Figure 3-12(b) under stoichiometric conditions for both fuels. The MD fuel also predicts well for the lean and rich conditions, while the MD9D fuel is advanced for the lean case in Figure 3-12(a) and delayed for the rich case Figure 3-12(c). Rate adjustments to correct for the advanced lean condition caused an exaggerated delay for the rich case and *vice versa*, so the original values were considered a compromise.

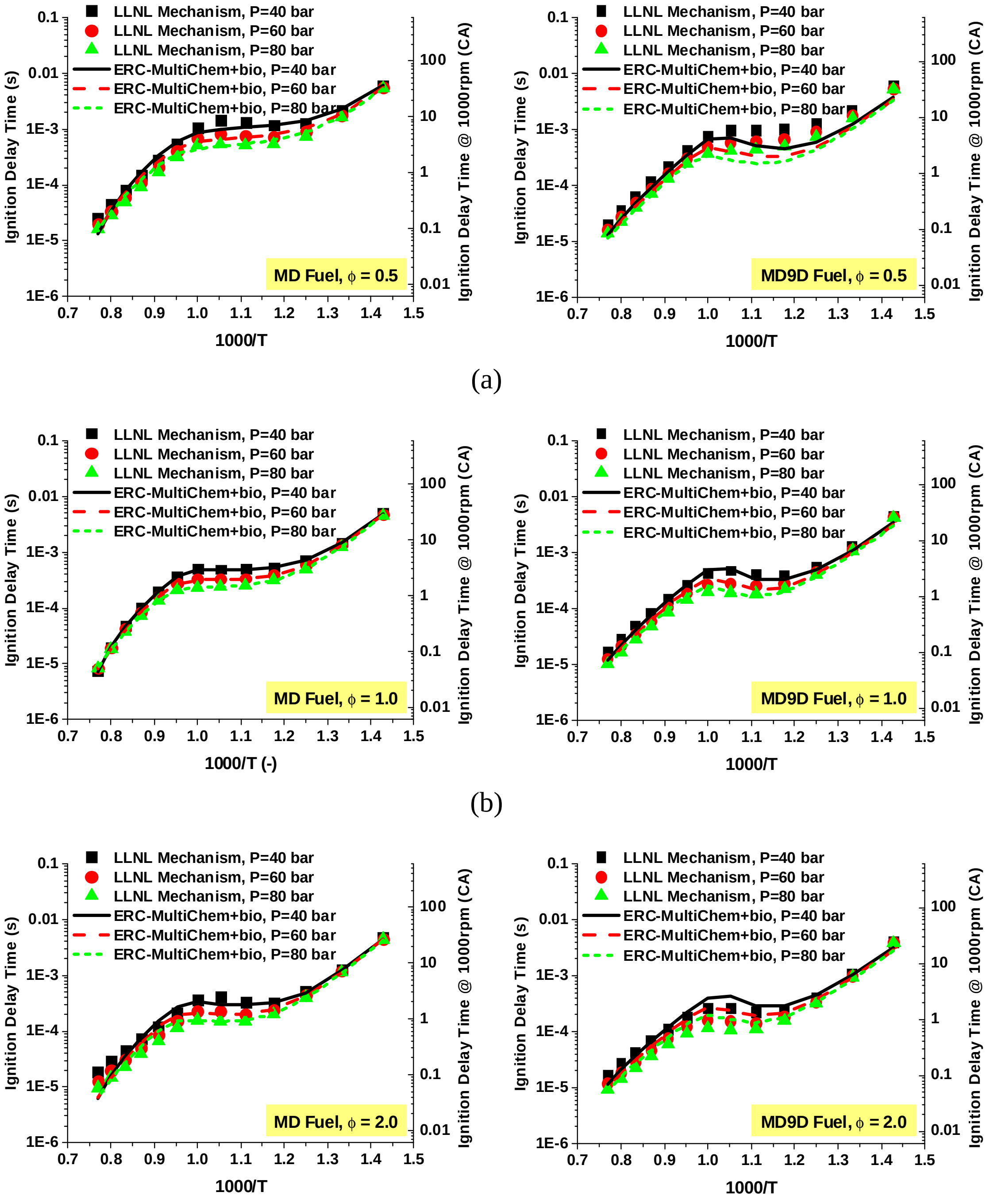

(a)

(b)

(c)

Figure 3-12: Ignition delay time validation for the ERC-MultiChem+MD/MD9D mechanism

As Table 3-4 shows, the maximum error for each fuel occurs at temperatures below 1000K under lean conditions. At this time, these errors were deemed acceptable considering the uncertainty in the detailed mechanism itself. With no biodiesel or MD/MD9D ignition data available, the LLNL researchers validated their mechanism against n-decane ignition data for a range of temperature and pressures, but only under stoichiometric conditions [59,60].

Table 3-4: Maximum error observed for the ERC-MultiChem+MD/MD9D mechanism

Conditions at Maximum Ignition Delay Error	**Fuel**	
	MD	**MD9D**
Pressure (bar)	40	40
Equivalence Ratio	0.50	0.50
Temperature (K)	950	850
LLNL Ignition Delay (s)	1440	1030
ERC Ignition Delay (s)	985	460
Ignition Difference (us)	455	570
Error (%)	**31.6**	**55.3**
Difference (CA*)	2.7	3.4

**assuming 1000 rev/min*

Chapter 4: Property Model Formulation and Validation

4.1 Physical Properties

As mentioned previously, the current KIVA code uses a discrete multi-component approach to model the physical properties of the fuel components. Properties of interest are listed in Table 4-1. Molecular mass, liquid density and heat of formation for each component were found in the Knovel Critical Tables online database [79]. Critical temperature and the remaining temperature-dependent property values for methyl palmitate, methyl stearate, and methyl oleate were found in the database maintained by the Design Institute for Physical Property Research (DIPPR) [41].

Much of the data for methyl linoleate and methyl linolenate were unavailable. Critical temperature values were found from Ref. [79] and the BDProp program developed at the University of Illinois at Urbana-Champaign [49,52] was used to calculate vapor pressure, density, heat of vaporization, and viscosity for these two fuels. This program estimates average biodiesel fuel properties based on a specified methyl ester composition. For the present study, the composition was set to 100% for the component of interest. Until more information becomes available, the thermal conductivity, specific heat, and diffusivity of methyl oleate were used for methyl linoleate and methyl linolenate. It is anticipated that the similar structure of the unsaturated species makes methyl oleate’s properties the most representative of the missing data.

Table 4-1: Physical properties required by the KIVA-DMC model

Property	**Reference**	
	C16:0, C18:0, C18:1	**C18:2, C18:3**
Molecular mass	[28]	
Liquid density	[79]	
Heat of formation	[79]	
Critical temperature	[41]	[79]
Latent heat of vaporization	[41]	[49]
Vapor pressure	[41]	[49]
Liquid specific heat	[41]	[49]
Surface tension	[41]	[49]
Liquid viscosity	[41]	[49]
Vapor thermal conductivity	[41]	*
Liquid thermal conductivity	[41]	*
Vapor diffusivity	[41]	*

**use methyl oleate properties*

The physical properties of the five components are similar in comparison to each other. However, some of the key properties of the biodiesel components are drastically different from those of diesel. Figure 4-1 compares the density, liquid viscosity, vapor pressure, and surface tension of the five biodiesel components and tetradecane ($C_{14}H_{30}$), a surrogate commonly used to represent diesel fuel properties in single-component diesel simulations. It is seen that biodiesel's liquid viscosity and surface tension are higher and the vapor pressure is much lower, which can lead to less spray break-up and poor evaporation compared to diesel. These properties, coupled with the high density of the fuel components, are expected to produce long liquid spray tip penetrations and potentially a significant amount of wall wetting in engine cases. The remaining physical properties listed in Table 4-1 are compared to tetradecane in Appendix A.

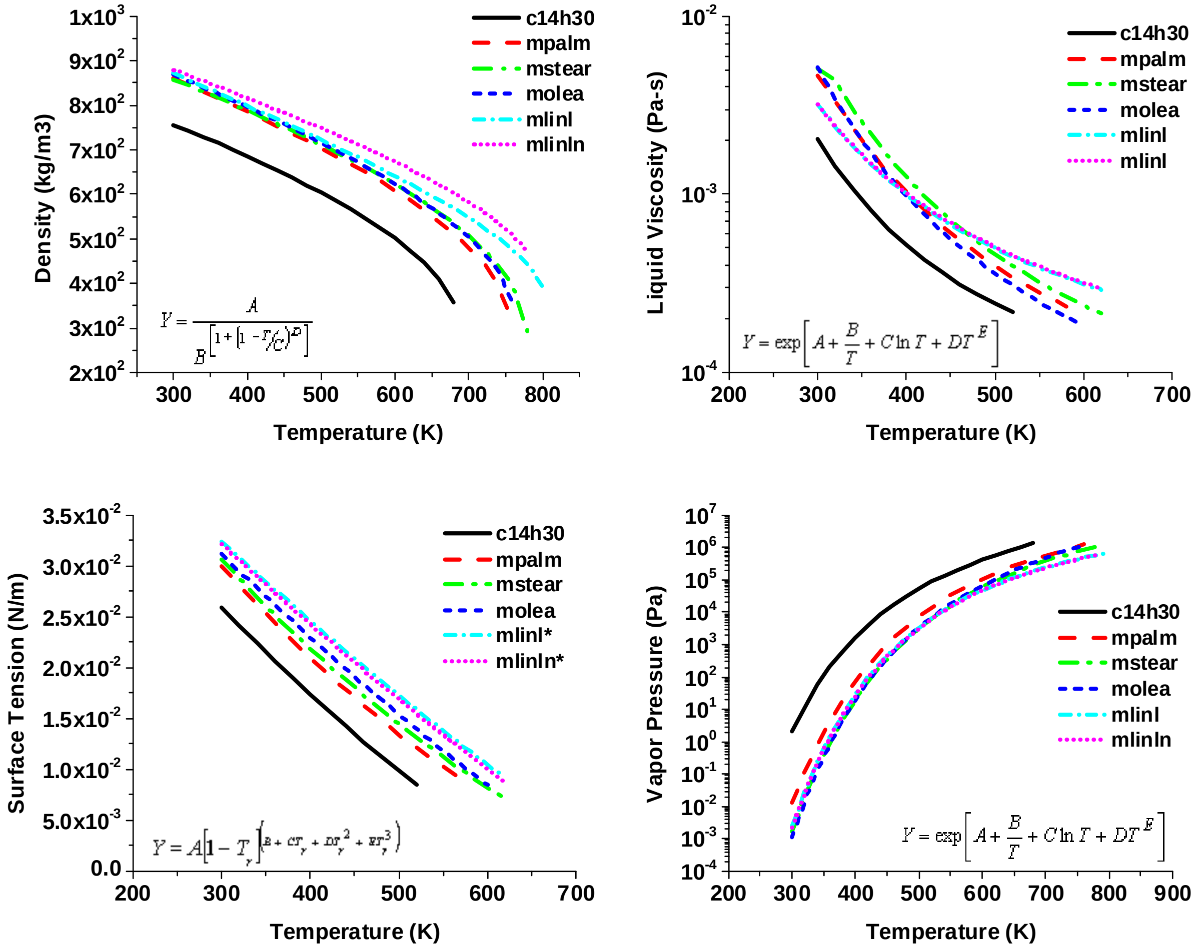

Figure 4-1: Physical property comparison for properties that greatly affect liquid penetration

A generic fuel composition was used with a single droplet model [80] to create the distillation curve seen in Figure 4-2. The boiling point temperatures of the five biodiesel fuel components are shown to the right of the curve with their respective simulated mass contribution. The simulation results are shown compared to experimental soy biodiesel distillation curves from Fisher et al. [81] and commercial soy biodiesel fuel of unknown composition from Ott and Bruno [82]. It should be noted that the boiling temperatures of these components are within 50K, which results in a nearly horizontal curve. Fisher et al. estimated the composition of their biodiesel, and that composition was used in the simulation. The composition of the commercial biodiesel fuel was not reported. The slight discrepancy between the model and literature is attributed to high molecular mass hydrocarbon species (i.e., higher boiling points) that may be present in the real fuel. Currently the biodiesel model only considers the five methyl esters mentioned previously and none of their boiling temperatures is high enough to improve the predicted distillation to match the experiments. Additional species may be included in the fuel surrogate in future studies to match the high temperature region.

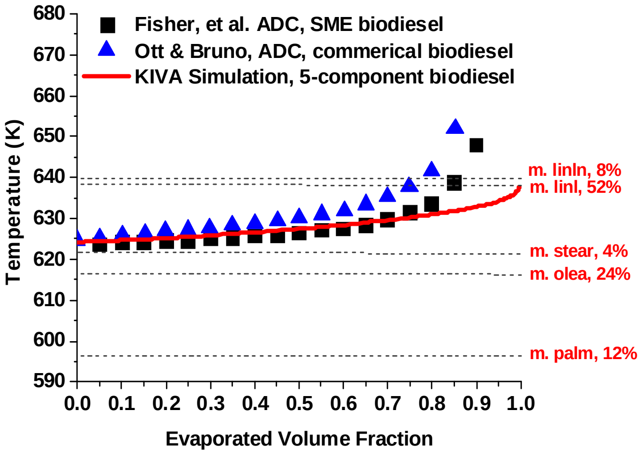

Figure 4-2: Comparison of simulated and experimental soy-based biodiesel distillation curves

In addition to the physical properties, it is also important to provide accurate thermodynamic data for each component to ensure proper estimates of enthalpy, entropy and specific heat. Researchers at the University of Orleans in France [83] have calculated the necessary thermodynamic data for common fatty acid methyl esters (FAME) and conveniently tabulated the data in NASA format. This data was applied in the biodiesel mechanism and assigned to generic fuel species in the mechanism that will later be linked to the two fuel species for chemistry. The heat of formation from this data was used to calculate the lower heating value

(LHV) of the fuel surrogate using the methyl ester composition reported in Ref. [84]. The paper reported a value of 37.4 MJ/kg and the model predicted a similar value of 37.7 MJ/kg.

4.2 Connecting Physical Properties to Chemistry

Fuel spray and vaporization processes are modeled in KIVA. Once a threshold temperature is reached (e.g., 600K), CHEMKIN is called and the vaporized fuel begins to react. For single-component fuels, KIVA would read the mechanism and connect the property surrogate to its appropriate chemistry surrogate in CHEMKIN. Unless otherwise specified, heat of formation values used to calculate the energy release in KIVA would come from the thermodynamic data provided by the mechanism. For the current multi-component simulations, five property surrogates and two chemistry surrogates are used to represent biodiesel. Since the number of property surrogates exceeds the chemistry surrogates, and it was necessary to add five “dummy” species to the mechanism. These species do not participate in any reactions; they simply make it possible to initially transfer appropriate thermodynamic data to the property species in KIVA.

Figure 4-3 depicts the relationship between the physical properties used by KIVA and the chemical species in CHEMKIN. The fuel preferentially vaporizes into five dummy species (mpalm, mstear, molea, mlinl, and mlinln) according to the physical properties assigned to each surrogate. The two saturated species, mpalm and mstear, are assigned to MD in CHEMKIN, while the unsaturated species react as MD9D. CHEMKIN performs the appropriate chemical reactions, and calculates new species production rates, then species concentrations are updated to

KIVA. Any remaining MD and MD9D species are divided back into their corresponding property surrogates in the proportions specified by their initial mass fractions.

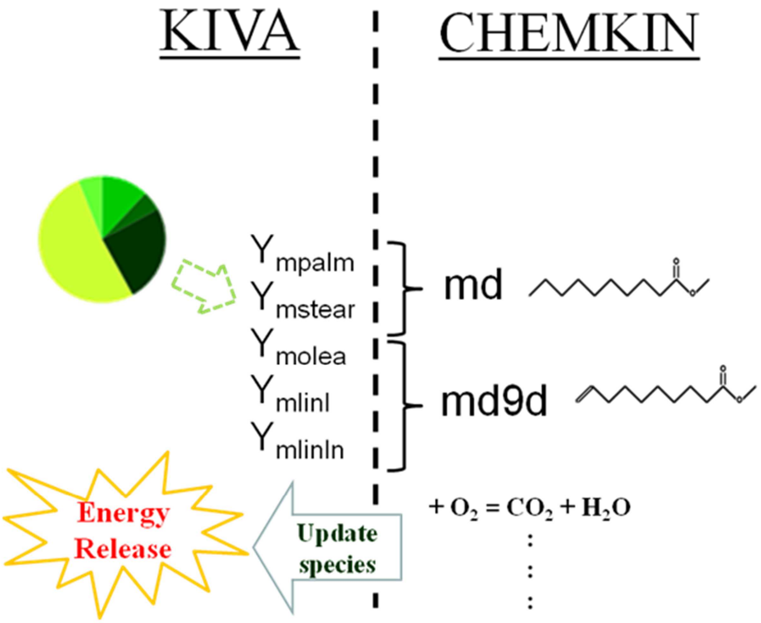

Figure 4-3: Pictorial description of connection between physical properties and chemistry in multi-component KIVA simulations for biodiesel fuel

4.3 Spray Validation

4.3.1 Constant Volume Liquid Length

The next step in the model development was to assess the spray characteristics of the fuel. Higgins et al. [85] studied the effect of physical properties on the liquid-phase penetration of several fuels. Experimental liquid penetration was measured in the constant volume spray chamber at Sandia National Laboratories (see Ref. [16]) using Mie-scattering. Figure 4-4 displays the experimental apparatus and the grid used in the simulation. The sprays were assumed to be axisymmetric, and the constant volume spray chamber was reproduced for the simulations using a 2-D sector representing half of the spray chamber. Figure 4-4(a) includes a dashed outline indicating the computational grid boundary and Figure 4-4(b) has a dot located in the position of the simulated injector.

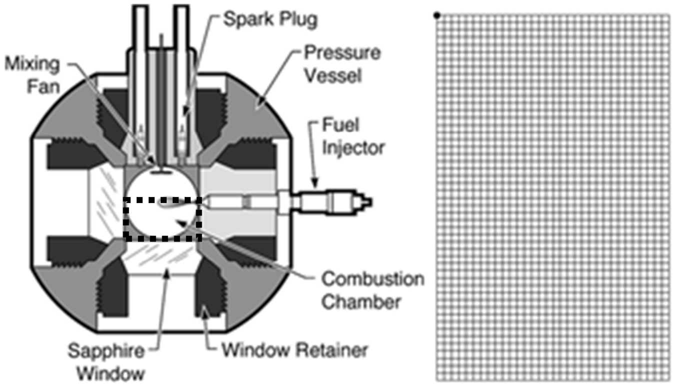

(a) (b)

Figure 4-4: (a) Sandia constant volume spray chamber [85] and (b) the 2-D axisymmetric computational grid used in the simulation

As shown in Table 4-2, the biodiesel fuel was tested at four densities and four temperatures that are representative of conditions seen in diesel engine operation. These were non-reacting experiments and an inert gas mixture was present in the cylinder prior to fuel injection. The injector orifice diameter, discharge coefficient, and the injection duration were also given. The fuel composition was not measured in the experiments and the authors assumed the following mass-fraction distribution for their correlation: 12% C16:0, 5% C18:0, 25% C18:1, 52% C18:2, and 6% C18:3. This composition was also applied in these simulations. Assuming an ideal gas, the known density and gas temperature were used to calculate the initial pressure for the simulations. A simple top-hat injection profile was assumed, and the injector characteristics and duration were used with the fuel density to determine the mass of fuel injected.

Table 4-2: Operating conditions and relevant specifications for the constant volume liquid length experiments of Higgins et al. [85]

Apparatus	Constant volume spray chamber
Gas mixture composition (mole fraction)	89.7% N_2, 6.5% CO_2, 3.8% H_2O
Gas temperatures	800, 900, 1000, 1100 K
Gas density	7.3, 14.8, 30.0, 45.0 kg/m^3
Injector orifice diameter	246 μm
Discharge coefficient	0.78
Injection duration	5.0 ms

The initial biodiesel spray simulations used the KH-RT spray constants originally applied in diesel spray cases. It was found that the simulations were able to capture the trend of increased penetration with decreased ambient density. However, liquid length was under-predicted for most conditions and the simulations were not able to capture the appropriate trend with varying temperature.

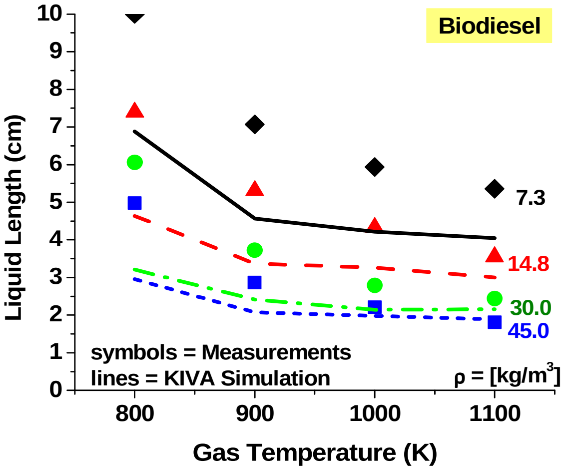

Figure 4-5: Comparison of constant volume liquid length measurements of Higgins et al. [85] (symbols) and predictions from KIVA simulations using standard KH-RT spray constants (lines)

The KH-RT spray constants are adjustable for different injectors and engine configurations. To assess the model's sensitivity to the parameters, the constants were changed by a factor of two and liquid length was recalculated. Figure 4-6-Figure 4-8 compare the liquid length of the experiments (symbols) to those predicted using the original (solid lines) and adjusted (dashed lines) spray constants. Figure 4-6 demonstrates the effect of the spray parameter B_1 (cnst22) in Equation (14). Decreasing from the default value of 40 to 20 caused a shorter primary breakup time, giving less time for droplets to grow. The smaller droplets vaporize sooner, which decreases the liquid length over the range of temperatures. Increasing cnst22 has an inconsistent effect on the liquid length for these conditions.

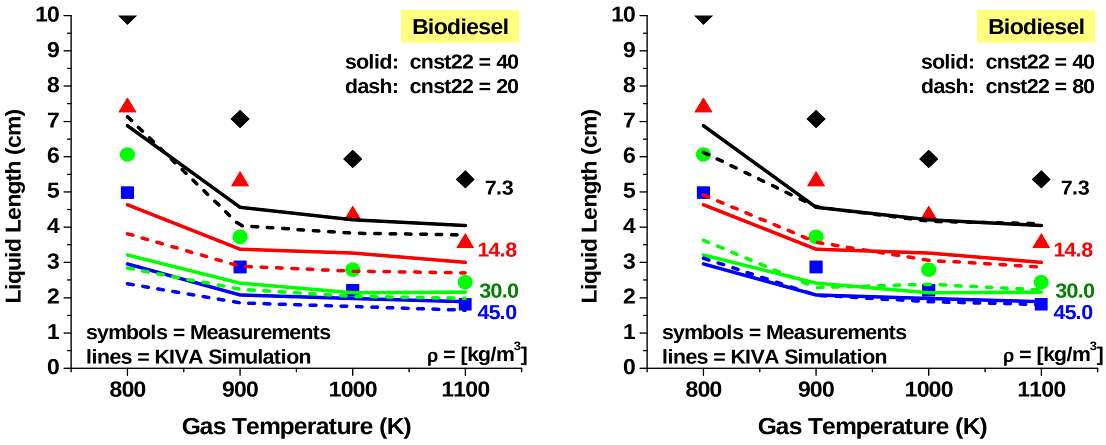

(a) (b)

Figure 4-6: Effect of (a) decreasing and (b) increasing the KH breakup time constant ("cnst22") by a factor of two

The C_b (distant) parameter seen in Figure 4-7 determines the transition point between the KH primary breakup and the RT secondary breakup regimes. This parameter has a drastic effect on both the liquid length and the temperature dependence. The shorter distant value causes secondary breakup to be achieved sooner. This also results in a significant reduction in liquid length with increased temperature, suggesting that the temperature dependence of the breakup model is mostly a function of the RT breakup regime. The longer distant value improves the penetration at lower temperatures, but nearly eliminates the temperature dependence.

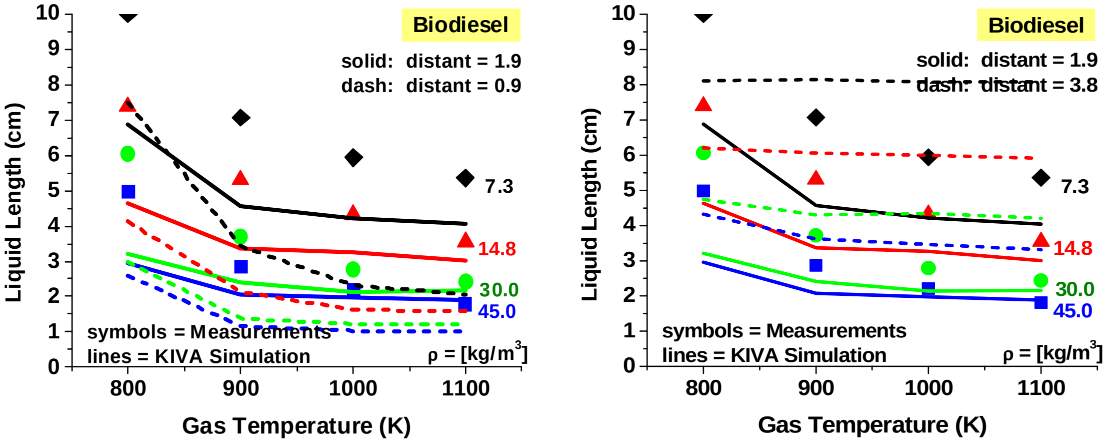

(a) (b)

Figure 4-7: Effect of (a) decreasing and (b) increasing the breakup length constant ("distant") by a factor of two

Figure 4-8 shows the effect of the C_{RT} (cnst3rt) in Equation (17). The smaller value causes smaller droplet radii once the secondary breakup regime is reached. The smaller droplets easily vaporize causing decreased liquid penetration. Increasing cnst3rt consistently increases the liquid length across the entire temperature range.

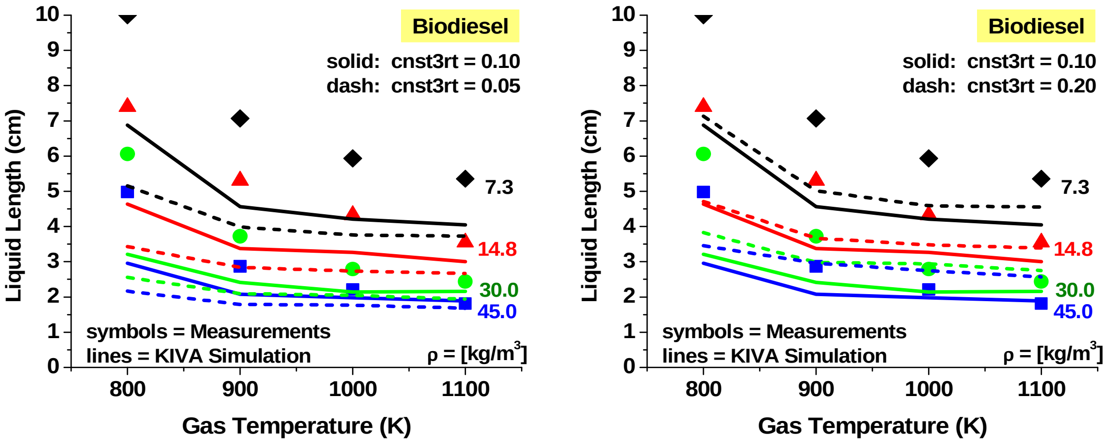

(a) (b)

Figure 4-8: Effect of (a) decreasing and (b) increasing the RT breakup size constant ("cnst3rt") by a factor of two

Using the sensitivity analysis as a guide, a trial-and-error method was used to find a combination of spray constant values that gave the greatest improvement to the liquid penetration predictions over the range of temperatures and densities. The smallest overall error occurred when distant remained at the standard value of 1.9, while both the KH and RT constants were doubled. As shown in Figure 4-9, the liquid length is improved for most conditions, though still under-predicted for the low density cases. It is expected that a closer agreement could be reached by expanding the sensitivity limit beyond a factor of two, but an exact match was not the goal of this comparison.

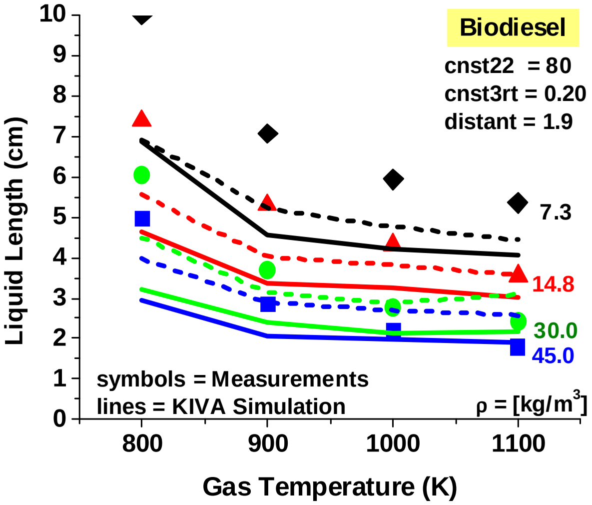

Figure 4-9: Comparison of constant volume liquid length measurements of Higgins et al. [85] (symbols) and predictions from KIVA simulations using standard (solid) and new (dashed) KH RT spray constants

4.3.2 Constant Volume Liquid Length, Composition Effects

The liquid length prediction for a fuel is composition-dependent. It was of interest to see the effect that various biodiesel compositions would have on liquid length. First, single-component simulations were performed to determine the liquid lengths predicted by individual biodiesel components. Standard KH-RT spray constant values were used in this comparison. Figure 4-10 compares the components at the 7.3 kg/m^3 ambient density condition. A similar trend was observed at all densities.

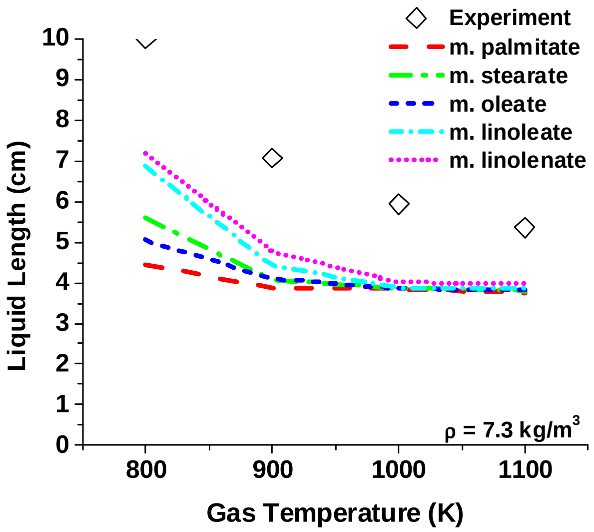

Figure 4-10: Liquid length predictions for individual biodiesel components at the ambient density condition of 7.3 kg/m^3

The differences observed between components can be attributed to the properties shown previously in Figure 4-1. Methyl palmitate has the highest vapor pressure, lowest density and lowest surface tension, and as a result, has the shortest liquid penetration. Methyl stearate and methyl oleate have similar vapor pressures, but methyl stearate has slightly higher density and viscosity, allowing it to penetrate further. Methyl linoleate and methyl linolenate have the highest densities and surface tensions, and the lowest vapor pressures. The higher density of methyl linolenate gives it the longest liquid length.

The next test compared the compositions of common biodiesels from three separate feedstocks [86]. Spray experiments by Fisher et al. [81] suggest that for multi-component fuels the liquid penetration is controlled by the least volatile components. Figure 4-11 illustrates the impact that feedstock has on the fuel composition. The fuels are listed in order of increased proportion of methyl linoleate and methyl linolenate (the least volatile components).

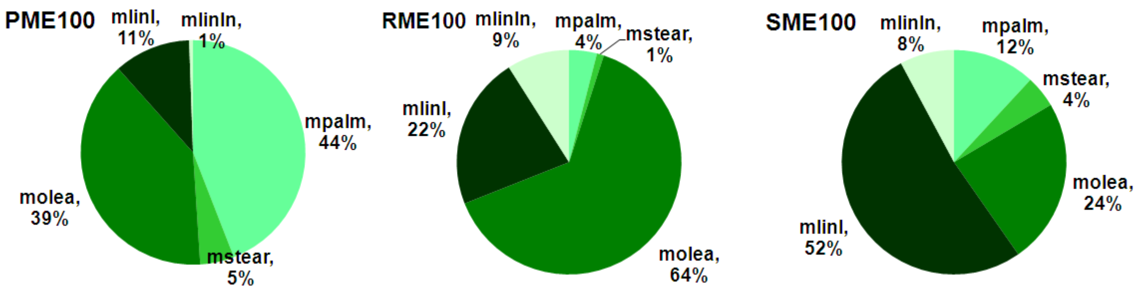

(a) (b) (c)

Figure 4-11: Composition of biodiesel fuels from three different feedstocks: (a) palm, (b) rapeseed, and (c) soy

Figure 4-12 shows the composition effect on liquid penetration. The highest density conditions resulted in very similar liquid lengths, and the 45 kg/m^3 cases were not included to improve clarity of the figure. The multi-component liquid lengths are consistent with the single-component predictions in Figure 4-10. Palm methyl ester (PME100) has the lowest methyl linoleate/linolenate content (12%) and penetrates the least. Rapeseed methyl ester (RME100) and soy methyl ester (SME100) contain 31% and 60% of the low-volatility components, respectively, giving SME the longest liquid length.

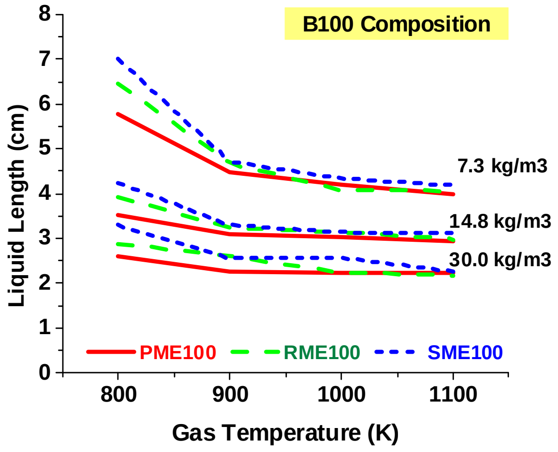

Figure 4-12: Comparison of liquid length predictions for biodiesel fuels from different feedstocks

4.3.3 Unsteady Spray Liquid Lengths

The constant volume results are valuable, but a single maximum liquid length value does not account for the rate of fuel injected and how quickly or slowly it penetrates in-cylinder. Fisher et al. [81] performed unsteady spray experiments in the Sandia Compression-Ignition Optical Research Engine (SCORE). In the experiments, liquid penetration lengths were measured for soy methyl ester (SME) biodiesel fuel injected into time-varying in-cylinder conditions. The effect of injection pressure, intake manifold pressure, and injection timing were considered. Table 4-3 and Table 4-4 show the relevant engine and fuel injection system specifications, respectively. Table 4-5 contains the engine operating conditions for the spray cases. Injection rate profiles were provided and the fuel mass was calculated by integrating the injection rate curves for each case.

Table 4-3: Engine specifications for the SCORE

Engine type	Single-cylinder CAT 3176
Cycle	Four-stroke CIDI
Bore x Stroke	125 mm x 140 mm
IVC	-153° aTDC
EVO	116° aTDC
Connecting rod length	225 mm
Piston bowl diameter	90 mm
Piston bowl depth	16.4 mm
Squish height	1.5 mm
Swirl ratio	0.59
Displacement	1.72 L
Compression ratio (geo.)	12.3:1

Table 4-4: Fuel-injection system specifications for the SCORE

Injector type	CAT HEUI A
Injector model	HIA-450
Nozzle style	Single-guided VCO
Hole pattern	2 x 0.108 mm
Included spray angle	140°
Max. fuel injection pressure	71 MPa, 142 MPa
Pressure intensification ratio	6.85:1

Table 4-5: Engine operating conditions for unsteady SCORE spray experiments

Engine speed	1500 rev/min
Intake mixture	4.0% O_2, 1.5% CO_2, 94.5% N_2
Coolant temperature	80°C
Intake manifold temperature	116°C (69°C simulated)
Intake manifold pressure	1.65 bar, 2.48 bar
Start of injection	-50º to +10º aTDC
Duration of injection	~4.5 ms (~41 CAD)

The standard KH-RT spray breakup constants were applied in an initial simulation of the baseline case with low boost pressure, low injection pressure and the earliest SOI timing (P_{boost}=1.65bar, P_{inj}=71MPa, and SOI=-50^{o}aTDC). The results are shown in Figure 4-13, where the horizontal line indicates the field-of-view limit in the experiment. The simulation captures the trend of an initial steep rise in penetration, followed by a decrease as the compression stroke increases in-cylinder pressure and density. The magnitude of the liquid length is under-predicted, which is consistent with the constant volume results shown previously. At this early injection timing, the peak liquid length occurs during the first five crank angle degrees and the initial large discrepancy carries through the rest of the injection period.

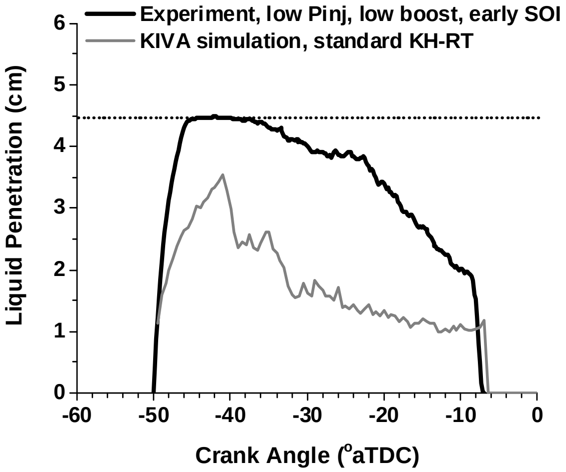

Figure 4-13: Prediction of liquid length for the baseline unsteady SCORE spray case; simulations use original KH-RT spray breakup constants

First, the discharge coefficient was investigated to see if allowing more fuel to exit the nozzle (larger discharge coefficient) would increase the initial liquid length prediction. Figure 4-14 shows that the overall penetration increases slightly, but the discharge coefficient does not impact the initial injection period.

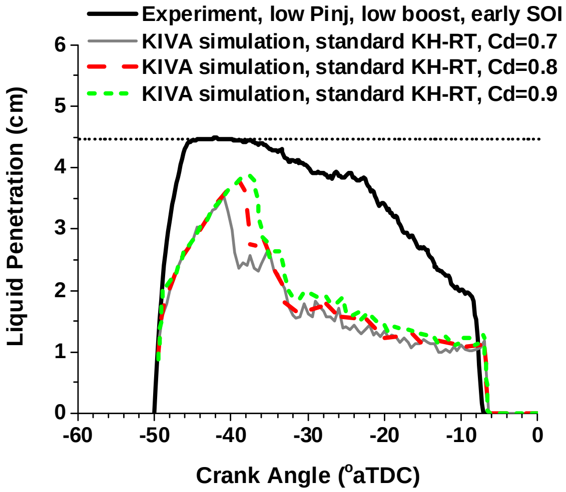

Figure 4-14: Effect of adjusting discharge coefficient for the baseline unsteady SCORE spray case; simulations use original KH-RT spray breakup constants

Figure 4-15 shows the result of applying the spray breakup constants identified in the constant volume simulations discussed previously. Liquid length is increased similar to adjusting the discharge coefficient. However, these results suggest that a different set of spray breakup constants may be required for the unsteady simulations.

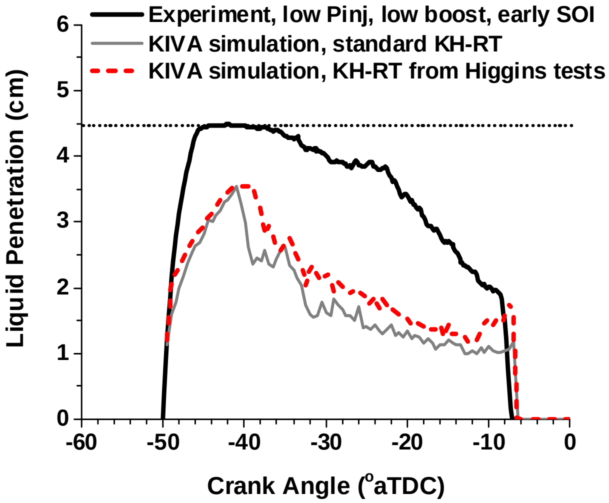

Figure 4-15: Comparison of liquid length predictions using standard (light grey, solid) KH-RT spray breakup constants and new (dashed) constants identified in the constant volume simulations.

A breakup constant sensitivity analysis was performed for the unsteady spray cases as was done for the constant volume cases. As displayed in Figure 4-16, only the breakup length (distant) has a significant effect on the liquid length for these cases. Increasing distant allows the simulation to remain in the primary KH breakup stage longer, where the large “blob” indicative of this regime can quickly penetrate. In fact, it is clear from Figure 4-16(c) that the distinct change in model’s liquid length prediction observed around -48^{o} aTDC is indicative of the transition between KH and RT break-up in the model.

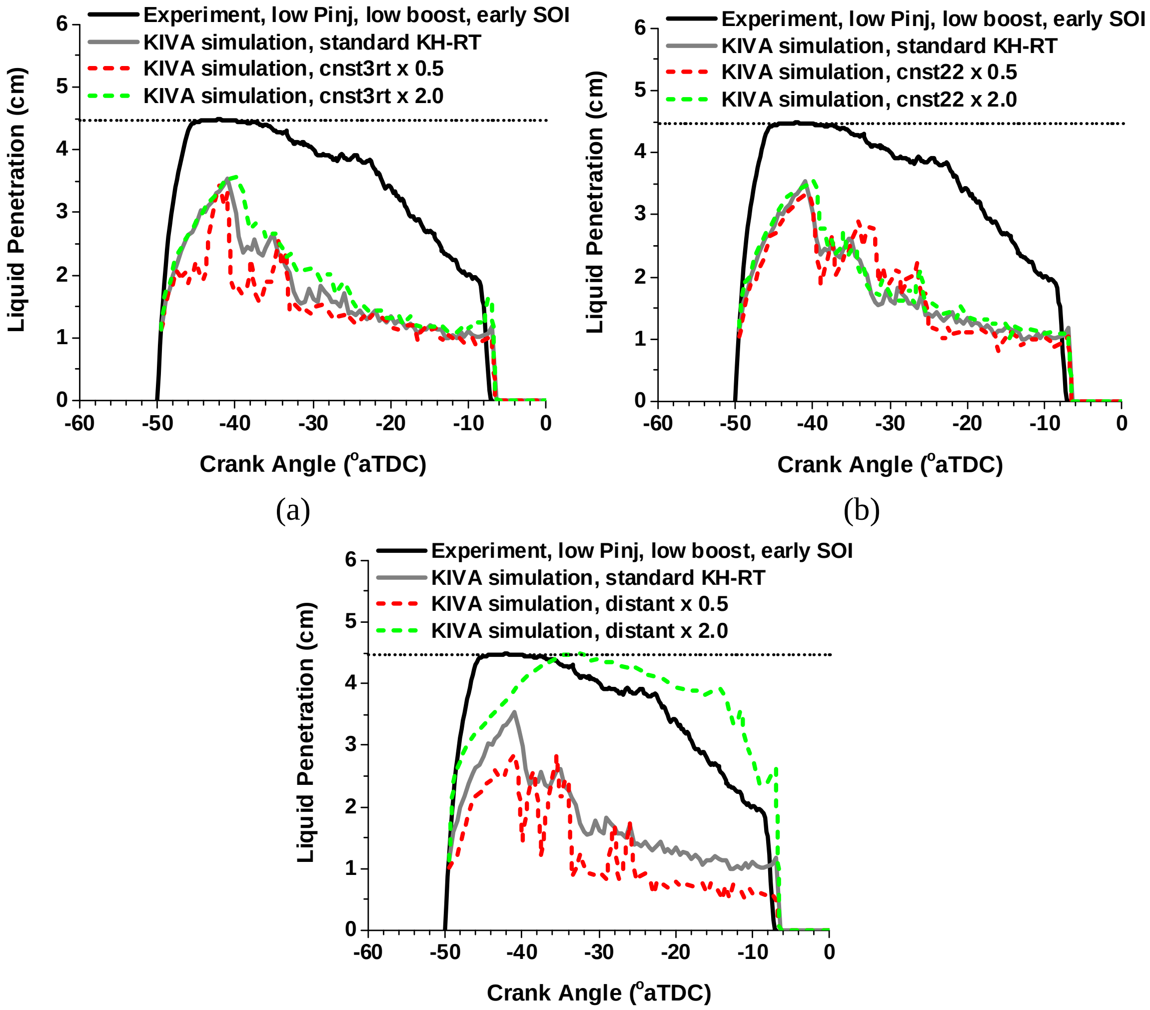

(a)

(b)

(c)

Figure 4-16: Effect of adjusting the (a) KH time constant, cnst22, (b) RT size constant, cnst3rt, and (c) breakup length, distant

The breakup length was then increased to achieve the appropriate early liquid penetration. From Figure 4-17 it is clear that a breakup length greater than 4.5 is required to keep the spray in primary breakup to achieve the appropriate maximum liquid penetration. This large value, however, causes the rest of the injection period to be over-predicted. Once the maximum is reached, the secondary RT breakup then needs to produce smaller droplets that are more susceptible to vaporization. Figure 4-18 confirms this theory requiring a new RT breakup size constant that was one-quarter its standard value.

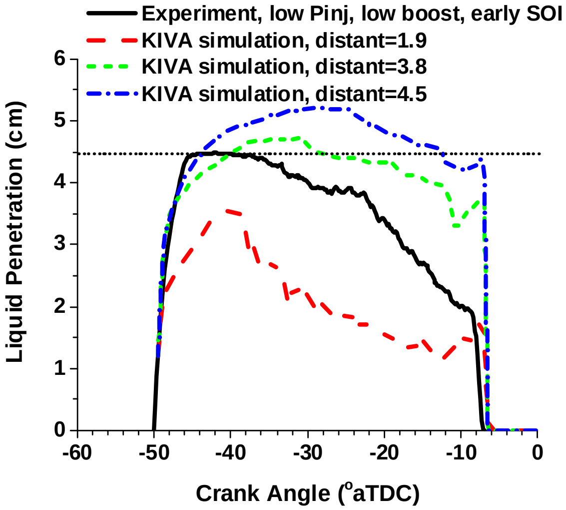

Figure 4-17: Effect of increasing breakup length (distant) for the baseline unsteady SCORE spray case; the KH-RT spray breakup constants cnst22=80, cnst3rt=0.2 from the constant volume tests.

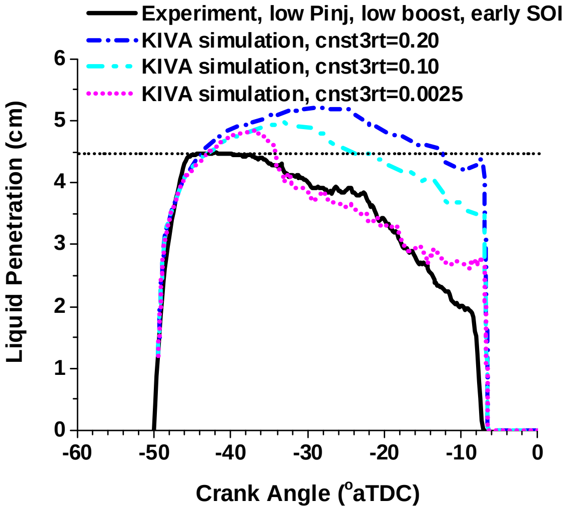

Figure 4-18: Effect of reducing RT breakup size (cnst3rt) for the baseline unsteady SCORE spray case; the remaining KH-RT spray breakup constants are cnst22=80, distant=4.5.

These new constants were applied over the remaining unsteady tests covering the changing injection pressure, boost pressure and SOI timings. Figure 4-19 shows the liquid length comparisons for different injection timings at low injection and low boost pressures. The magnitudes of the liquid length predictions match the experiments well and the simulation is able to capture the effect of delayed injection timing. Similar agreement is seen at the higher boost and injection pressures as well. Those results are shown in Figure A-3 of Appendix A.

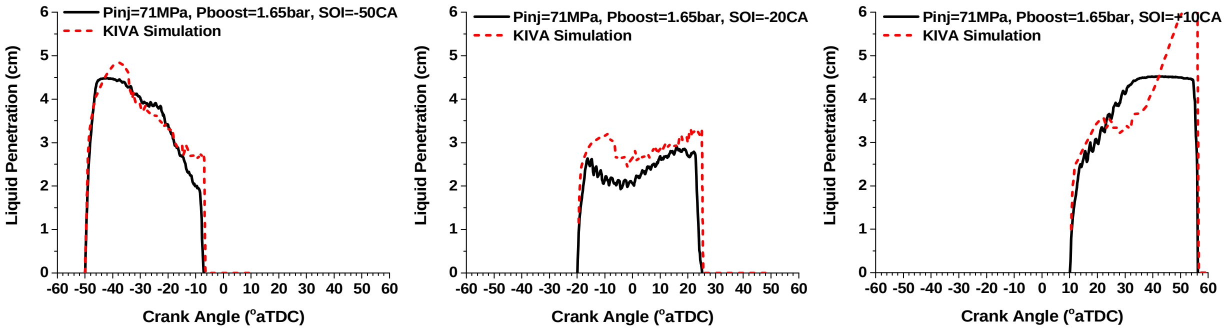

(a) (b) (c)

Figure 4-19: Liquid lengths predicted for unsteady SCORE spray cases: P_{inj}=71 MPa and P_{boost}=1.86 bar; uses spray break-up constants: cnst22=80, cnst3rt=0.025, and distant=4.5

Figure 4-20 and Figure 4-21 show the effect of boost pressure at the early SOI timing and low and high injection pressures, respectively. Part (a) of each figure shows the effect of the experiments and part (b) shows the simulation results. The simulations capture the trends well, with increased boost pressure reducing the liquid length compared to the low boost condition. The experiments and the simulations found that the injection pressure had very little effect on the liquid length. These results are shown in Figure A-4 and Figure A-5 of the Appendix.

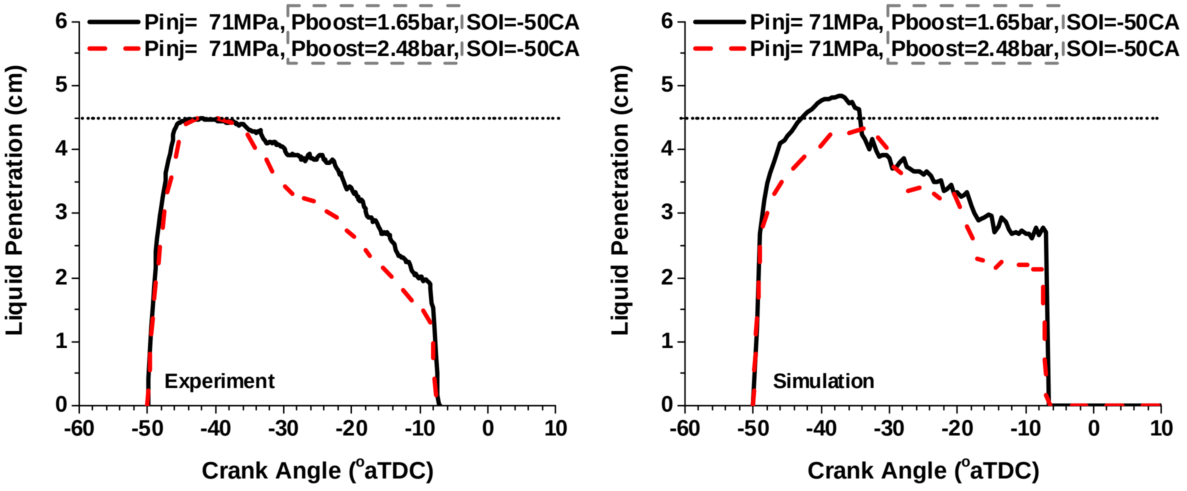

(a) (b)

Figure 4-20: Boost pressure effect on liquid lengths (a) measured and (b) predicted for unsteady SCORE spray cases at P_{inj}=71 MPa and SOI=-50°aTDC; uses spray break-up constants: cnst22=80, cnst3rt=0.025, and distant=4.5

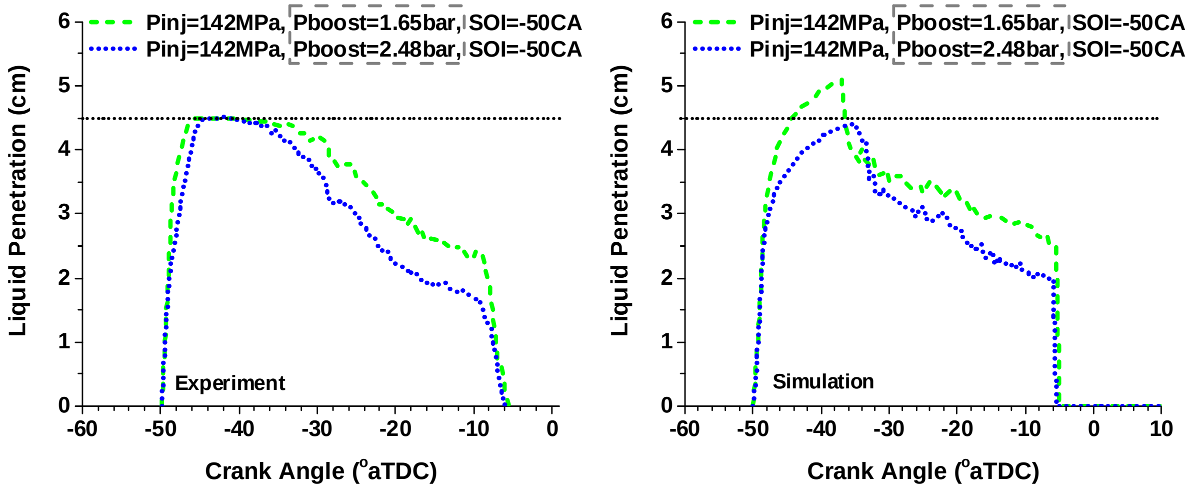

(a) (b)

Figure 4-21: Boost pressure effect on liquid lengths (a) measured and (b) predicted for unsteady SCORE spray cases at P_{inj}=142 MPa and SOI=-50°aTDC; uses spray break-up constants: cnst22=80, cnst3rt=0.025, and distant=4.5

A very large breakup length was required to achieve the liquid length magnitude for these unsteady cases. Unfortunately, the same breakup length cannot be applied to the constant volume conditions, as shown in Figure 4-22. These results suggest that there is not one set of optimal spray parameters applicable to all simulation conditions. Instead, the values should be can be adjusted, using the results of this section as a guide, for the injector and piston geometry used in a particular case. The SCORE is a relatively large engine with a large nozzle orifice, and it is expected that the spray will penetrate very far in a short period of time. However, an engine with a smaller bore would certainly require a smaller distant value to ensure that the RT break-up regime is initiated before impingement. For the remaining simulations, unless otherwise specified, the standard KH-RT constants were applied.

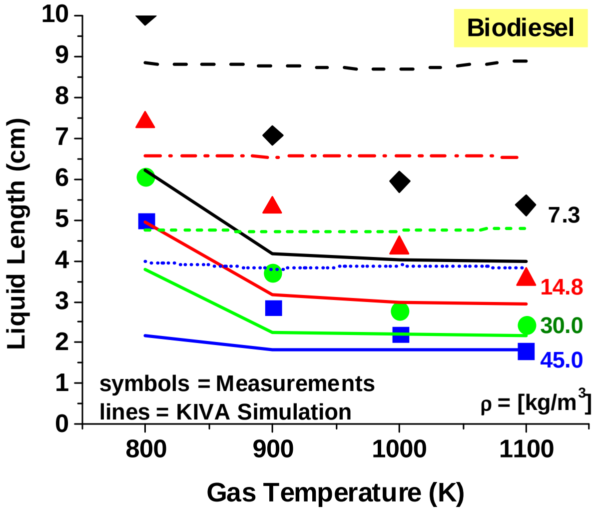

Figure 4-22: Constant volume penetration predictions compared to spray experiments of Higgins et al. [85]; uses KH-RT spray constants identified in unsteady simulations: cnst22=80, cnst3rt=0.025, distant=4.5

Chapter 5: Engine Validation

5.1 Conventional Combustion

The biodiesel model was applied to engine simulations and compared to experimental data to test its performance. The experiment chosen for this work [63] was the same used to validate previous biodiesel combustion models [61,66]. The experiments were performed in the SCORE operating under a conventional diesel combustion strategy, with injection near top dead center (TDC) and zero EGR. Four low-speed, high-load conditions were tested. The computational grid, seen in Figure 5-1, contained about 13200 cells that were 3 mm in the radial direction.

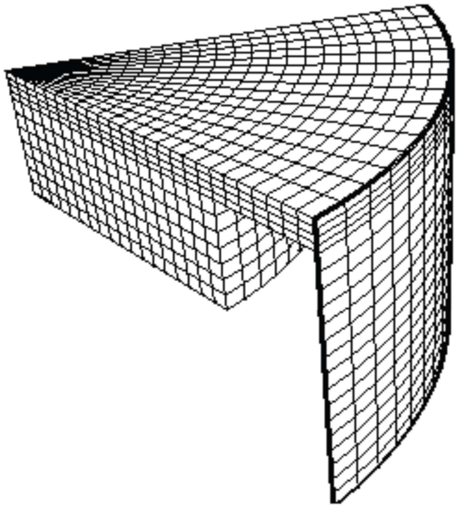

Figure 5-1: SCORE grid used in conventional combustion simulations

Table 5-1 shows the operating conditions and relevant engine parameters. An injection rate profile from a previous SCORE experiment was used to estimate profiles for the given injection durations [87].

Table 5-1: Experimental operating conditions and engine specifications for conventional combustion cases [63]

Parameter	**Value**
Engine type	Single-cylinder CAT 3176
Bore x stroke	125mm x 140 mm
IVC	-153^o aTDC
EVO	116^o aTDC
Connecting rod length	225 mm
Piston bowl diameter	90 mm
Piston bowl depth	16.4 mm
Swirl ratio	0.59
Displacement	1.72 L
Compression ratio	11.3 : 1
Engine speed	800 rev/min
Time of injection	-1.1^o aTDC
Intake air pressure	2.3 bar
Engine loads	10-16 bar gIMEP
EGR	None

Pressure and heat release rate were compared to the experiments for the four load conditions and the profiles are shown in Figure 5-2. The simulations and experiments were well matched for all the cases, which indicate a good representation of biodiesel spray and combustion for these conditions.

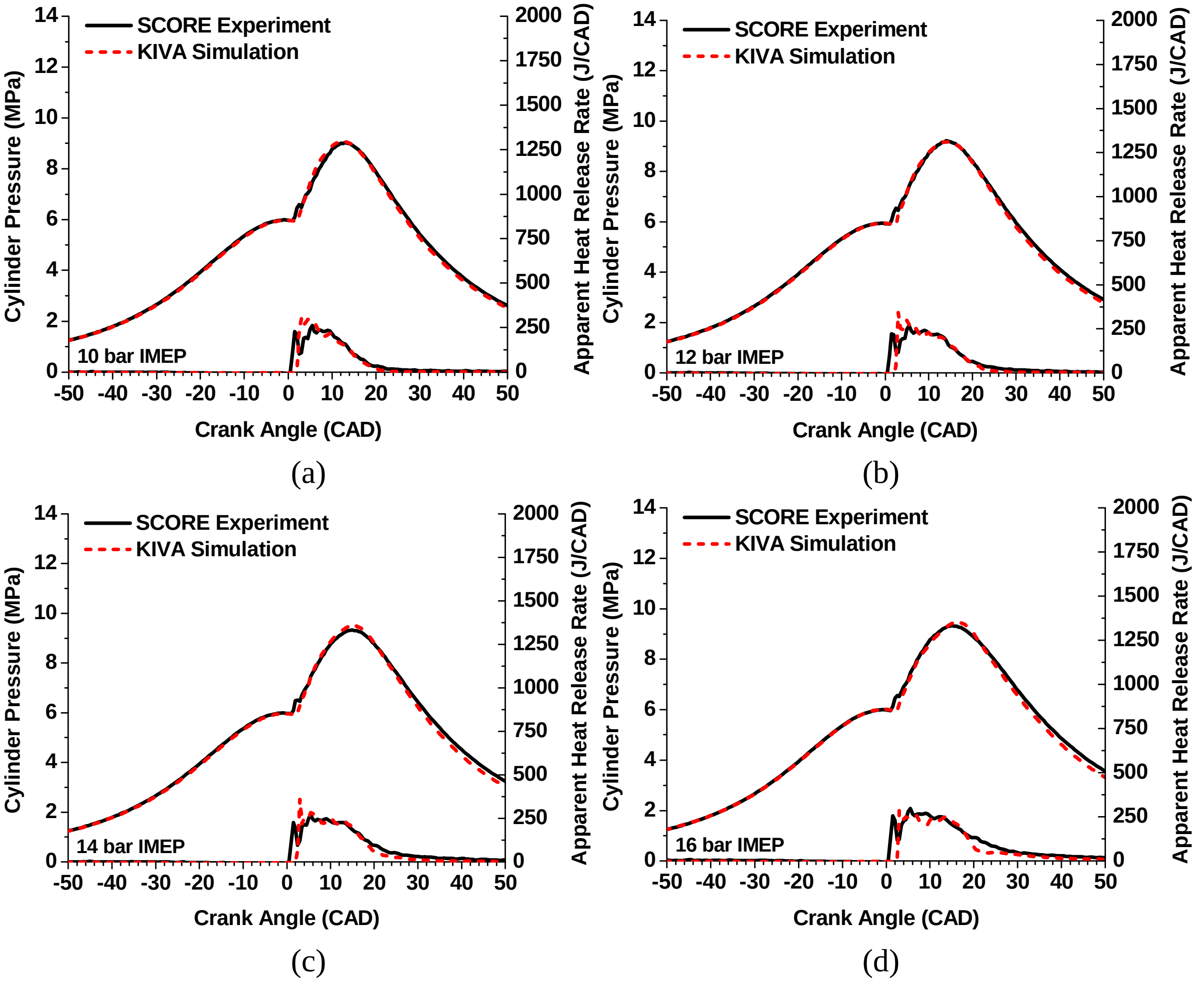

Figure 5-2: Pressure and heat release rate validation for the four loads: (a) 10bar IMEP, (b) 12 bar IMEP, (c) 14 bar IMEP, (d) 16 bar IMEP

NOx was also measured at each load condition. Here, NOx is the combination of the NO and NO_2 species. Figure 5-3 compares the experimental NOx measurement and that predicted by the current and previous ERC biodiesel models. The triangles represent the previous model of Brakora et al. [61], which used a single-component mixture of methyl butanoate and n-heptane to represent the fuel chemistry. The circles represent the current multi-component model described in this work. The current model improves the magnitude of the NOx prediction and more effectively captures the trend of decreasing NOx with increased load.

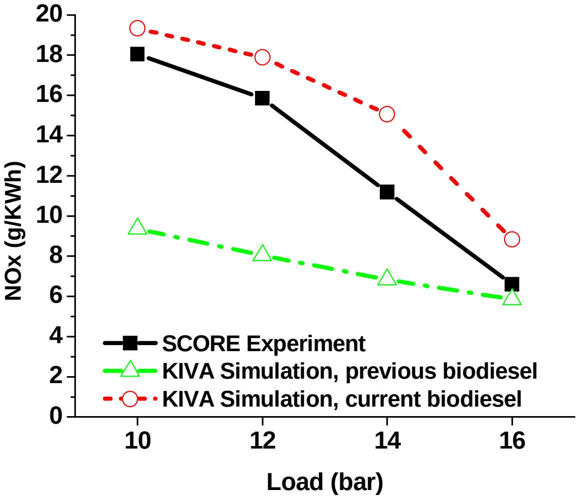

Figure 5-3: NOx (as NO+NO_2) comparison between the experiment, the previous KIVA biodiesel model (triangles) [61], and the current KIVA biodiesel model (circles)

In order to gain a better understanding of the NOx trend observed with increasing load, the temperature and NOx histories were investigated using the current model. The average in-cylinder temperature was highest for the highest load condition, and the peak temperatures remained high as a result of the high fueling and long fuel injection duration adding energy later in the cycle. One would expect the higher temperatures to lead to higher NOx. However, NOx is lowest for that condition due to the late end-of-injection timing and its effect on the local oxygen concentrations, as described next.

Figure 5-4 shows that near 20^{o} aTDC, the low load condition finishes injecting and the energy release and O_2 predictions of the four load cases begin to diverge. Injections for the higher load conditions continue, and the fuel oxidation releases more energy and decreases the amount of oxygen available for NOx formation.

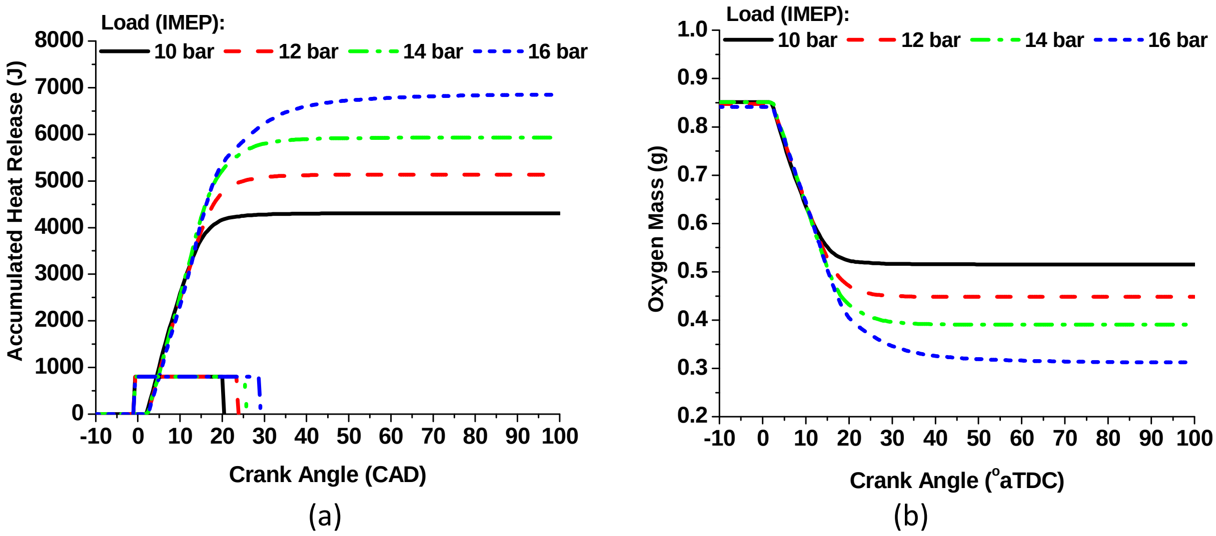

Figure 5-4: Comparison of (a) accumulated heat release and (b) oxygen mass for each load condition

In-cylinder images were generated to compare the NOx and oxygen mole fractions for each of the conditions. Figure 5-5 shows that at 10° aTDC the oxygen and NOx distributions look very similar for each load condition. By 30° aTDC, the oxygen and NOx distributions for each load are distinctly different. It can be seen that the areas of low oxygen correspond to the region of the spray where fuel oxidation occurs. NOx formation also occurs in this region due to the high temperatures. These images confirm that in the later crank angles, the higher load cases have less oxygen available in this region and therefore, lower NOx.

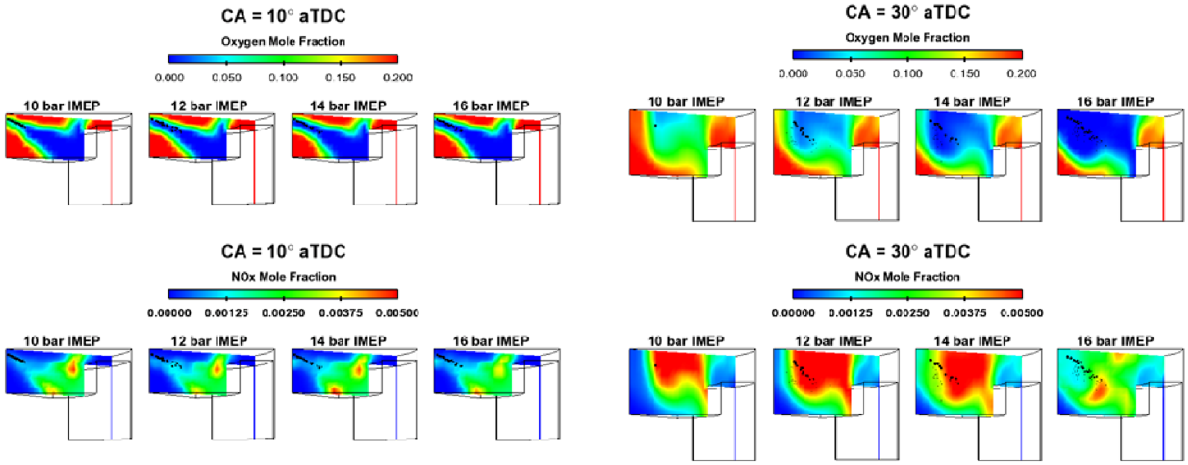

(a) (b)

Figure 5-5: In-cylinder oxygen and NOx distributions for each load condition at (a) 10° aTDC and (b) 30° aTDC

The improved NOx trend observed with the current KIVA biodiesel model indicates that it provides a more realistic distribution of in-cylinder O_2 for each load condition. Figure 5-6 compares the oxygen distribution between the current (a) and previous (b) biodiesel models and it is seen there is a distinct difference in O_2 availability between loads in the current model, while very little difference is seen between loads for the previous model. This oxygen distribution improvement is likely the combined result of more realistic spray and vaporization, as well as more representative fuel chemistry.

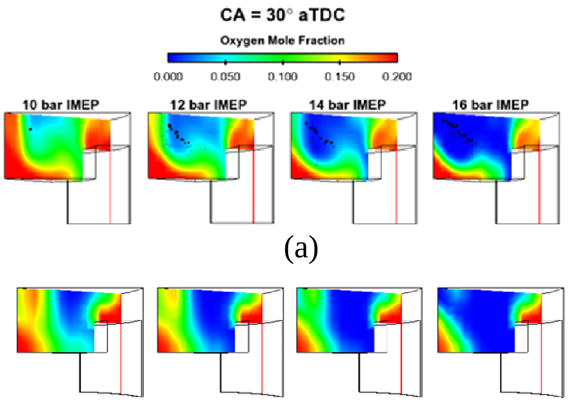

(a)

(b)

Figure 5-6: Comparison of the oxygen distribution for each load in the (a) current and (b) previous biodiesel models

5.2 Preliminary Low-Temperature Combustion

Tran [88] investigated the effects of biodiesel on low temperature combustion (LTC) using a light-duty diesel engine at a low-load and high-speed conditions. The engine is a single-cylinder version of the GM 1.9L production engine. Specifications are listed in Table 5-2. The computational grid for the simulations, shown in Table 5-2, consists of 10470 cells that average 1.5 cm in the radial direction.

Table 5-2: Engine specifications used for LTC cases

Parameter	**Value**
Engine type	GM 1.9L
Bore x stroke	82 mm x 90.4 mm
IVC	-132°aTDC
EVO	112°aTDC
Swirl ratio	2.2
Displacement	0.474 L
CR	16.6 : 1

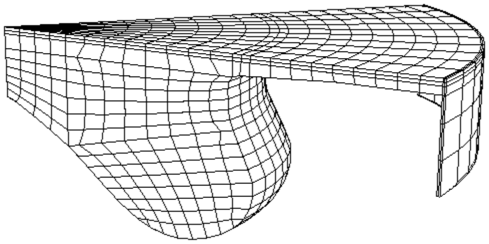

Figure 5-7: Computational grid for GM 1.9L engine

Two biodiesel fuels, soy methyl ester (SME) and palm methyl ester (PME), were tested as blends (B20) and compared to diesel fuel. The soy methyl ester was also compared as B100. Over a range of injection timings, the experiments found that the biodiesel blends generally showed little change in CO, but improved HC, NOx, and smoke emissions compared to the diesel fuel. These LTC experiments were performed at a load of 5.5 bar nIMEP, speed of 2000 rpm, and an inlet O_2 concentration of 9.5% (~67% EGR). These were identical conditions to those performed by Opat et al. [19] and Koci et al. [20,89] when they investigated fuel effects in the same engine. Other relevant operating conditions are shown in Table 5-3.

Table 5-3: Engine operating conditions for LTC cases

Parameter	**Value**
Engine speed	2000 rpm
Engine load	5.5 bar nIMEP
SOI	-40 to -22° aTDC
EGR	~67%
Fuel type	Diesel, SME, PME
Intake temperature	65° C
Intake pressure	162 kPa abs

5.2.1 Diesel LTC

Previously, Ra et al. successfully simulated the experiments of Opat et al. [19] and Koci et al. [89] for diesel fuel, and the first step was to reproduce the similar diesel combustion cases of Tran's experiments [88]. The author provided post-processed results, which included pressure, heat release rate, and emissions results, as well as specific input conditions (e.g., fuel mass) for start of injection (SOI) timings of -40° to -22° aTDC in two degree increments. Also included were injection rate shapes for diesel and neat biodiesel fuels for a range of injection pressures and durations. The diesel indicated durations were around 600 μs for all injection timings.

Figure 5-8 below shows the given experimental injection rate profiles for two indicated injection durations and the two injection commands. For diesel fuel and this injector, there is a 374 μs delay between the injection command and the actual start of injection. In addition, the injection event lasts longer than the indicated durations as the nozzle closes.

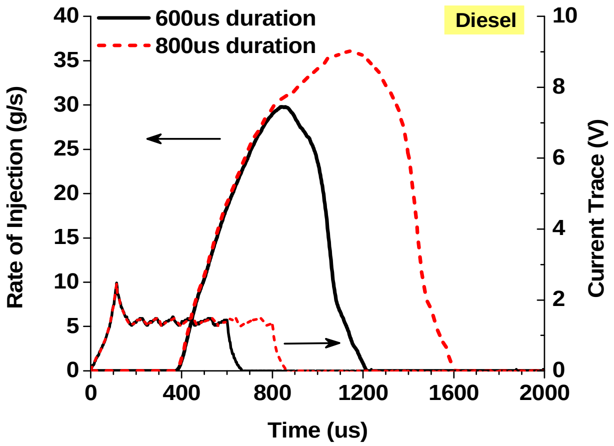

Figure 5-8: Experimental injection rate profiles for diesel fuel at two indicated injection durations (600 μs and 800 μs) for the GM engine

The 800 μs profile was used to create the injection profile for simulating each SOI timing case. The rising and falling slopes of the experimental profile were maintained, while the peak rate and duration were adjusted until the integrated profile matched the given fuel mass for each case. Figure 5-9 gives example profiles for the -36°, -30°, and -22° SOI timing diesel fuel cases. The indicated durations for these three cases were 603, 592, and 583, respectively. The fuel masses, indicated durations, and actual (i.e., simulated) durations for all cases are given in Table 5-4.

.

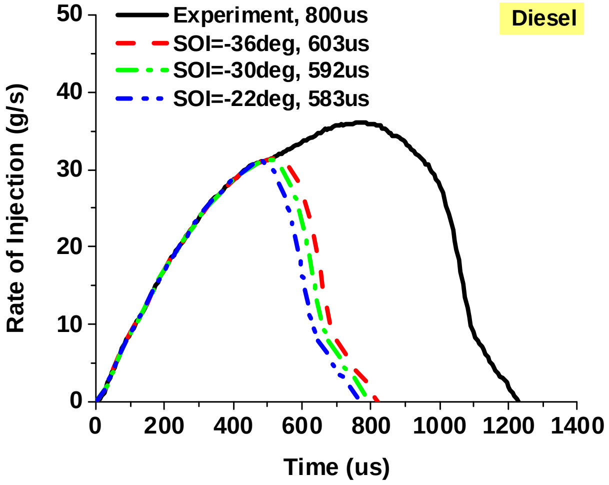

Figure 5-9: Rate of injection profiles for three SOI timings using diesel fuel

Table 5-4: Rate of injection information used for each diesel fuel LTC case

SOI Timing (^{o} aTDC)	**Fuel Mass (mg)**	**Indicated Duration (μs)**	**Calculated Duration (μs)**	**Indicated Duration (CAD)**	**Calculated Duration (CAD)**
-40	15.40	616	849	7.37	10.15
-38	14.87	611	831	7.31	9.94
-36	14.75	603	825	7.21	9.86
-34	14.37	599	813	7.16	9.72
-32	14.02	594	807	7.10	9.65
-30	13.83	592	801	7.08	9.58
-28	14.02	590	807	7.06	9.65
-26	13.64	589	795	7.04	9.50
-24	13.14	585	777	7.00	9.29
-22	13.05	583	771	6.97	9.22

The target EGR rate was 67% and the experiments provided the specific EGR percentages used in each case. These values did not account for residual mass trapped in-cylinder following IVC. The output did include an estimate of the residual mass, and this was added to the exhausted species to calculate a higher EGR percent. For each SOI timing simulation, an EGR percent within the range of the given and adjusted values was chosen to best capture the experimental performance. Table 5-5 provides the initial IVC pressures provided by the experiments, IVC temperatures estimated using polytropic compression and adjusted as needed to match ignition timing, and EGR percents that were used in the simulations.

Table 5-5: Initial conditions for diesel fuel LTC simulations

SOI Timing (^{o} aTDC)	**IVC Pressure (bar)**	**IVC Temperature (K)**	**EGR Percent (%)**
-36	1.919	355	73
-34	1.915	360	70
-32	1.909	355	69
-30	1.912	360	69
-28	1.917	360	69
-26	1.918	360	70
-24	1.909	360	70
-22	1.909	360	70

Initial simulations revealed two mechanism concerns for diesel combustion. First, the n-heptane portion of the ERC-MultiChem base mechanism was intended to be one of multiple components of diesel, instead of a single-component surrogate for diesel fuel. As a result, the mechanism's author adjusted the n-heptane reactions to represent real n-heptane fuel, which led to delayed ignition in these single-component diesel simulations. A previous ERC-PRF mechanism developed by Ra et al. [90] was designed to use iso-octane and n-heptane species as single-component surrogates for gasoline and diesel, respectively. The n-heptane reaction rate parameters from that PRF mechanism were applied in the MultiChem mechanism for single-component diesel simulation. Figure 5-10 shows the effect that these rate constant changes have on the pressure and heat release for an SOI timing of -30^o aTDC.

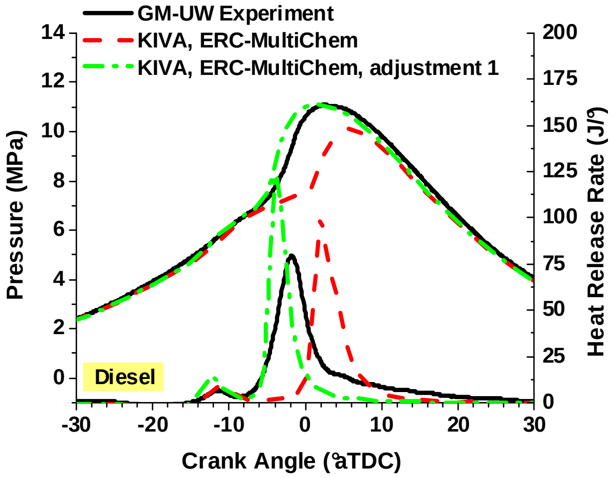

Figure 5-10: Effect of n-heptane rate constant adjustments to represent single-component diesel fuel

A second adjustment was also needed to further improve the pressure and heat release rate predictions of the diesel simulations. It was found that several lower-level reactions were added to the PRF mechanism when developing the MultiChem mechanism. Among them, the pressure-dependent *ch3o(+m)=ch2o+h(+m)* reaction had a significant effect on the energy release, causing a drastic spike in pressure and heat release rate. This reaction was important for the biodiesel portion of the mechanism, and the rate constant was reduced by two orders of magnitude instead of removing it. This was the largest reduction possible, without greatly impacting the MD and MD9D ignition timings. Figure 5-11 displays the effect of reducing the rate constant.

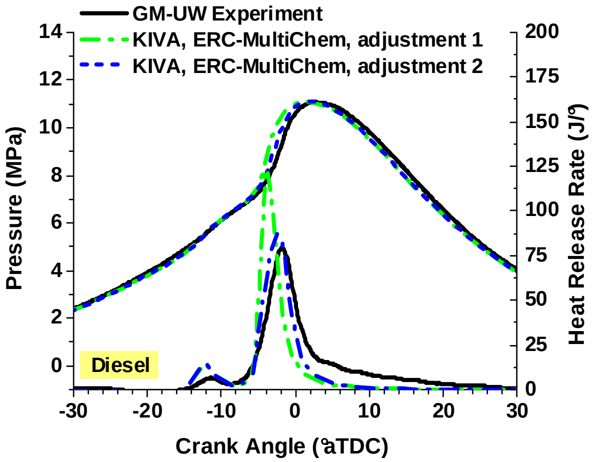

Figure 5-11: Effect of reducing the *ch3o(+m)=ch2o+h(+m)* rate constant by two orders of magnitude to improve single-component n-heptane combustion

Once the chemistry issues were resolved, simulations for the sweep of diesel SOI timings successfully reproduced the experiments in terms of fuel consumption and emissions. Figure 5-12 shows the pressure and heat release rate predictions for three representative SOI timings. Similar agreement is seen for the -36° to -22° cases and the individual results are found in Appendix A.

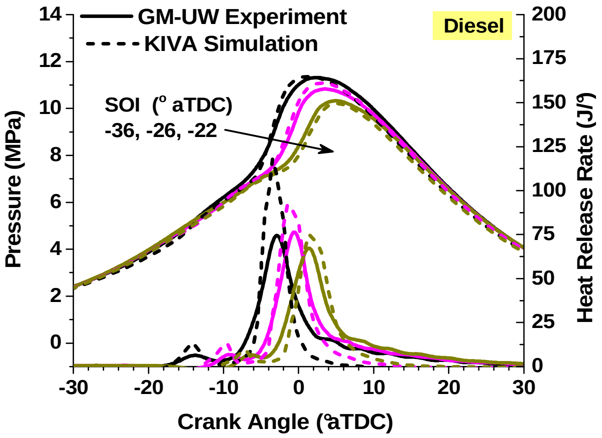

Figure 5-12: Pressure and heat release rate predictions for the diesel SOI timings of -36°, -26° and -22° aTDC

Previous simulations of the work by Opat et al. [19] helped identify a “sweet spot” for reduced CO that occurs for SOI timings near -33° aTDC. At this point, the injection angle is such that the fuel penetrates to the piston pip and CO is formed with access to the oxygen available in both the squish and bowl regions. Figure 5-13 shows good agreement between the experimental emissions and fuel consumption results and those predicted by the simulations, including the subtle CO “sweet spot” around -30° aTDC.

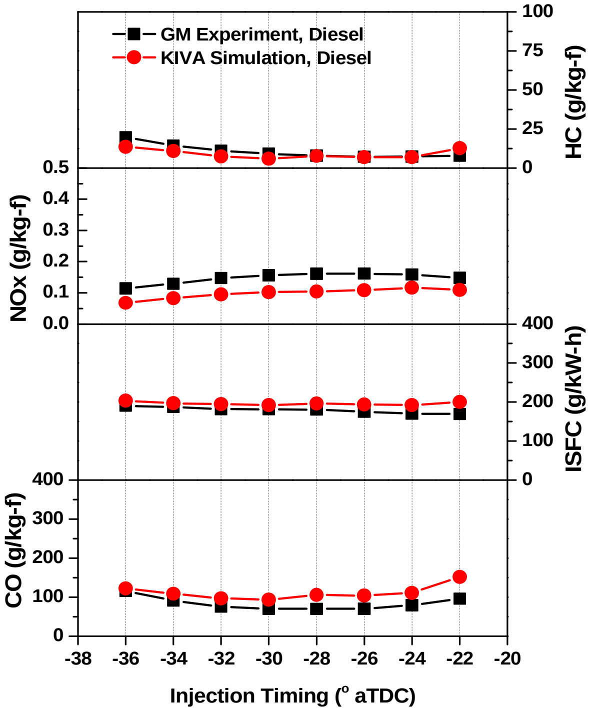

Figure 5-13: Emissions and fuel consumption for the diesel SOI timings of -36° to -22° aTDC

The results for the SOI timings of -40° and -38° aTDC were not included in the results. The simulations were not able to capture the appropriate energy release without significant adjustment to the initial conditions. The pressure and heat release rate shown in Figure 5-14 are for the -40° aTDC SOI timing using the maximum EGR percent as calculated using the given EGR rate and the residual mass. Despite the low oxygen availability, the fuel is too reactive and the energy release is very over-predicted.

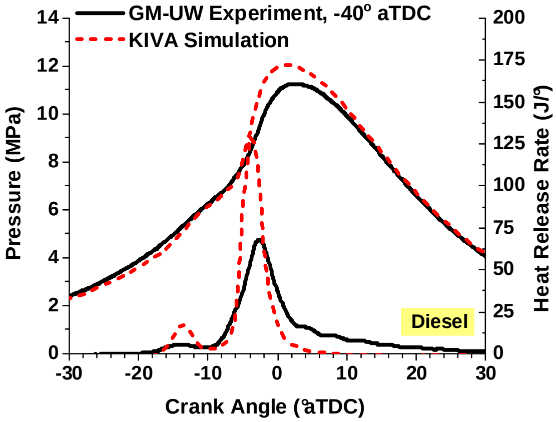

Figure 5-14: Impact of excessively vaporized fuel on pressure and heat release for -40° aTDC SOI timing

In the experiments, the early SOI timings had relatively high fuel consumption values. The work of Opat et al. [19] and Koci et al. [20,89] indicate that a significant amount of fuel impinges on the piston for these timings, which may contribute to reduced vaporization and combustion efficiency. Figure 5-15(a) shows that the mass of fuel in the experiment increased as SOI advanced, which could indicate that more fuel was injected to achieve the desired load and overcome the fuel trapped on the piston. Impingement is confirmed for the -40° aTDC SOI timing simulation in Figure 5-15(b). However, despite the impingement, the fuel becomes fully-vaporized in the simulation and reacts very well.

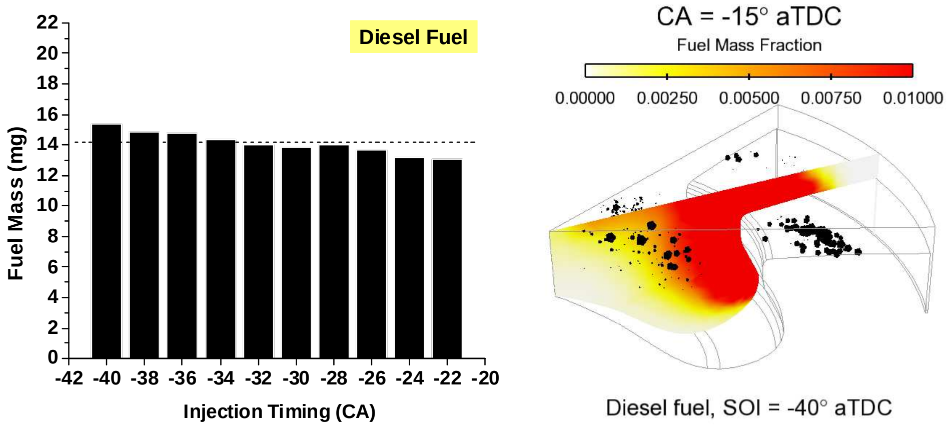

(a) (b)

Figure 5-15: (a) Fuel injected, and (b) in-cylinder view of spray impingement for the -40° aTDC SOI timing

To prevent the excessive energy release, two methods were tested and the results are shown in Figure 5-16. The first test reduced the amount of fuel injected to match the average of the diesel SOI cases (dotted line in Figure 5-15(a)). This required a 10% reduction in fuel. The reduced fueling successfully reduced the amount of fuel available to react, but the ISFC became much lower than the experiments. Alternatively, the EGR percent was increased from the 73% with the reported residual mass to 77%, reducing the oxygen fraction to 0.73. This strategy reduced the reactivity of the vaporized fuel and the pressure and heat release are improved, but the CO, and HC were much lower than the experiments, which eliminated the SOI timing trends. Similar behavior was seen in early SOI timings of the biodiesel cases. Inconsistencies with wall impingement and vaporization from the wall were beyond the scope of this work and for the present study, the earliest SOI timing cases were simply not included.

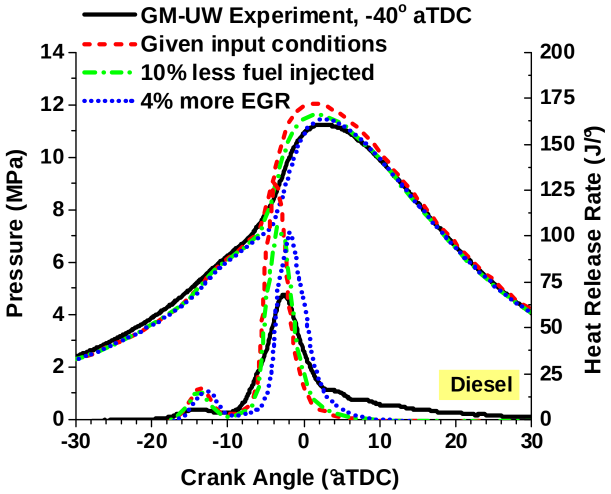

Figure 5-16: Effect of reducing the amount of fuel injected (dash-dot) and increasing the EGR (dot) for the -40° aTDC SOI timing

5.2.2 Preliminary LTC for Neat and Blended Biodiesel

The experiments included neat soy methyl ester biodiesel, denoted SME100, and 20% biodiesel blends for both soy and palm methyl esters, denoted SME20 and PME20, respectively. The biodiesel cases included additional SOI timings, but for the sake of comparison, simulations were only performed for the same timings as the diesel LTC experiments. The experiments provided mass-based compositions for the neat SME and PME fuels that included 17 species. For computation purposes, the species were binned into groups of the five main biodiesel methyl esters. Table A-5 in the Appendix shows the experimental composition, as well as the binned and normalized composition values used in the simulations. For the neat biodiesel simulations, the SME mass fractions shown in Table 5-6 were directly applied to represent the five physical property components.

Table 5-6: Mass fraction composition applied in LTC simulations for SME100

Property **Species**	**Composition** **SME**
m. palmitate	0.1189
m. stearate	0.0459
m. oleate	0.2384
m. linoleate	0.5185
m. linolenate	0.0783

The biodiesel blend simulations use six components to represent the physical properties. A mass-averaged density was calculated for B100 and a mixture of 20% biodiesel and 80% diesel (as tetradecane) by volume was used to determine the mass fractions. Table 5-7 shows the physical property composition applied in the simulations for the two biodiesel blends.

Table 5-7: Mass fraction composition applied in preliminary LTC simulations for B20 blends

Property	**Composition**	
Species	**SME**	**PME**
m. palmitate	0.0267	0.0984
m. stearate	0.0103	0.0109
m. oleate	0.0535	0.0881
m. linoleate	0.1164	0.0246
m. linolenate	0.0176	0.0013
tetradecane	0.7756	0.7768

Figure 5-17 shows that for a given experimental injection duration, the biodiesel had a similar profile shape as that of the diesel fuel, though the biodiesel injections exhibited a slightly longer delay (400 μs) between command and actual SOI. The SOI timing was delayed in the simulations to reflect the actual time that fuel injected in the experiments.

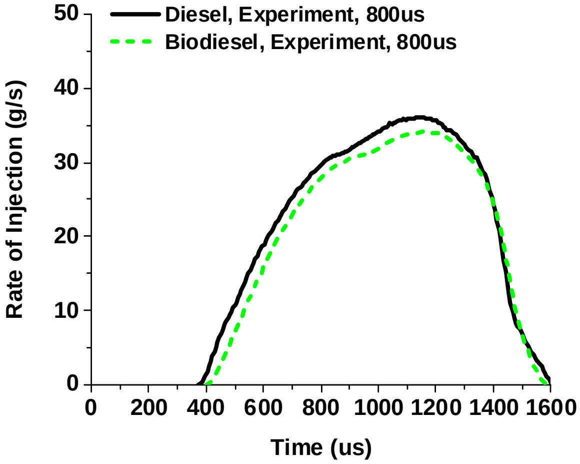

Figure 5-17: Comparison of biodiesel and diesel fuel injection profiles as provided by the experiments of Tran [88]

As was done in the diesel cases, the peak and duration of the biodiesel profiles were adjusted until the integrated fuel mass matched that specified by the experiments. While the injection profiles for the two fuels fuel were similar, the biodiesel cases required more fuel than diesel, resulting in longer injection durations. Table 5-8 provides the fuel mass, indicated duration, and actual (i.e., simulated) duration for each simulated SOI timing case. The diesel injection profile was used as the baseline for the B20 fuels, but the fuel mass and duration differed for each blend. Table 5-9 and Table 5-10 list the rate of injection information for the SME20 and PME20 blends.

Table 5-8: Rate of injection information used for each SME100 fuel LTC case

SOI Timing (^{o} aTDC)	**Fuel Mass (mg)**	**Indicated Duration (us)**	**Calculated Duration (us)**	**Indicated Duration (CAD)**	**Calculated Duration (CAD)**
-40	19.78	686	981	8.20	11.74
-38	18.45	668	939	7.99	11.23
-36	17.70	655	915	7.83	10.94
-34	17.12	643	897	7.69	10.73
-32	16.35	634	873	7.58	10.44
-30	16.18	631	867	7.55	10.37
-28	16.36	630	873	7.53	10.44
-26	15.97	627	861	7.50	10.30
-24	16.06	625	867	7.47	10.37
-22	16.08	625	867	7.47	10.37

Table 5-9: Rate of injection information used for each SME20 fuel LTC case

SOI Timing (^{o} aTDC)	**Fuel Mass (mg)**	**Indicated Duration (us)**	**Calculated Duration (us)**	**Indicated Duration (CAD)**	**Calculated Duration (CAD)**
-40	16.01	622	867	7.44	10.37
-38	15.86	616	861	7.37	10.30
-36	15.11	608	837	7.27	10.01
-34	14.78	600	831	7.17	9.94
-32	14.50	596	819	7.13	9.79
-30	14.57	596	819	7.13	9.79
-28	14.52	596	819	7.13	9.79
-26	14.30	593	813	7.09	9.72
-24	14.23	593	813	7.09	9.72
-22	14.06	588	807	7.03	9.65

Table 5-10: Rate of injection information used for each PME20 fuel LTC case

SOI Timing (^{o} aTDC)	**Fuel Mass (mg)**	**Indicated Duration (us)**	**Calculated Duration (us)**	**Indicated Duration (CAD)**	**Calculated Duration (CAD)**
-40	16.23	622	873	7.44	10.44
-38	15.83	615	861	7.35	10.30
-36	15.24	607	843	7.26	10.08
-34	15.00	602	837	7.20	10.01
-32	14.58	597	825	7.14	9.86
-30	14.52	597	819	7.14	9.79
-28	14.42	593	819	7.09	9.79
-26	13.99	589	801	7.04	9.58
-24	14.10	588	807	7.03	9.65
-22	13.94	585	801	7.00	9.58

Preliminary simulations were performed on the -30° aTDC SOI timings for each fuel. Figure 5-18 compares the B20 pressure and heat release rate predictions to the experimental results. The ignition timing, pressure and heat release rate predictions are well-matched for these two blends. This agreement was expected, since a majority of the fuel is diesel.

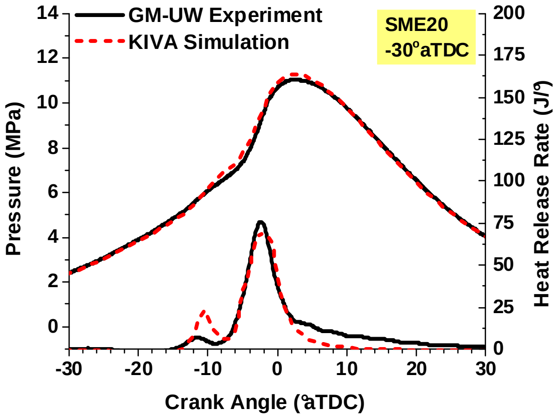

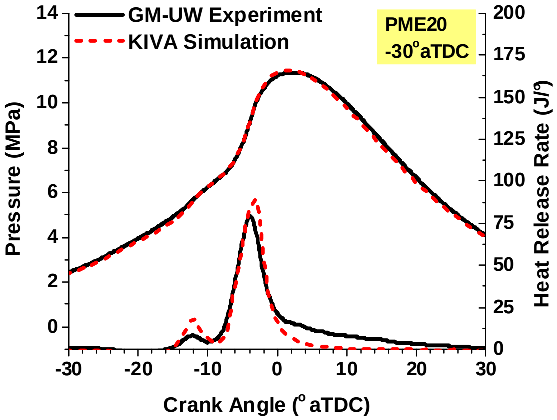

(a) (b)

Figure 5-18: Preliminary pressure and heat release predictions for -30° aTDC SOI timing using (a) SME20 and (b) PME20 fuels

A neat biodiesel case was run to see how the simulation performed with zero n-heptane in the fuel composition. Figure 5-19 shows acceptable ignition timing, but an over-prediction of first-stage, low-temperature heat release and poor combustion following main ignition. Several tests were performed to determine if proper combustion could be achieved with improvements to the physical or chemical properties.

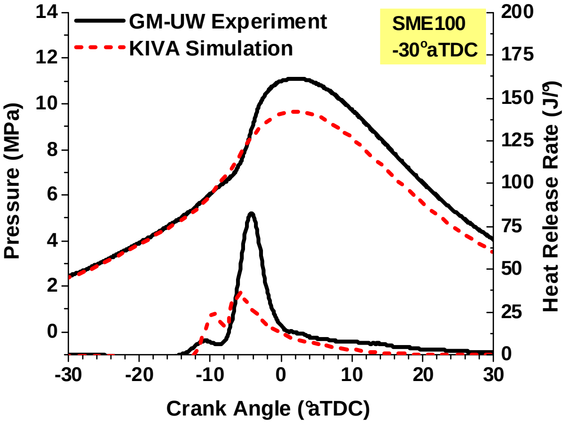

Figure 5-19: Preliminary pressure and heat release predictions for -30° aTDC SOI timing using SME100 fuel

First, sweeps of IVC temperatures and EGR percentages were performed with the goal of improving fuel reactivity. Figure 5-20(a) shows that the increased temperatures advanced ignition, but did not improve the combustion. Increased oxygen availability shown in Figure 5-20(b) improved the main combustion, but advanced ignition beyond what could be realistically-controlled by reducing IVC temperatures.

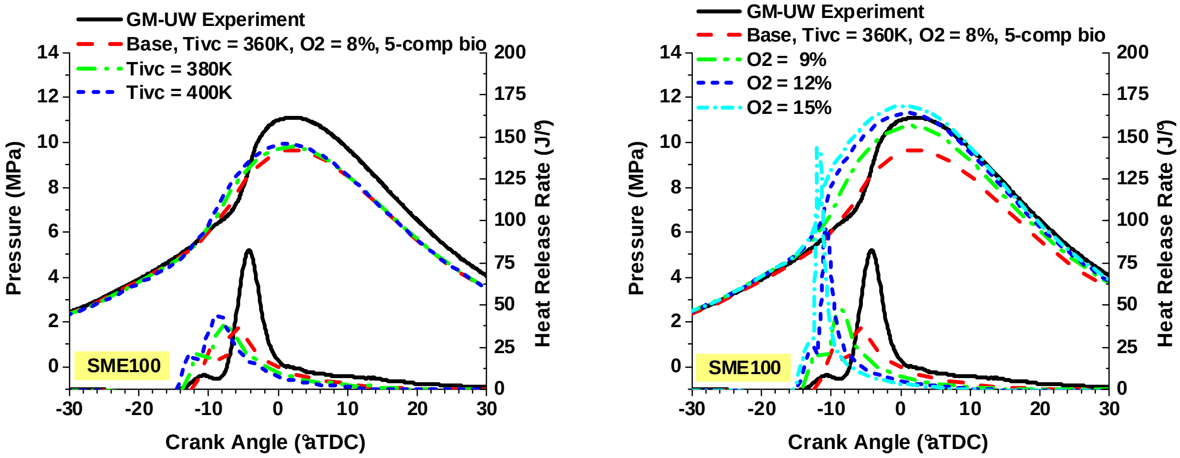

(a) (b)

Figure 5-20: Effect of increased (a) IVC temperature and (b) O_2 fraction in EGR for the -30° aTDC SOI timing using SME100 fuel

Finally, the properties were changed to tetradecane ($C_{14}H_{30}$), the physical property surrogate for diesel simulations, to assess whether a more-volatile set of fuel properties would improve the vaporization and fuel reactivity. As seen in Figure 5-21, the combustion was improved, but the excessive low-temperature chemistry persisted, confirming that chemistry required further investigation.

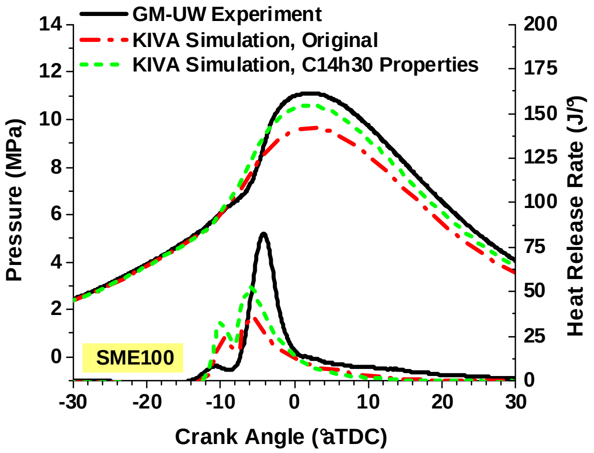

Figure 5-21: Small improvement in combustion performance when biodiesel properties (dash-dot) are replaced with tetradecane (dashed) for -30^{o} aTDC SOI timing using SME100 fuel

The following chapter outlines shortcomings that were identified in the current biodiesel kinetic mechanism. Improvements were made to the mechanism, including another reduction to create a truly skeletal model, and a new strategy for biodiesel chemistry is introduced to overcome the limitations that exist with the current method.

Chapter 6: Biodiesel Chemistry Improvements

6.1 Motivation for Chemistry Improvements

Since the initial LTC simulations performed well with a large proportion of n-heptane, the first step in investigating the biodiesel chemistry was to compare the ignition behavior of the methyl esters to that of n-heptane. Figure 6-1 provides the ignition delay times for MD and MD9D compared to the prediction of n-heptane using the ERC-MultiChem mechanism. The n-heptane ignites much sooner, particularly at the lower initial temperatures.

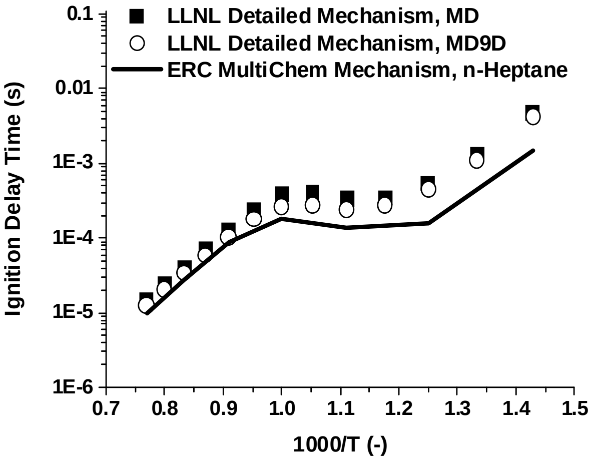

Figure 6-1: Constant volume ignition delay time predictions using the LLNL detailed mechanism for MD (squares) and MD9D (circles) and the ERC-MultiChem for n-heptane (line)

The premixed nature of the early injection LTC cases made it possible to perform an engine-specific chemistry investigation using Senkin single-zone HCCI simulations. This strategy served two purposes: quick run-times (less than 1 minute) and the homogeneity and absence of a spray isolated the chemistry from physical property effects. Comparisons were made to the -33^{o} aTDC SOI timing case using SME100 fuel at a uniformly-mixed equivalence ratio of 0.6. The initial pressure and temperature (both at IVC) were taken from the experimental conditions. The simulations were adiabatic, resulting in steep spikes in pressure compared to the experiment. The heat release rates for these single-zone simulations were *chemical* heat release and not calculated from the pressure trace, as was done in the experiment. As such, the single-zone results were intended solely as a qualitative comparison to the experiment.

As shown in Figure 6-2, the n-heptane mechanism performed relatively well compared to the experiment considering the adiabatic HCCI conditions of the simulation. The mechanism has distinct low-temperature and main heat releases. It should be noted that n-heptane is shown against a biodiesel experiment in Figure 6-2. It is intended for qualitative comparison only to demonstrate provide an example of the ignition behavior needed to represent LTC biodiesel combustion. Figure 6-3 displays the HCCI predictions when MD and MD9D are individually applied as biodiesel. Figure 6-3(a) shows that MD (dash) fuel in the reduced mechanism did not ignite and the early-stage combustion of MD9D (dash-dot) fuel released as much energy as the main combustion.

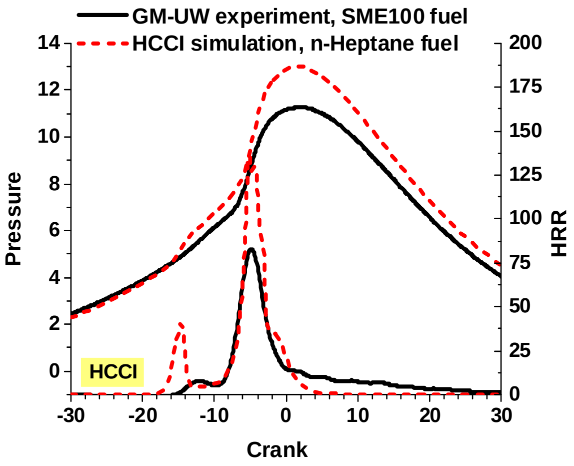

Figure 6-2: Comparison of LTC experiment for -33^o aTDC SOI timing case using SME100 fuel and predictions using n-heptane fuel chemistry in a single-zone HCCI engine simulation

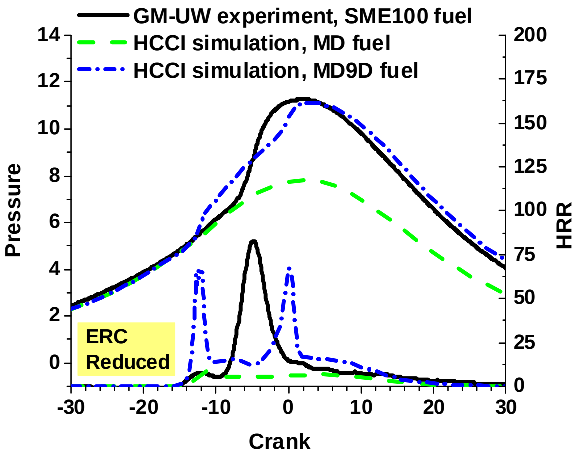

Figure 6-3: Comparison of LTC experiment for -33^{o} aTDC SOI timing and single-zone HCCI engine simulation predictions using MD and MD9D fuel chemistry from the reduced mechanism

Chemkin-Pro was used to visualize the important reactions that formed HO_2, OH, and CO for n-heptane. The third most important reaction in the list was *c2h5+o2=c2h4+ho2*. This reaction was #8 for the MD fuel and #22 on the list for MD9D. The n-heptane mechanism includes a species that directly forms C_2H_5 as one of the early decomposition steps through the reaction *c7h15-2=c2h5+c2h4+c3h6*. This is not an elementary reaction and was likely a result of combining multiple reactions during development of the n-heptane reaction mechanism. Regardless of the origin, this reaction is key to forming HO_2 under these LTC conditions. In contrast, the MD/MD9D mechanisms had to go through several other pathways before reaching that species. The mechanisms did include reactions for C_3H_5: *c6h12-1=c3h5+c3h7* for MD and *c6h10-15=c3h5+c3h5* for MD9D. The C_3H_5 species contributed to C_2H_5 and then HO_2, but enhancing the reaction by two orders of magnitude did not improve the results.

In order to attain appropriate combustion for LTC biodiesel simulations, advanced ignition delay times (more similar to n-heptane according to Figure 6-1 and Figure 6-2) were required. With this in mind, there were two options. Due to the reduced form of the mechanism, it would be justified to radically adjust the rate constants to make the MD/MD9D species more representative of their real biodiesel methyl esters. Unfortunately, at the time of this work, there were no biodiesel ignition delay experiments (e.g., shock tube or rapid compression machine) to validate those adjustments. The rate constants could be adjusted to match the LTC experiments, but the mechanism would then be restricted to that narrow range of operating conditions. In addition, there would be no way to isolate the chemistry from the experiments from the physical property effects.

Without another means of evaluating the ignition delay performance, the detailed mechanism was the only available baseline for validation. An initial concern was that important low temperature reactions were removed during the mechanism reduction process. The detailed mechanism was applied in the HCCI engine simulation to test that hypothesis. Figure 6-4 confirms that the ignition problems originated from the detailed LLNL mechanism.

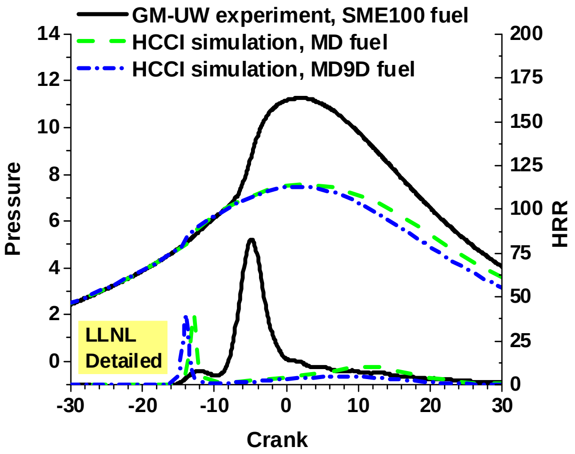

Figure 6-4: Comparison of LTC experiment for -33^{o} aTDC SOI timing and single-zone HCCI engine simulation predictions using MD and MD9D fuel chemistry from the detailed mechanism

Considering the poor performance of the detailed mechanism for the LTC simulations, the MD/MD9D species were deemed inappropriate as individual biodiesel surrogates, but that did not mean they were inappropriate as *components* of a surrogate biodiesel fuel. The second option involved adjusting the MD/MD9D rate constants as needed to match the detailed mechanism, then including another species, namely n-heptane, as one of the biodiesel chemistry components as a means of improving ignition performance. This latter option was chosen and is described in the following section.

6.2 New Strategy for Biodiesel Simulation Chemistry

The strategy of including n-heptane as a surrogate for biodiesel was first reported by Brakora et al. [91] when a mixture of the small-chain methyl ester methyl butanoate ($C_5H_{10}O_2$), termed "MB", was combined with two moles of n-heptane. The idea was to simulate the relatively quick decomposition of the $C_{17\text{-}19}$ methyl esters of real biodiesel in a single step as depicted in Figure 6-5. This method more accurately represented the C/H/O ratio found in real biodiesel methyl esters and the mechanism was able to reproduce conventional combustion ignition and performance, but was not able to capture NOx emissions trends.

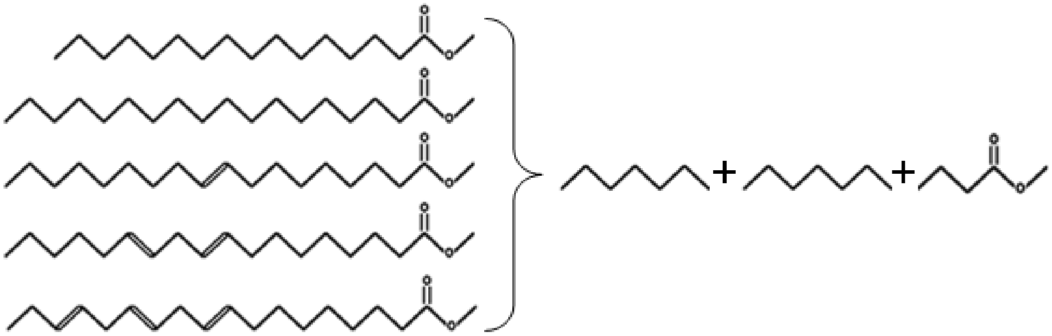

Figure 6-5: Previous biodiesel chemistry strategy using n-heptane and MB

As mentioned previously, the methyl decanoate and methyl-9-decenoate mechanisms soon replaced MB as the state-of-the-art biodiesel surrogates. While the initial intent of in this work was to use the MD/MD9D species alone, it should be noted that the researchers at LLNL who developed the detailed mechanisms included n-heptane in their validation work against real biodiesel fuels as well. In addition, researchers at the University of Connecticut and Argonne National Laboratory collaborated to create their own MD/MD9D reduced mechanism in parallel to this work. They validated their mechanism using a mixture of 25% MD, 25% MD9D and 50% n-heptane, but did not indicate an approach for accounting for various fuel compositions.

In contrast to the MB work, the long chain length of the MD and MD9D methyl esters allowed a single n-heptane to be applied for each methyl ester species, as shown in Figure 6-6. Using this strategy, B100 simulations now required six components, and 50% (mole fraction) would be represented by n-heptane. The remaining portion is divided among MD and MD9D depending on the biodiesel type that is being represented. For example, considering the compositions shown previously in Figure 4-11, RME would contain 2.5% MD and 47.5% MD9D, SME would have 8% MD and 42% MD9D, and PME would be 24.5% MD and 25.5% MD9D.

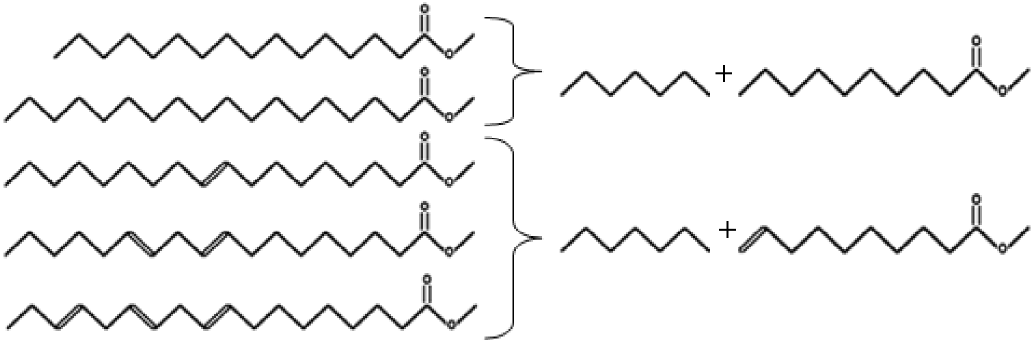

Figure 6-6: New biodiesel chemistry strategy using n-heptane, MD and MD9D

The new n-heptane strategy was intended to include n-heptane chemistry only, and not apply the volatile n-heptane physical properties. Consequently, a new dummy species (nc7bio) was included in the mechanism to link n-heptane chemistry with biodiesel physical properties. For a given fuel composition, the nc7bio species was given properties of the dominant biodiesel component.

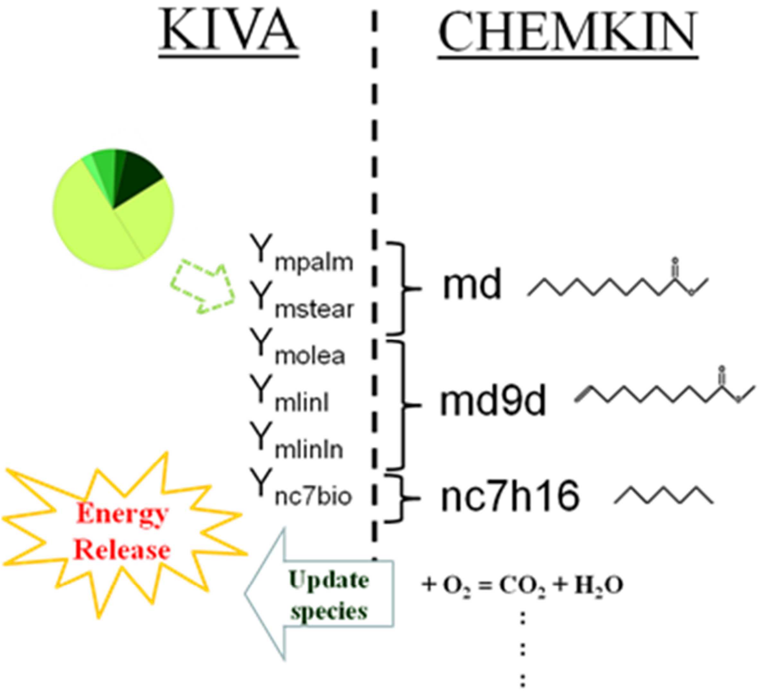

Figure 6-7: Pictorial description of connection between physical properties and chemistry in multi-component KIVA simulations using the new biodiesel strategy; compare to Figure 4-3.

6.3 Second Mechanism Reduction

While investigating the chemistry, it was found that the MD/MD9D portion of the mechanism had several dead-end pathways leaving long-chain species with no decomposition reactions. These persistent species decreased the efficiency of the mechanism by increasing the species count without contributing to the progression from fuel to products. A second manual reduction was performed to eliminate these surplus species and provide a straightforward skeletal set of reactions for future analysis.

As a first step, the biodiesel reactions were rearranged to easily discern reaction flow from fuel-decomposition to lower-level intermediate species. The existing nine oxidation pathways in the n-heptane portion of the mechanism served as a template from which the new biodiesel arrangement was modeled. Table 6-1 lists the n-heptane reactions and the analogous reactions in the reduced MD/MD9D mechanisms. MD/MD9D oxidation requires several more pathways, as displayed in Figure 3-6, and they remained in the mechanism as “additional reactions”. It should be noted that the n-heptane reactions do not include an isomerization reaction (e.g., md6o2=md6ooh8j). This reaction is embedded in Reaction 6. The two reactions in the MD/MD9D mechanisms could not be assimilated into a single reaction without a drastic effect on ignition delay time and were therefore assessed separately.

Table 6-1: Curran reaction class [30] for the nine n-heptane reactions and analogous MD/MD9D reactions in the ERC-MultiChem+MD/MD9D mechanism

Rxn #	**n-Heptane Reaction**	**MD/MD9D Analogous Reactions**	**Curran Rxn Class**
1	nc7h16+h=c7h15-2+h2	md+h=md6j+h2 md9d+h=md9d6j+h2 md9d+h=md9d8j+h2	2
2	nc7h16+oh=c7h15-2+h2o	md+oh=md6j+h2o md9d+oh=md9d6j+h2o md9d+oh=md9d8j+h2o	2
3	nc7h16+ho2=c7h15-2+h2o2	md+ho2=md6j+h2o2 md9d+ho2=md9d6j+h2o2 md9d+ho2=md9d8j+h2o2	2
4	nc7h16+o2=c7h15-2+ho2	md+o2=md6j+ho2 md9d+o2=md9d6j+ho2 md9d+o2=md9d8j+ho2	2
5	c7h15-2+o2=c7h15o2	md6j+o2=md6o2 md9d6j+o2=md9d6o2 md9d8j+o2=md9d8o2	10
6	c7h15o2+o2=c7ket12+oh	md6o2=md6ooh8j md9d6o2=md9d6ooh8j md9d8o2=md9d8ooh6j	12
		md6ooh8j+o2=mdket68+oh md9d6ooh8j+o2=md9dket68+oh md9d8ooh6j+o2=md9dket86+oh	22
7	c7ket12=c5h11co+ch2o+oh	mdket68=oh+c2h5cho+ms6oxo7j md9dket68=oh+c2h3cho+ms6oxo7j md9dket86<=>oh+mh6oxo+ch2co+c2h3	24
8	c5h11co=c2h4+c3h7+co	c2h5cho=c2h5+hco c2h3cho=c2h3+hco	NA
9	c7h15-2=c2h5+c2h4+c3h6	c6h12-1=c3h5+c3h7* c6h10-15=c3h5+c3h5	3

**Added later from detailed LLNL mechanism*

A single dominant pathway for each fuel was identified and the rest were removed. The largest species removal came from completely eliminating the *md9d8j* pathway from the MD9D branch shown in Figure 3-6. Three species were removed from the MD branch by combining reaction sets. The combined pathways are listed in Table A-3 of Appendix A. The resulting skeletal mechanism, ERC-MultiChem+Bio, consisted of 69 species and 192 reactions, including the six dummy biodiesel and four NOx species. The new mechanism's key pathways for each fuel are shown in Figure 6-8. The new ERC-MultiChem+Bio mechanism required additional rate parameter adjustments to reproduce the MD and MD9D ignition delay curves. The changes are documented in Table A-4 of the Appendix.

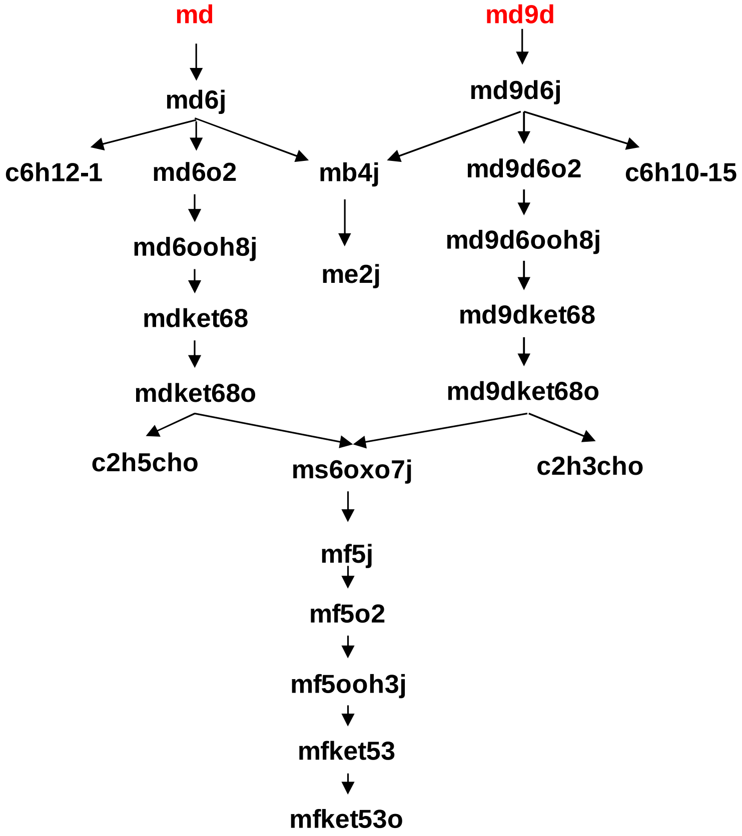

Figure 6-8: Key pathways remaining in the second reduction process to form a skeletal ERC-MultiChem+Bio mechanism

Figure 6-9 displays the resulting ignition delay predictions for the range of engine-relevant conditions mentioned previously in Table 3-3. Errors are shown in Table 6-2. Note that these values represent about a 12% increase compared to the previous mechanism, but ignition delay predictions for both fuels are more consistent across the sweep of equivalence ratios. Additionally, the new mechanism contains 12 fewer species, which reduces computation time for the simulations. While the errors are larger, the same uncertainty applies as mentioned previously. More accurate ignition validation can be achieved when reliable ignition delay data becomes available for biodiesel fuels or representative long-chain methyl esters.

Table 6-2: Maximum error observed for the ERC-MultiChem+Bio mechanism

Conditions at Maximum Ignition Delay Error	**Fuel**	
	MD	**MD9D**
Pressure (bar)	40	40
Equivalence Ratio	0.50	0.50
Temperature (K)	950	800
LLNL Ignition Delay (μs)	1430	2520
ERC Ignition Delay (μs)	810	819
Ignition Difference (μs)	620	1700
Error (%)	**43.3**	**67.5**
Difference (CA*)	3.7	10.2

**assuming 1000 rev/min*

The following chapter discusses the application of this new strategy to the LTC cases. It should be noted that the original engine validation cases using the conventional combustion in the SCORE were satisfactorily repeated, including NOx predictions, and those results are in Appendix A.

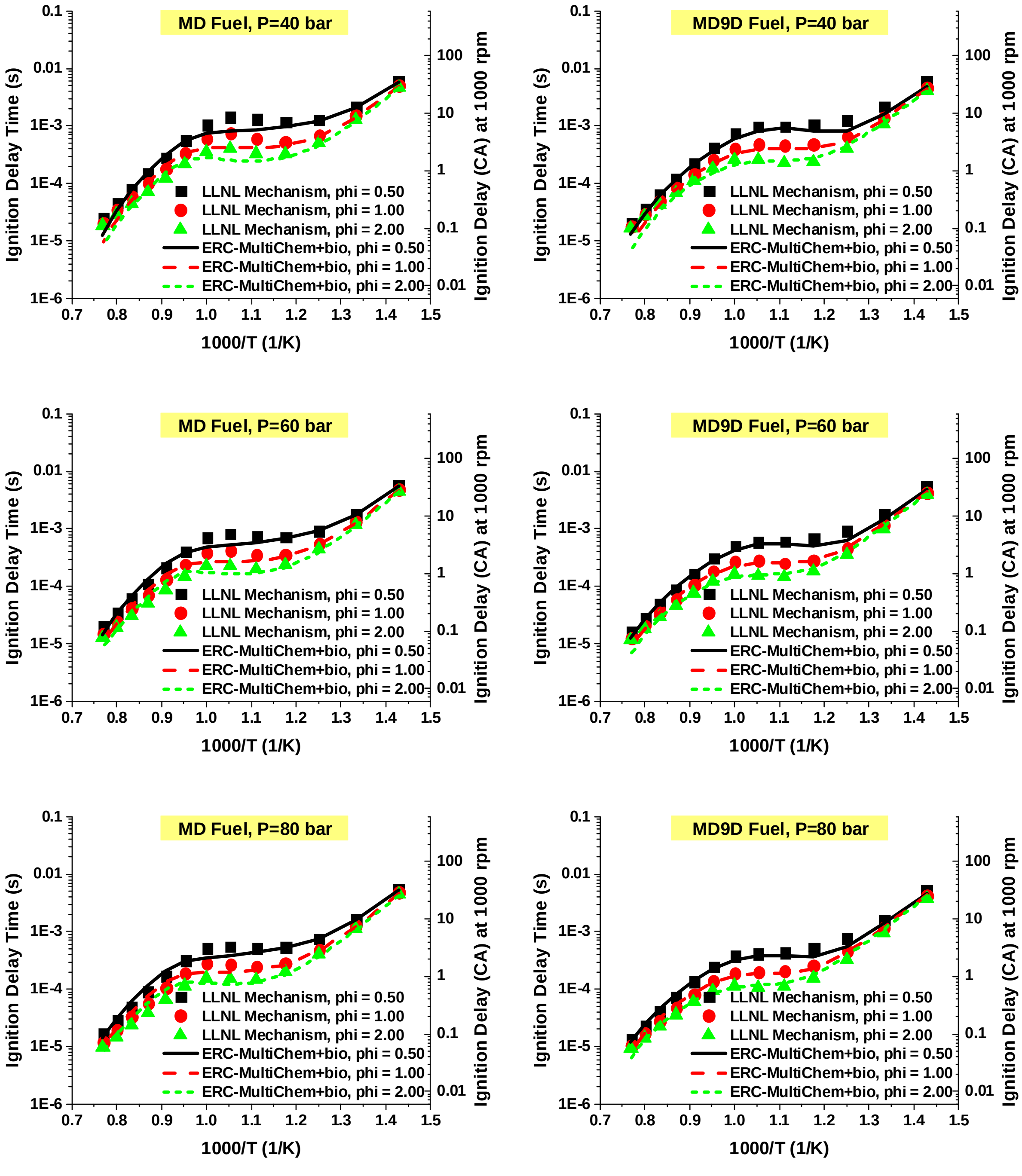

Figure 6-9: Ignition delay time predictions for the skeletal ERC-MultiChem+Bio mechanism

Chapter 7: Low Temperature Combustion Cases

7.1 SME100 LTC

The LTC simulations using neat soy-based biodiesel were repeated using the new chemistry strategy. First, it should be noted that runtimes for the SME cases improved from nearly 30 hours to 22 hours by eliminating the 14 species in the second mechanism reduction. This 27% reduction in CPU time can translate to significant walltime savings with parallel computing. The simulations were run on a computer cluster that consists of an array of Intel® Pentium™4 and Core™2 processors. Runtimes can be reduced to five hours using four processors in parallel.

Table 7-1 gives the new six-species fuel composition for the SME100 LTC cases, including the physical and chemical properties assigned to each species. The new biodiesel component was assigned methyl linoleate properties, since it was the dominant component for SME fuel.

Table 7-1: SME100 fuel composition for the new chemistry strategy

Mechanism Species	**Property Species**	**Chemistry Species**	**Composition (mass fraction)**
mpalm	m. palmitate	md	0.0590
mstear	m. stearate	md	0.0228
molea	m. oleate	md9d	0.1183
mlinl	m. linoleate	md9d	0.2572
mlinln	m. linolenate	md9d	0.0388
nc7bio	m. linoleate	nc7h16	0.5039

Table 7-2 lists the initial conditions used to reproduce the experiments. Similar to the diesel cases, the IVC temperature and EGR percent were adjusted as needed for each SOI timing. As seen in the table, the biodiesel simulations required higher temperatures to vaporize the less-volatile methyl esters. Despite the higher temperatures, the biodiesel still penetrated further compared to the diesel fuel. Figure C-1 compares in-cylinder fuel penetration predictions for the two fuels. The longer penetration of biodiesel is most noticeable at -13^{o} aTDC.

Table 7-2: Initial conditions for SME100 fuel LTC simulations

SOI Timing (^{o} aTDC)	**IVC Pressure (bar)**	**IVC Temperature (K)**	**EGR Percent (%)**
-36	1.918	375	70
-34	1.926	380	70
-32	1.933	380	70
-30	1.920	365	68
-28	1.922	375	69
-26	1.922	370	68
-24	1.918	370	68
-22	1.930	355	68

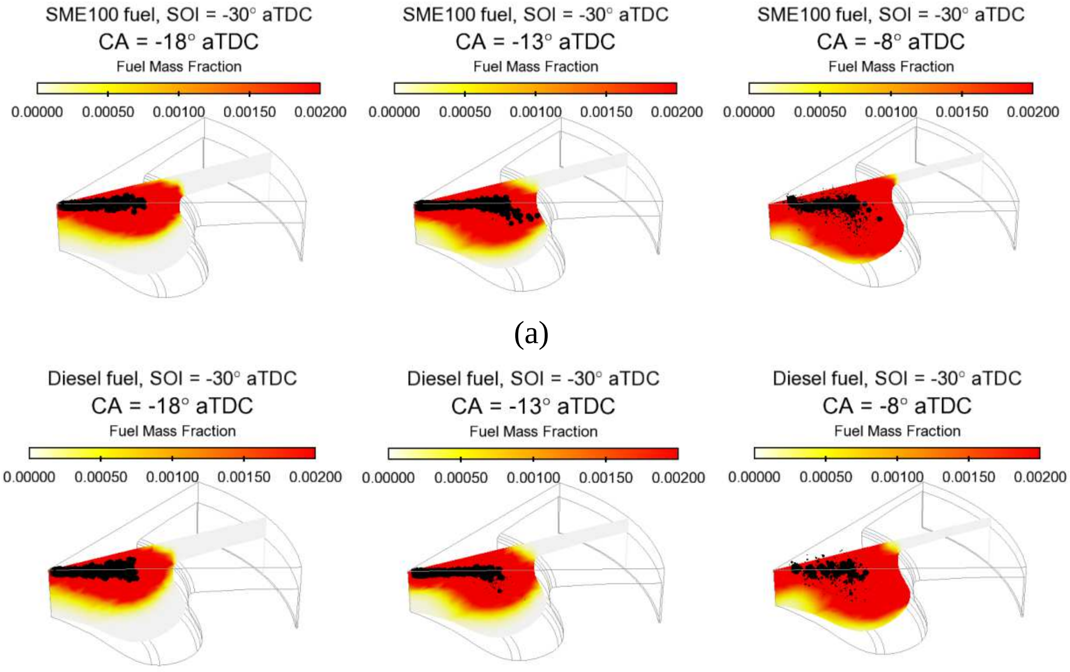

(a)

(b)

Figure 7-1: In-cylinder fuel penetration predictions for (a) SME100 and (b) diesel fuels at the -30^o aTDC SOI timing under LTC conditions.

The simulations were run using the standard KH-RT spray constants. It was of interest to test the spray constants identified in the unsteady SCORE spray cases run previously. Table 7-2 shows the excessive fuel penetration that occurs using these constants. This is expected, since the GM engine is much smaller than the SCORE. With a bowl radius of only 2.5 cm, a *distant* value of 4.5 never allows the RT spray model to be called in the GM engine. A spray constant analysis was not performed for this engine. Instead, the standard KH-RT values were applied.

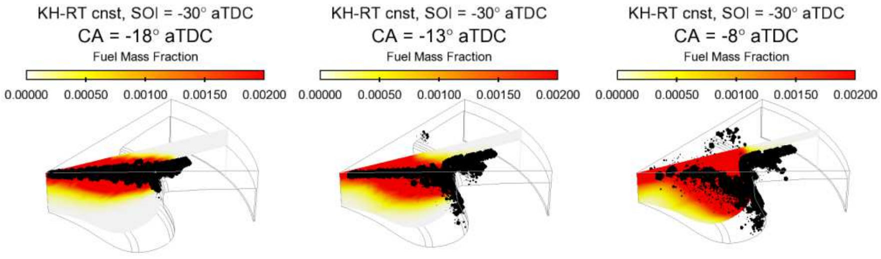

Figure 7-2: In-cylinder fuel penetration predictions for SME100 fuel -30^o aTDC SOI timing under LTC conditions using KH-RT constants identified in unsteady spray simulations

Figure 7-3 displays the results from the -32^o, -26^o and -22^o aTDC SOI timings and compares them to the diesel simulation results. The figure confirms that ignition timing, pressure, and heat release rate are well-matched for both fuels. Similar agreement is seen over the range of SOI timings and full results are shown in Appendix A.

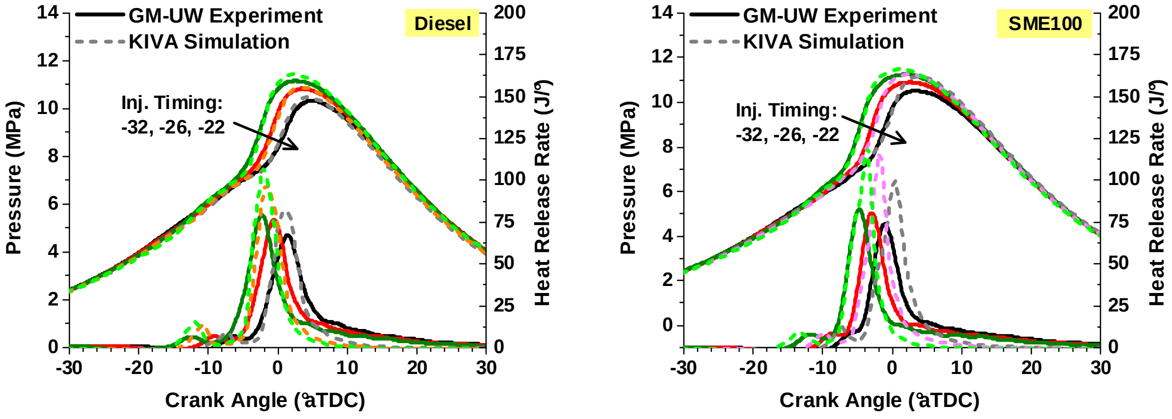

(a)

(b)

Figure 7-3: Comparison of pressure and heat release rate for (a) diesel and (b) neat soy biodiesel for LTC injection timings of -32^o, -26^o and -22^o aTDC

Figure 7-4 shows the simulated emissions and fuel consumption results for the two fuels compared to their respective experiments. The simulations do very well reproducing the experiments. Only a subtle CO “sweet spot” exists for these experimental conditions and the simulations are able to capture the lower emission values around -30° aTDC. Figure 7-5 provides a different perspective, comparing the two fuels as observed in the experiments and predicted by the simulations. The simulations match the experimental trend well. The HC predictions are similar for diesel and biodiesel, while NOx is lower and fuel consumption is higher for biodiesel compared to diesel.

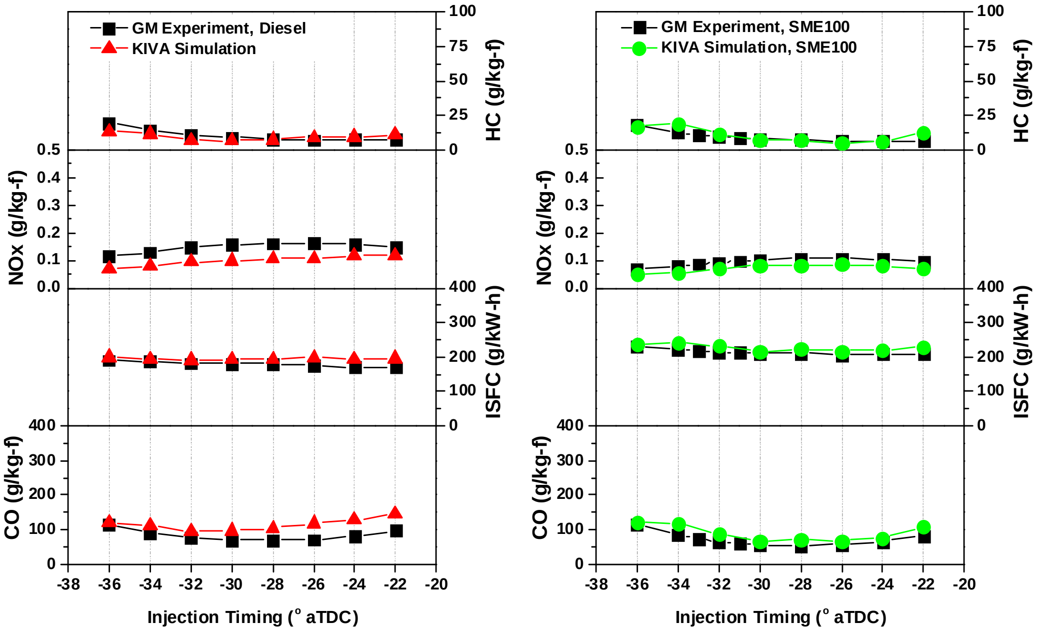

(a) (b)

Figure 7-4: Simulated emissions and fuel consumption predictions for (a) diesel and (b) SME100 compared to experimental results of Tran [88]

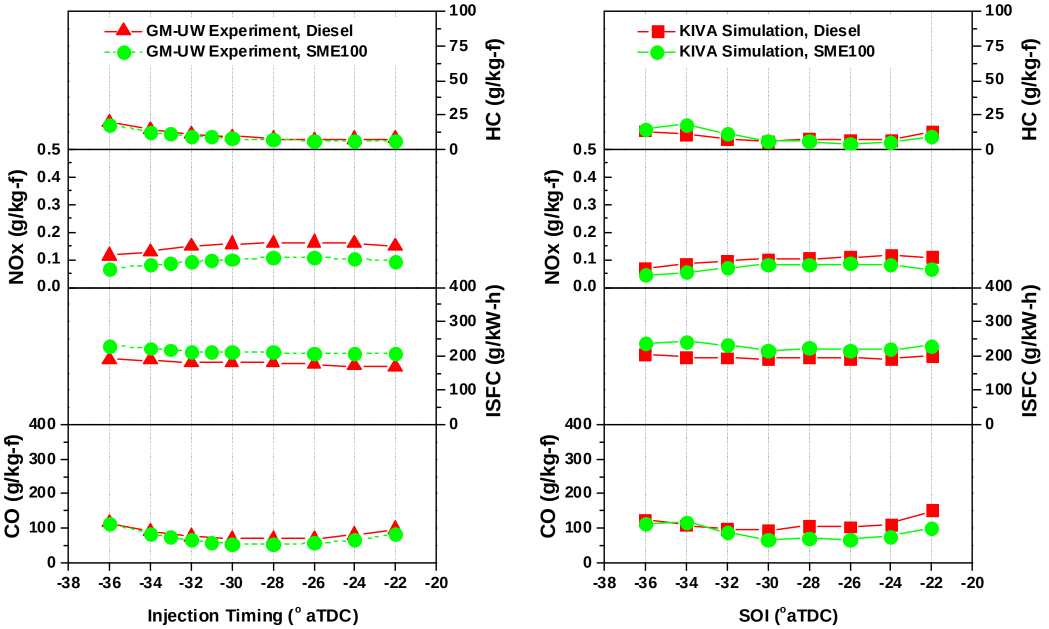

(a) (b)

Figure 7-5: Comparison of diesel and SME100 emissions and fuel consumption results (a) observed by the experiments of Tran [88] and (b) predicted by the KIVA simulations

7.2 B20 Results

Next, the new strategy was applied to the B20 cases. Table 7-3 and Table 7-4 provide the seven-species fuel compositions for the PME20 and SME20 LTC cases. The PME and SME compositions shown in Figure 4-11 were used for the methyl ester portion of the biodiesel fraction in each of these fuel blends.

Table 7-3: PME20 fuel composition for the new chemistry strategy

Mechanism Species	**Property Species**	**Chemistry Species**	**Composition (mass fraction)**
mpalm	m. palmitate	md	0.0483
mstear	m. stearate	md	0.0054
molea	m. oleate	md9d	0.0432
mlinl	m. linoleate	md9d	0.0121
mlinln	m. linolenate	md9d	0.0006
nc7bio	m. palmitate	nc7h16	0.1142
nc7h16	tetradecane	nc7h16	0.7763

Table 7-4: SME20 fuel composition for the new chemistry strategy

Mechanism Species	**Property Species**	**Chemistry Species**	**Composition (mass fraction)**
mpalm	m. palmitate	md	0.0132
mstear	m. stearate	md	0.0051
molea	m. oleate	md9d	0.0265
mlinl	m. linoleate	md9d	0.0577
mlinln	m. linolenate	md9d	0.0087
nc7bio	m. linoleate	nc7h16	0.1130
nc7h16	tetradecane	nc7h16	0.7757

Each blend case required unique initial conditions for the simulations. EGR was kept within the range the values given in the experiments and the calculated external EGR plus residual mass. Table 7-5 and Table 7-6 list the initial condition applied for the PME20 and SME20 cases, respectively.

Table 7-5: Injection information for PME20 fuel

SOI Timing (^{o} aTDC)	**IVC Pressure (bar)**	**IVC Temperature (K)**	**EGR Percent (%)**
-36	1.905	370	73
-34	1.922	360	70
-32	1.917	360	69
-30	1.922	370	69
-28	1.915	360	69
-26	1.909	360	70
-24	1.903	360	70
-22	1.920	360	70

Table 7-6: Injection information for SME20 fuel

SOI Timing (^{o} aTDC)	**IVC Pressure (bar)**	**IVC Temperature (K)**	**EGR Percent %**
-36	1.914	365	73
-34	1.917	360	71
-32	1.919	360	70
-30	1.922	360	70
-28	1.915	360	70
-26	1.906	360	71
-24	1.911	360	71
-22	1.913	355	71

Figure 7-6 shows results for the two fuel blends for the -32^o, -26^o and -22^o aTDC SOI timings. The results are fairly well-matched. Extensive optimization was not performed on the input conditions for these cases. It is expected improvements could be with input adjustments.

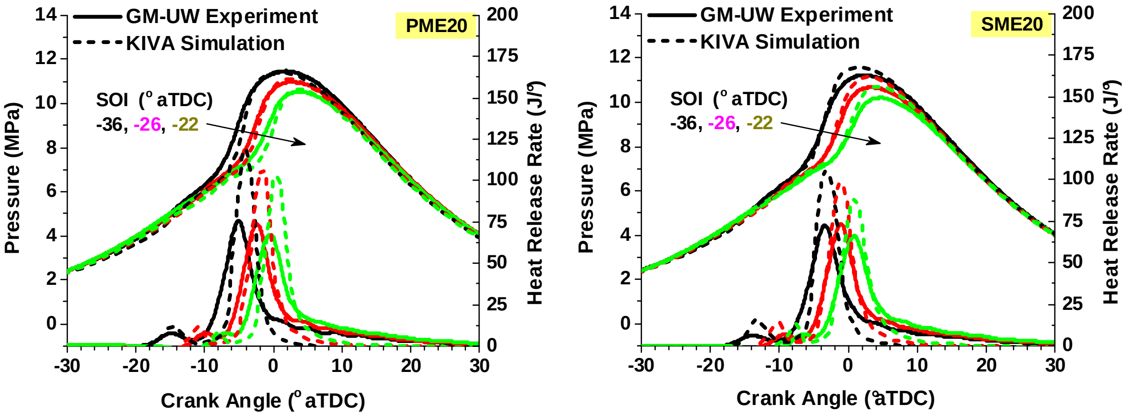

(a) (b)

Figure 7-6: Comparison of pressure and heat release rate for (a) PME20 and (b) SME20 biodiesel blends for LTC injection timings of -32°, -26° and -22° aTDC

Emissions and fuel consumption predictions for the two biodiesel blends are shown in Figure 7-7. Similar to the diesel case, the simulations under-predict NOx and over-predict CO, but the trends are consistent. Figure 7-8 confirms that the simulations do a good job reproducing the relative fuel differences seen in the experiments. The emissions and fuel consumption are similar for the three fuels, with the exception of NOx. The experiments attributed this increased NOx for PME20 to the higher cetane number of PME. The earlier ignition and longer residence time at higher temperatures promoted NOx formation. In the simulations, the PME20 ignited slightly sooner as well, but due to initial conditions and not fuel chemistry. The increased fraction of MD chemistry in the PME fuel actually reduces reactivity, as shown previously in the ignition delay comparison of Figure 6-1.

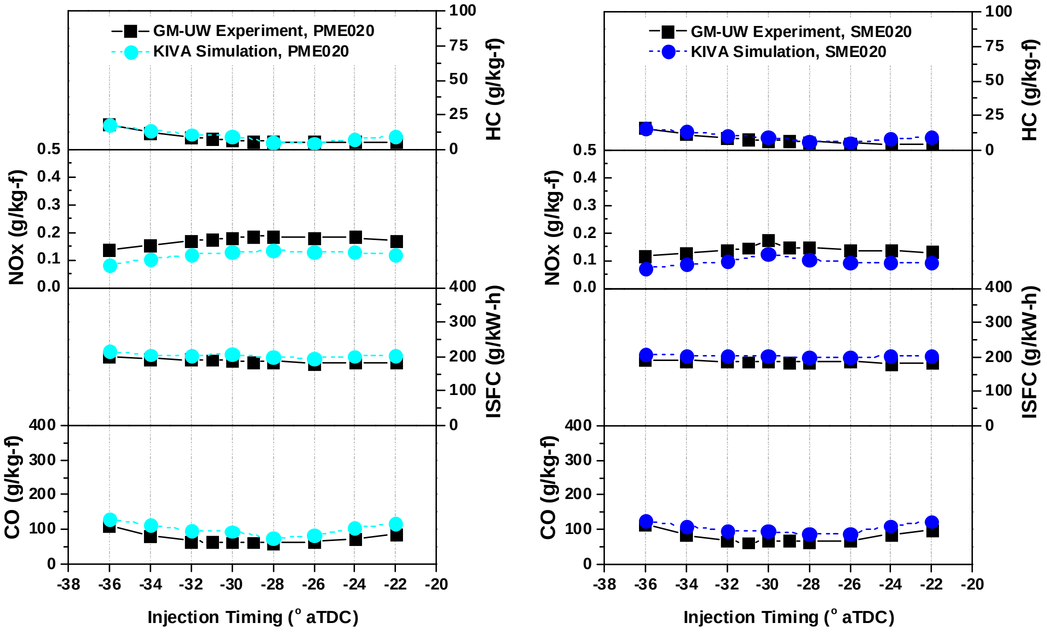

Figure 7-7: Simulated emissions and fuel consumption predictions for (a) PME20 and (b) SME20 biodiesel blends compared to experimental results of Tran [88]

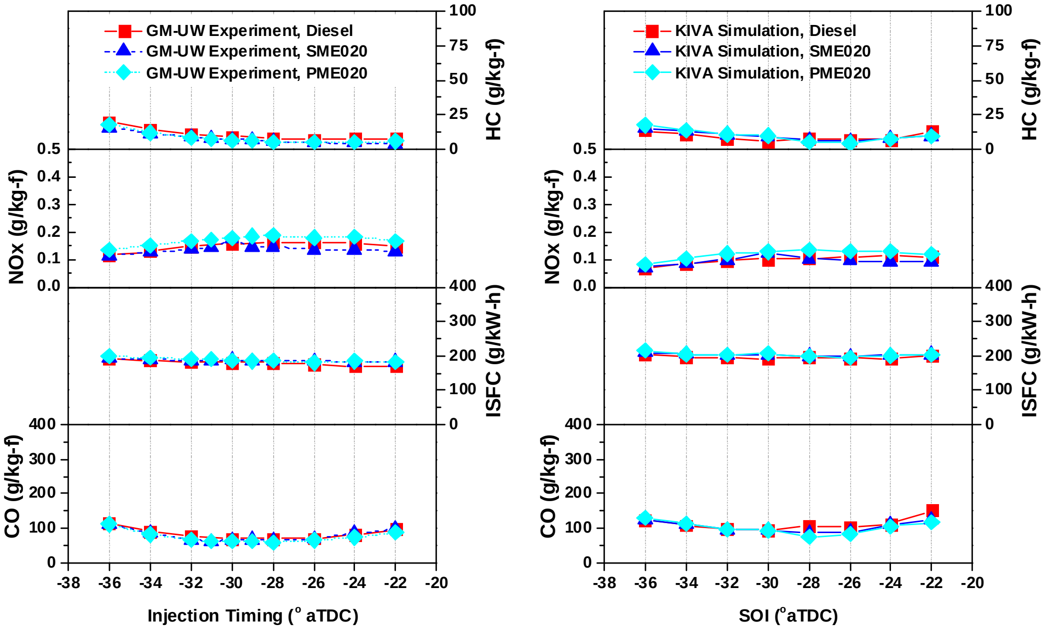

Figure 7-8: Comparison of diesel and the B20 blends' emissions and fuel consumption results (a) observed by the experiments of Tran [88] and (b) predicted by the KIVA simulations

Finally, a comparison was made between the diesel, SME20, and SME100 fuels to assess the impact of increased biodiesel fraction. Figure 7-9 compares diesel, SME20 and SME100 to show the impact of increased biodiesel. The simulations do well to capture the trends in the experiments. The B20 blend does not impact the results greatly. Neat biodiesel, however, slightly decreases NOx and increases ISFC. CO and HC are not significantly changed with increased biodiesel.

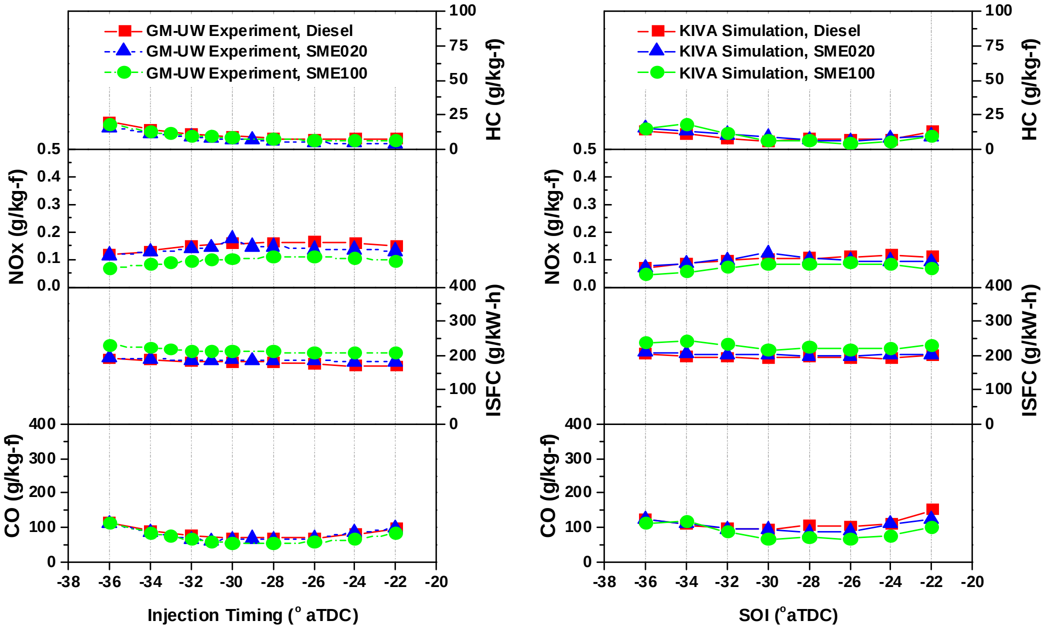

Figure 7-9: Impact of increased biodiesel fuel in (a) experiments and (b) simulations

7.3 Generic LTC Cases

It is difficult to definitively compare the effect of fuel type using the experimental cases shown previously, because the conditions such as EGR percent and initial temperatures and pressures differed for each SOI timing. Simulations offer the capability of performing an idealized comparison using identical conditions. A set of generic conditions was prepared for the -30^o aTDC case so that the EGR composition, IVC pressure and temperature, and fuel energy was the same for each fuel. Five fuels were compared: diesel, SME20, SME100, PME20 and PME100. The diesel fuel served as the baseline and the biodiesel blends had unique fuel masses, based on their densities and lower heating values, to match the energy content of the diesel fuel. Each fuel mass required a unique injection profile, which was calculated as done previously. Table 7-7 outlines the initial conditions and Table 7-8 lists the species composition used to represent the 70% EGR in-cylinder. All other inputs for the simulations were the same for each fuel.

Table 7-7: Initial conditions for generic LTC fuel comparison

Fuel	**Fuel Mass (mg)**	**IVC Pressure (bar)**	**IVC Temperature (K)**	**EGR Percent (%)**
Diesel	14.10	1.9	365	70
PME20	14.70			
PME100	17.35			
SME20	14.64			
SME100	17.30			

Table 7-8: Generic in-cylinder composition simulating 70% EGR for LTC fuel comparison

Fuel	**EGR Component Mole Fractions**
CH_4	0.0005
CO	0.0030
CO_2	0.0720
O_2	0.0840
H_2	0.0005
H_2O	0.0700
N_2	0.7700

First, a pressure and heat release rate comparison was made to ensure that the fuels maintained similar ignition and load. Figure 7-10 shows that the differences in combustion performance are nearly indistinguishable between fuels.

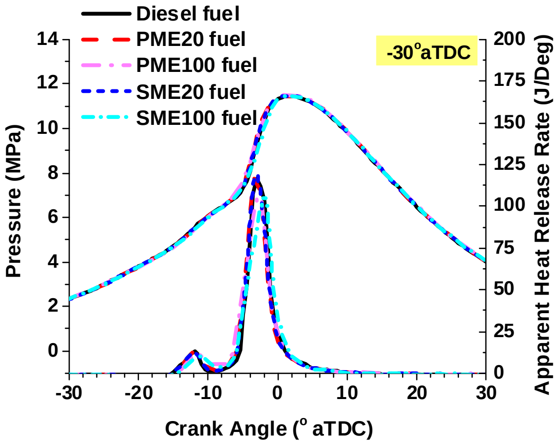

Figure 7-10: Pressure and heat release rate comparison for five fuels under LTC conditions at a -30^{o} aTDC SOI timing

Figure 7-11 compares the emissions and fuel consumption predicted by each of the fuels. CO was not affected by fuel type and both B20 blends are similar to the diesel case for all parameters. The B100 fuels, however, have higher HC and ISFC and lower NOx. The fuel consumption difference is a result of the increased biodiesel fuel mass required to match the diesel fuel energy. The HC emissions are due, at least in part, to the liquid biodiesel fuel remaining in-cylinder during the expansion stroke, as seen in Figure 7-12. Both fuels appear to have parcels caught on the piston head, exacerbating their vaporization. The least volatile fuel, SME100, has the most parcels remaining, and also the highest HC emissions at EVO.

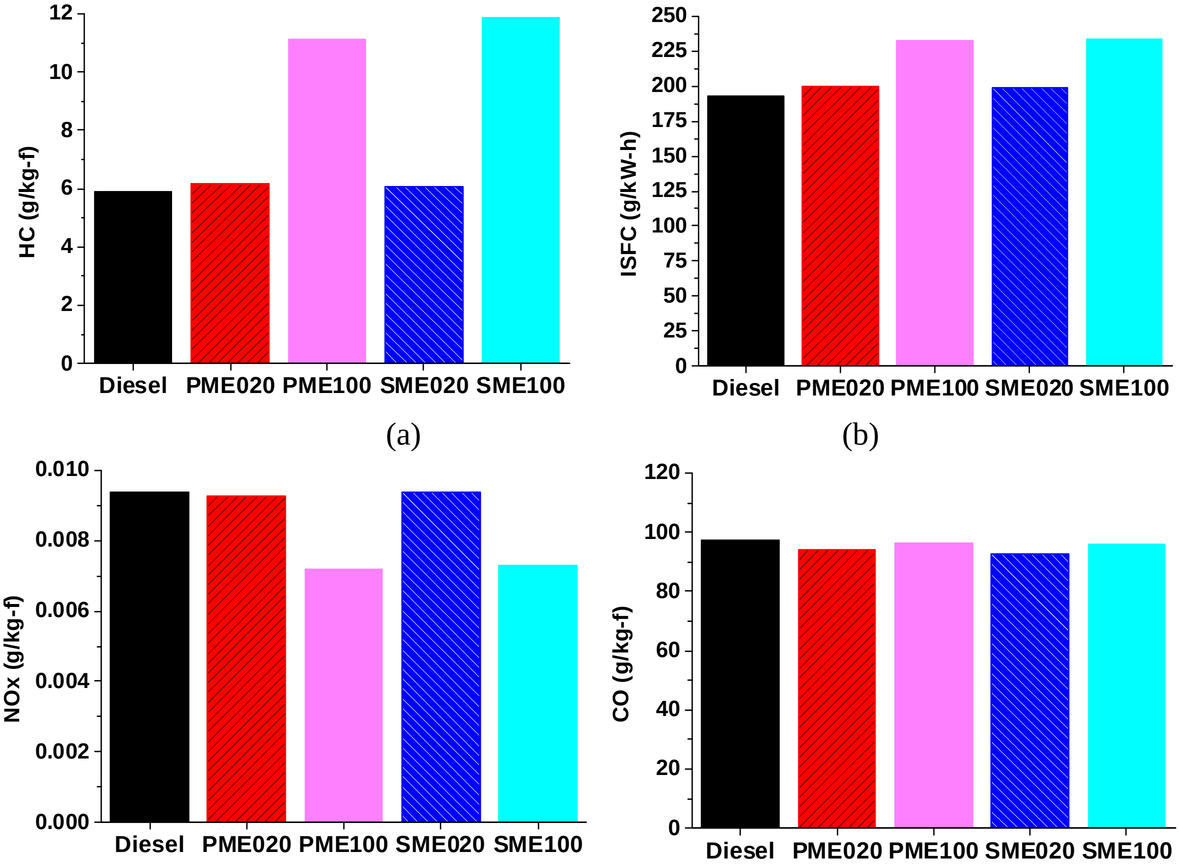

(a) (b)

(c) (d)

Figure 7-11: Comparison of (a) HC, (b) ISFC, (c) NOx, and (d) CO for five fuels under LTC conditions at a -30^o aTDC SOI timing

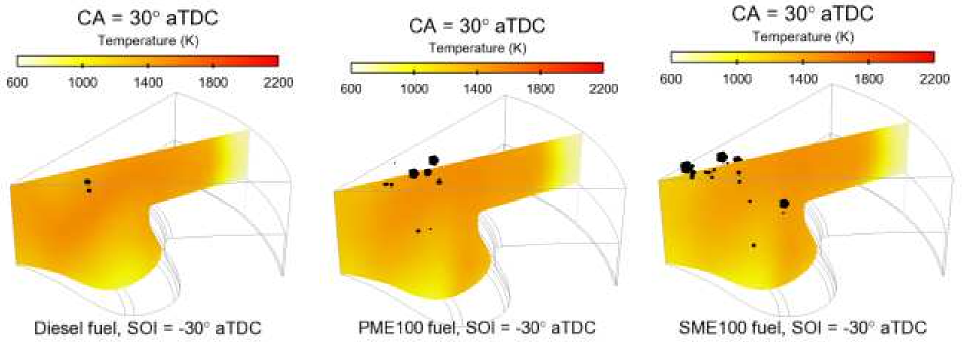

(a) (b) (c)

Figure 7-12: Unvaporized fuel remaining in-cylinder for (a) diesel, (b) PME100, and (c) SME100 fuels under LTC conditions at a -30^o aTDC SOI timing

For all fuels, the NOx predictions using the generic EGR composition were an order of magnitude smaller than the LTC experiments observed, suggesting that the temperatures in the simulations may be lower than those of the experiments. While a reduction in NOx was seen with B100 (as was observed in the LTC experiments), it is difficult to compare NOx formation in these simulations when so little was formed. The small difference may be due to the fact that the max temperature reached by the B100 fuels was about 5K cooler than the diesel.

Chapter 8: Conclusions and Future Work

8.1 Summary

In this work, a comprehensive biodiesel combustion model was created for use in multi-dimensional engine simulations. The model incorporates realistic physical properties in a vaporization model developed for multi-component fuel sprays and applies an improved mechanism for biodiesel combustion chemistry. In addition to developing a successful biodiesel combustion model, this work provided guidelines for future researchers who wish to reduce other detailed mechanisms for CFD applications.

A Lawrence Livermore National Laboratory mechanism for two biodiesel fuel surrogate species, methyl decanoate (MD) and methyl-9-decenoate (MD9D), was reduced from 3299 species to 85 species using a combination of the Directed Relation Graph method, isomer lumping, and limited reaction rate adjustments. The mechanism was later reduced further to 69 species and a new biodiesel chemistry strategy was implemented that included n-heptane to improve low-temperature combustion behavior. The MD/MD9D portions of the reduced mechanism accurately predicted ignition delay times of the detailed mechanism over a range of engine-specific operating conditions.

The fuel chemistry was combined with physical property information for the five methyl ester components of biodiesel to validate the model under realistic engine operating conditions. In both conventional and low temperature combustion strategies, the model was able to capture ignition, as well as key performance and emissions results. In addition, emissions and fuel consumption trends observed in the LTC experiments that compared diesel to the neat and blended biodiesel fuels in were reproduced with simulated fuels.

The results shown in this work suggest that this biodiesel model can be applied in conventional and low temperature combustion strategies using neat and blended biodiesel fuels from a variety of feedstocks. Very few deviations from the given experimental output (e.g., accounting for residual mass in LTC EGR calculations) were needed to obtain a good match to emissions and fuel consumption results. Future well-defined biodiesel experiments with clear operating conditions can easily be reproduced using this model. More importantly, the simulation predictions using a generic set of initial conditions were able to reproduce trends observed in the experiments, particularly the decreased NOx with neat biodiesel, without the exact experimental conditions, which ensures this model can also be used as a tool to *guide* future engine experiments.

8.2 Future Work

8.2.1 Improved Biodiesel Chemistry and Physical Properties

Ideally an equal number of chemistry and physical property surrogates would be used to model a given fuel. For diesel, it is impractical to model the hundreds of components of the real fuel. In contrast, biodiesel is mainly five components and each of those could realistically be represented. Researchers at Lawrence Livermore National Laboratory have developed a mechanism for the *real* five components of biodiesel: methyl palmate, methyl stearate, methyl oleate, methyl linoleate, and methyl linolenate [92,93]. The ignition delay predictions of these fuels are shown in Figure 8-1. It would be of interest to apply the reduction techniques described in this work to this very large (4800 species, 20000 reactions) mechanism and eliminate the need for simplified chemistry surrogates.

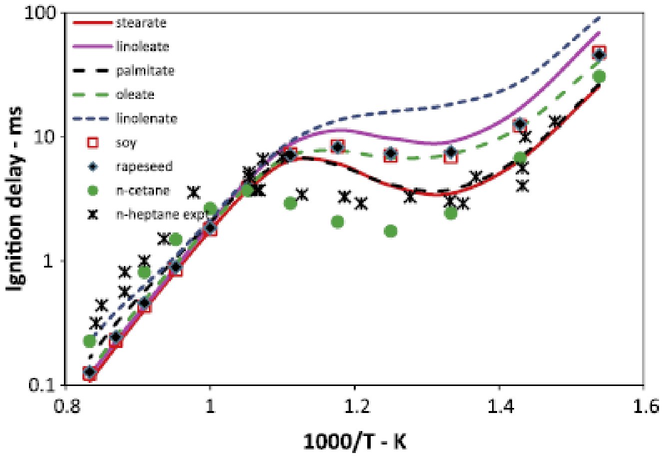

Figure 8-1: Ignition delay time predictions of detailed mechanisms for the real five components of biodiesel fuel; reproduced from [92,93]

In addition to the chemistry, it would be valuable for improvements to also be made to the methyl linoleate and methyl linolenate physical properties. At present, these components are mostly represented using a combination of predictions of the BDprop program from the University of Illinois at Urbana/Champagne [49,52] and methyl oleate properties. Hopefully researchers will soon have a means of characterizing these fuel components.

8.2.2 Application in Other Combustion Strategies

Hansen [94] recently performed Reactivity-Controlled Compression-Ignition (RCCI) experiments using a B20 blend in place of diesel as the high cetane fuel. The experiments were performed at Oak Ridge National Laboratory in a GM 1.9-L engine similar to the one used in the LTC experiments presented in this work. The stock piston was replaced with an RCCI-optimized piston, which offered a very low surface area to reduce heat transfer. Results from this work can provide another validation point for the biodiesel mechanism. From there, the model can be used to supplement future biofuel (B100 and ethanol) RCCI experiments that are planned.

8.2.3 Particulate Matter (Soot) Characterization

To date, particulate matter (PM) has received very little attention from the biodiesel modeling community. Yet the reduced PM seen with biodiesel is one of its key benefits. It is thought that the reduced PM of biodiesel causes a reduction in radiative heat transfer, which could lead to increased temperatures and thus increased NOx [84,95]. As mentioned previously, an improved soot model was developed by Vishwanathan [96,97] that includes a reduced mechanism for polycyclic aromatic hydrocarbon (PAH) formation, which is thought to impact soot formation. In addition, soot number density was included in the improved model. The improved soot model was not implemented into the biodiesel model in this work, but would be a valuable addition for future biodiesel analyses that include PM. The LTC experiments of Tran [88] included soot particle size and particle number data, which can be used to validate the model for diesel, B100 and the B20 blends.

References

1. Amsden, A. A., O'Rourke, P. J. and Butler, T. D. *KIVA-II: A Computer Program for Chemically Reactive Flows with Sprays,* Report No. LA-11560-MS, Los Alamos National Laboratories, May 1989.

2. Amsden, A. A. *KIVA-3V, Release 2: Improvements to KIVA-3V,* Report No. LA-UR-99-915, Los Alamos National Laboratories, October 1996.

3. Office of Transportation and Air Quality, U.S. E.P.A. "Overview: Pollutants and Programs" Available at: www.epa.gov/otaq/transport.htm

4. Office of Transportation and Air Quality, U.S. E.P.A. "Emission Standards Reference Guide" Available at: http://www.epa.gov/otaq/standards/index.htm

5. Dieselnet. "Emission Standards" Available at: www.dieselnet.com/standards/

6. Office of Transportation and Air Quality, U.S. E.P.A. "Transportation and Climate: Regulations and Standards" Available at: http://www.epa.gov/otaq/climate/regulations.htm

7. "Light-Duty Vehicle Greenhouse Gas Emission Standards and Corporate Average Fuel Economy Standards; Final Rule," 75 *Federal Register* 88 (May 7, 2011): 25324-25728. Available at: http://www.gpo.gov/fdsys/pkg/FR-2010-05-07/pdf/2010-8159.pdf.

8. "Greenhouse Gas Emissions Standards and Fuel Efficiency Standards for Medium- and Heavy-Duty Engines and Vehicles; Final Rule," 76 *Federal Register* 176 (September 15, 2011): 57106-57513. Available at: http://www.gpo.gov/fdsys/pkg/FR-2011-09-15/pdf/2011-20740.pdf.

9. National Highway Traffic and Safety Administration. "CAFE - Fuel Economy" Available at: http://www.nhtsa.gov/fuel-economy

10. Kamimoto, T. and Bae, M."High Combustion Temperature for the Reduction of Particulate in Diesel Engines" *SAE,* 880423 (1988)

11. Akihama, K., Takatori, Y., Inagaki, K., Sasaki, S. and Dean, A. M."Mechanism of the Smokeless Rich Diesel Combustion by Reducing Temperature" *SAE,* 2001-01-0655 (2001)

12. Kimura, S., Ogawa, H., Matsui, Y. and Enomoto, Y."An Experimental Analysis of Low Temperature and Premixed Combustion for Simultaneous Reduction of NOx and Particulate Emissions in Direct-Injection Diesel Engines" *Int. J. Engine Res.*, 3, 4 (2002) 249-259

13. Dec, J. E."A Conceptual Model of DI Diesel Combustion Based on Laser-Sheet Imaging" *SAE*, 970873 (1997)

14. Musculus, M. P. B."On the Correlation between NOx Emissions and the Diesel Premixed Burn" *SAE*, 2004-01-1401 (2004)

15. Pickett, L. M., Siebers, D. L. and Idicheria, C. A."Relationship between Ignition Processes and the Lift-Off Length of Diesel Fuel Jets" *SAE*, 2005-01-3843 (2005)

16. Siebers, D. L."Liquid Phase Fuel Penetration in Diesel Sprays" *SAE*, 980809 (1998)

17. Siebers, D. L."Scaling Liquid-Phase Fuel Penetration in Diesel Sprays Based on Mixing-Limited Vaporization" *SAE*, 1999-01-0528 (1999)

18. Genzale, C. L., Reitz, R. D. and Musculus, M. P. B. "Effects of Spray Targeting on Mixture Development and Emissions Formation in Late-Injection Low-Temperature Heavy-Duty Diesel Combustion" *32nd International Symposium on Combustion*, August 3-8, 2008.

19. Opat, R., Ra, Y., Gonzalez, M. A., Krieger, R., Reitz, R. D., Foster, D. E., Durrett, R. P. and Siewert, R. M."Investigation of Mixing and Temperature Effects on HC/CO for Highly Dilute Low Temperature in a Light-Duty Diesel Engine" *SAE*, 2007-01-0193 (2007)

20. Koci, C. P., Ra, Y., Krieger, R., Andrie, M., Foster, D. E., Siewert, R. M. and Durrett, R. P."Multiple-Event Fuel Injection Investigations in a Highly-Dilute Diesel Low Temperature Combustion Regime" *SAE*, 2009-01-0925 (2009)

21. Park, S. W. and Reitz, R. D."Modeling the Effect of Injector Nozzle-Hole Layout on Diesel Engine Fuel Consumption and Emissions" *J. Eng. Gas Turbines Power*, 130, (2008)

22. Park, S. W., Suh, H. K., Reitz, R. D., Abani, N. and Lee, C. S."Modeling of Group-Hole-Nozzle Sprays using Grid-Size-Hole-Location and Time-Step-Independent Models" *Atomization Sprays*, 19, 6 (2009) 567-582

23. Sun, Y. *Diesel Combustion Optimization and Emissions Reduction using Adaptive Injection Strategies (AIS) with Improved Numerical Models*, Ph.D. Thesis, University of Wisconsin, Madison, WI, 2007.

24. Genzale, C. L. *Optimizing Combustion Chamber Design for Low-Temperature Diesel Combustion*, Ph.D. Thesis, University of Wisconsin, Madison, WI, 2008.

25. Genzale, C. L., Reitz, R. D. and Musculus, M. P. B."Effects of Piston Bowl Geometry on Mixture Development and Late-Injection Low-Temperature Combustion in a Heavy-Duty Diesel Engine" *SAE*, 2008-01-1330 (2008)

26. Kokjohn, S. L., Hansen, R. M., Splitter, D. A. and Reitz, R. D."Experiments and Modeling of Dual-Fuel HCCI and PCCI Combustion using in-Cylinder Fuel Blending" *SAE,* 2009-01-2647 (2009)

27. Kokjohn, S. L., Hansen, R. M., Splitter, D. A. and Reitz, R. D."Fuel Reactivity-Controlled Compression-Ignition (RCCI) in Light- and Heavy-Duty Engines" *SAE Int. J. Engines,* 4, 1 (2011) 360-374

28. Kee, R. J., Rupley, F. M. and Miller, J. A. *CHEMKIN-II: A FORTRAN Chemical Kinetics Package for the Analysis of Gas Phase Chemical Kinetics,* Report No. SAND 89-8009, Sandia National Laboratories,

29. Lutz, A. E., Kee, R. J. and Miller, J. A. *SENKIN: A FORTRAN Program for Predicting Homogeneous Gas Phase Chemical Kinetics with Sensitivity Analysis,* Report No. SAND 89-8009, UC-4, Sandia National Laboratories,

30. Curran, H. J., Gaffuri, P., Pitz, W. J. and Westbrook, C. K."A Comprehensive Modeling Study of n-Heptane Oxidation" *Combust. Flame,* 114, (1998) 149-177

31. Kong, S., Marriott, C. D., Reitz, R. D. and Christensen, M."Modeling and Experiments of HCCI Engine Combustion using Detailed Chemical Kinetics with Multidimensional CFD" *SAE,* 2001-01-1026 (2001)

32. Patel, A., Kong, S. and Reitz, R. D."Development and Validation of a Reduced Reaction Mechanism for HCCI Engine Simulations" *SAE,* 2004-01-0558 (2004)

33. Singh, S., Reitz, R. D. and Musculus, M. P. B."Comparison of the Characteristic Time (CTC), Representative Interactive Flamelet (RIF), and Direct Integration with Detailed Chemistry Combustion Models Against Optical Diagnostic Data for Multi-Mode Combustion in a Heavy-Duty DI Diesel Engine" *SAE,* 2006-01-0055 (2006)

34. Singh, S., Musculus, M. P. B. and Reitz, R. D."Mixing and Flame Structures Inferred from OH-PLIF for Conventional and Low-Temperature Diesel Combustion" *Combust. Flame,* 156, 10 (2009) 1898-1908

35. Kokjohn, S. and Reitz, R. D."Investigation of the Roles of Flame Propagation, Turbulent Mixing and Volumetric Heat Release in Conventional and Low-Temperature Diesel Combustion" *J. Eng. Gas Turbines Power,* (2011)

36. Sarre, C. V., Kong, S. C. and Reitz, R. D."Modeling the Effects of Injector Nozzle Geometry on Diesel Sprays" *SAE,* 1999-01-0912 (1999)

37. Abani, N., Munnannur, A. and Reitz, R. D."Reduction of Numerical Parameter Dependencies in Diesel Spray Models" *J. Eng. Gas Turbines Power,* 130, (2008)

38. Beale, J. C. and Reitz, R. D."Modeling Spray Atomization with the Kelvin-Helmholtz/Rayleigh-Taylor Hybrid Model" *Atomization Sprays*, 9, (1999) 623-650

39. Ra, Y. and Reitz, R. D."A Vaporization Model for Discrete Multi-Component Fuel Sprays" *Int. J. Multiphase Flow,* 35, (2009) 101-117

40. Ra, Y. and Reitz, R. D."A Combustion Model for IC Engine Combustion Simulations with Multi-Component Fuels" *Combust. Flame,* 158, (2011) 69-90

41. Design Institute for Physical Property Data/AIChE. DIPPR Project 801 - Full Version. Knovel Corporation, (2010) Available: http://search.library.wisc.edu/catalog/ocm62295705

42. Gas Research Institute. "GRI-Mech, v3.0" Available: www.me.berkeley.edu/gri-mech/

43. Kong, S., Sun, Y. and Reitz, R. D. "Modeling Diesel Spray Flame Lift-Off, Sooting Tendency and NOx Emissions using Detailed Chemistry with Phenomenological Soot Model" *Proceedings of the ASME ICED Spring Technical Conference,* April 2005.

44. ASTM International. "ASTM D6751-07b, Standard Specification for Biodiesel Fuel Blend Stock (B100) for Middle Distillate Fuels" Annual Book of ASTM Standards. ASTM International. West Conshohocken, PA: 2008.

45. Bajpai, D. and Tyagi, V. K."Biodiesel: Source, Production, Composition, Properties and its Benefits" *Journal of Oleo Science,* 55, 10 (2006) 487-502

46. Rittman, B. E."Opportunities for Renewable Bioenergy using Microorganisms" *Biotech Bioeng,* 100, 2 (2008)

47. Searchinger, T., Heimlich, R., Houghton, R. A., Dong, F., Elobeid, A., Fabiosa, J., Tokgoz, S., Hayes, D. and Yu, T."Use of U.S. Croplands for Biofuels Increases Greenhouse Gases through Emissions from Land-use Change" *Science,* 319, 5867 (2008) 1238-1240

48. National Institute of Standards and Technology. "Chemistry WebBook: Standard Reference Database Number 69" Available at: http://webbook.nist.gov/chemistry/

49. Yuan, W., Hansen, A. C. and Zhang, Q."Predicting the Physical Properties of Biodiesel for Combustion Modeling" *Trans. ASAE,* 46, 3 (2003) 1487-1493

50. Yuan, W., Hansen, A. C., Tat, M. E., Van Gerpen, J. H. and Tan, Z."Spray, Ignition, and Combustion Modeling of Biodiesel Fuels for Investigating NOx Emissions" *Trans. ASAE,* 48, 3 (2005) 933-939

51. Halstead, M. P., Kirsch, L. J. and Quinn, C. P."The Autoignition of Hydrocarbon Fuels at High Temperatures and Pressure-Fitting of a Mathematical Model" *Combust. Flame*, 30, (1977) 45-60

52. Stringer, V., McCrady, J., Hansen, A. and Lee, C. F. "Modeling Biodiesel Spray Breakup with Well-Defined Fuel Properties" *ILASS-Americas 2007,* May 9, 2007.

53. Zeng, Y. and Lee, C. F."A Model for Multicomponent Spray Vaporization in a High-Pressure and High-Temperature Environment" *J. Eng. Gas Turbines Power,* 124, (2002) 717-724

54. Chakravarthy, K., McFarlane, J., Daw, C. S., Ra, Y., Reitz, R. D. and Griffin, J."Physical Properties of Bio-Diesel and Implications for use of Bio-Diesel in Diesel Engines" *SAE,* 2007-01-4030 (2007)

55. Ra, Y., Reitz, R. D. and McFarlane, J."Effects of Fuel Physical Properties on Diesel Engine Combustion using Diesel and Bio-Diesel Fuels" *SAE,* 2008-01-1379 (2008)

56. Fisher, E. M., Pitz, W. J., Curran, H. J. and Westbrook, C. K."Detailed Chemical Kinetic Mechanisms for Combustion of Oxygenated Fuels" *Proc. Combust. Inst.,* 28, (2000) 1579-1586

57. Gaïl, S., Thomson, M. J., Sarathy, S. M., Syed, S. A., Dagaut, P., Diévart, P., Marchese, A. J. and Dryer, F. L."A Wide-Ranging Kinetic Modeling Study of Methyl Butanoate Combustion" *Proc. Combust. Inst.,* 31, 1 (2007) 305-311

58. Hakka, M. H., Glaude, P., Herbinet, O. and Battin-Leclerc, F."Experimental Study of the Oxidation of Large Surrogates for Diesel and Biodiesel Fuels" *Combust. Flame,* 156, 11 (2009) 2129-2144

59. Herbinet, O., Pitz, W. J. and Westbrook, C. K."Detailed Chemical Kinetic Mechanism for the Oxidation of Biodiesel Fuels Blend Surrogate" *Combust. Flame,* 157, 5 (2010) 893-908

60. Herbinet, O., Pitz, W. J. and Westbrook, C. K."Detailed Chemical Kinetic Oxidation Mechanism for a Biodiesel Surrogate" *Combust. Flame,* 154, 3 (2008) 507-528

61. Brakora, J. L., Ra, Y., Reitz, R. D., McFarlane, J. and Daw, C. S."Development and Validation of a Reduced Reaction Mechanism for Biodiesel-Fueled Engine Simulations" *SAE Int. J. Fuels Lubr.,* 1, 1 (2008)

62. Kong, S., Sun, Y. and Reitz, R. D."Modeling Diesel Spray Flame Lift-Off, Sooting Tendency, and NOx Emissions using Detailed Chemistry with Phenomenological Soot Model" *J. Eng. Gas Turbines Power,* 129, (2007) 245-251

63. Cheng, A. S., Upatnieks, A. and Mueller, C. J."Investigation of the Impact of Biodiesel Fueling on NOx Emissions using an Optical DI Diesel Engine" *Int. J. Engine Res.,* 7, 4 (2006) 297-317

64. Hoffman, S. R. and Abraham, J."A Comparative Study of n-Heptane, Methyl Decanoate, and Dimethyl Ether Combustion Characteristics Under Homogeneous-Charge Compression-Ignition Engine Conditions" *Fuel,* 88, (2009) 1099-1108

65. Song, J., Zello, V., Boehman, A. L. and Waller, F. J."Comparison of the Impact of Intake Oxygen Enrichment and Fuel Oxygenation on Diesel Combustion and Emissions" *Energy Fuels,* 18, (2004) 1282-1290

66. Brakora, J. L. and Reitz, R. D."Investigation of NOx Predictions from Biodiesel-Fueled HCCI Engine Simulations using a Reduced Chemical Kinetic Mechanism" *SAE,* 2010-01-0577 (2010)

67. Sarathy, S. M., Gaïl, S., Syed, S. A., Thomson, M. J. and Dagaut, P."A Comparison of Saturated and Unsaturated C4 Fatty Acid Methyl Esters in an Opposed Flow Diffusion Flame and a Jet Stirred Reactor" *Proc. Combust. Inst.,* 31, 1 (2007) 1015-1022

68. Seiser, H., Pitsch, H., Seshadri, K., Pitz, W. J. and Curran, H. J."Extinction and Autoignition of n-Heptane in Counterflow Configuration" *Proc. Combust. Inst.,* 28, (2000) 2029-2037

69. Golovitchev, V. I. "Mechanisms (combustion chemistry)" Available online at: www.tfd.chalmers.se/~valeri/MECH.html

70. Lu, T. and Law, C. K."A Directed Relation Graph Method for Mechanism Reduction" *Proc. Combust. Inst.,* 30, 1 (2005) 1333-1341

71. Lu, T. and Law, C. K."Linear Time Reduction of Large Kinetic Mechanisms with Direct Relation Graph: N-Heptane and Iso-Octane" *Combust. Flame,* 144, (2006) 24-36

72. Lu, T. and Law, C. K."Strategies for Mechanism Reduction for Large Hydrocarbons: N-Heptane" *Combust. Flame,* 154, 1-2 (2008) 153-163

73. Pepiot-Desjardins, P. and Pitsch, H."An Efficient Error-Propagation-Based Reduction Method for Large Chemical Kinetic Mechanisms" *Combust. Flame,* 154, 1-2 (2008) 67-81

74. Shi, Y., Ge, H., Brakora, J. L. and Reitz, R. D."Automatic Chemistry Mechanism Reduction of Hydrocarbon Fuels for HCCI Engines Based on DRGEP and PCA Methods with Error Control" *Energy Fuels,* 24, 3 (2010) 1646-1654

75. Seshadri, K., Lu, T., Herbinet, O., Humer, S., Niemann, U., Pitz, W. J., Seiser, R. and Law, C. K."Experimental and Kinetic Modeling Study of Extinction and Ignition of Methyl Decanoate in Laminar Non-Premixed Flows" *Proc. Combust. Inst.,* 32, 1 (2009) 1067-1074

76. Luo, Z., Lu, T., Som, S. and Longman, D. E. "Numerical Study on Combustion Characteristics of Biodiesel using a New Reduced Mechanism for Methyl Decanoate as Surrogate" *Proceedings of ICEF '10*, September 2010.

77. Luo, Z., Plomer, M., Lu, T., Som, S. and Longman, D. E. "A Reduced Mechanism for Biodiesel Surrogates with Low Temperature Chemistry" *7th US National Combustion Meeting,* March 20-23, 2011.

78. Reaction Design. "CHEMKIN-Pro." Release 15101 (2011).

79. Knovel. Knovel Critical Tables (2nd Edition). Knovel Corporation, (2008) Available at: http://search.library.wisc.edu/catalog/ocm51847053.

80. Ra, Y. and Reitz, R. D."The Application of a Multicomponent Droplet Vaporization Model to Gasoline Direct Injection Engines" *Int. J. of Engine Res.*, 4, 3 (2003) 193-218

81. Fisher, B. T., Knothe, G. and Mueller, C. J."Liquid-Phase Penetration Under Unsteady in-Cylinder Conditions: Soy- and Cuphea-Derived Biodiesel Fuels Versus Conventional Diesel" *Energy Fuels,* 24, (2010) 5163-5180

82. Ott, L. S. and Bruno, T. J."Variability of Biodiesel Fuel and Comparison to Petroleum-Derived Diesel Fuel: Application of a Composition and Enthalpy Explicit Distillation Curve Method" *Energy Fuels,* 22, 4 (2008) 2861-2868

83. Osmont, A., Catoire, L. and Dagaut, P."Thermodynamic Data for the Modeling of the Thermal Decomposition of Biodiesel. 1. Saturated and Monounsaturated FAMEs" *J. Phys. Chem. A,* 114, 11 (2010) 3788-3795

84. Mueller, C. J., Boehman, A. L. and Martin, G. C."An Experimental Investigation of the Origin of Increased NOx Emissions when Fueling a Heavy-Duty Compression-Ignition Engine with Soy Biodiesel" *SAE,* 2009-01-1792 (2009)

85. Higgins, B. S., Mueller, C. J. and Siebers, D. L."Measurements of Fuel Effects on Liquid-Phase Penetration in DI Sprays" *SAE,* 1999-01-0519 (1999)

86. Bamgboye, A. I. and Hansen, A. C."Prediction of Cetane Number of Biodiesel Fuel from the Fatty Acid Methyl Ester (FAME) Composition" *Int. Agrophysics,* 22, (2008) 21-29

87. Upatnieks, A. and Mueller, C. J."Investigation of the Relationship between DI Diesel Combustion Processes and Engine-Out Soot using an Oxygenated Fuel" *SAE,* 2004-01-1400 (2004)

88. Tran, H. *Investigation of Fuel Property and Biodiesel Effects in a Highly Dilute Low-Temperature Combustion Regime with a Light-Duty Diesel Engine,* M.S. Thesis, University of Wisconsin, Madison, WI, 2010.

89. Koci, C. P., Ra, Y., Krieger, R., Andrie, M., Foster, D. E., Siewert, R. M., Durrett, R. P., Ekoto, I. and Miles, P. C."Detailed Unburned Hydrocarbon Investigations in a Highly-Dilute Diesel Low Temperature Combustion Regime" *SAE,* 2009-01-0928 (2009)

90. Ra, Y. and Reitz, R. D."A Reduced Chemical Kinetic Model for IC Engine Combustion Simulations with Primary Reference Fuels" *Combust. Flame*, 155, (2008) 713-738

91. Brakora, J. L. *Development and Validation of a Reduced Reaction Mechanism for Biodiesel-Fueled Engine Simulations*, M.S. Thesis, University of Wisconsin, Madison, WI, 2007.

92. Naik, C. V., Westbrook, C. K., Herbinet, O., Pitz, W. J. and Mehl, M."Detailed Chemical Kinetic Reaction Mechanism for Biodiesel Components Methyl Stearate and Methyl Oleate" *Proc. Combust. Inst.*, 33, (2011) 383-389

93. Westbrook, C. K., Naik, C. V., Herbinet, O., Pitz, W. J., Mehl, M., Sarathy, S. M. and Curran, H. J."Detailed Chemical Kinetic Reaction Mechanisms for Soy and Rapeseed Biodiesel Fuels" *Combust. Flame,* 158, (2011) 742-755

94. Hansen, R. M. *RCCI Combustion in a Light-Duty Multi-Cylinder Engine,* Preliminary Thesis, University of Wisconsin, Madison, Wisconsin, 2012.

95. Ban-Weiss, G. A., Chen, J. Y., Buchholz, B. A. and Dibble, R. W."A Numerical Investigation into the Anomalous Slight NOx Increased when Burning Biodiesel; A New (Old) Theory" *Fuel Proc. Tech.,* 88, (2007) 659-667

96. Vishwanathan, G. and Reitz, R. D."Numerical Predictions of Diesel Flame Lift-Off Length and Soot Distribution Under Low Temperature Combustion" *SAE,* 2008-01-1331 (2008)

97. Vishwanathan, G. and Reitz, R. D."Development of a Practical Soot Modeling Approach and its Application to Low Temperature Diesel Combustion" *Combust. Sci. Technol.,* 182, 8 (2010) 1050-1082

Appendix A: Supplementary Results and Information

Nomenclature of Species

Below is the species nomenclature relevant to the reduced MD/MD9D mechanism. A more thorough description of the detailed mechanism's species is available on the LLNL mechanism webpage:

https://www-pls.llnl.gov/data/docs/science_and_technology/chemistry/combustion/

= methyl decanoate, md

Saturated methyl esters (e.g., md = methyl decanoate, me = methyl ethanoate):

Unsaturated methyl esters (e.g., mp2d):
name = "saturated ester" + "position of double bond" + "d" (+ "2nd double bond location" + "d")

Alkyl ester radicals (e.g., me2j):
Name = "name of ester" + "position of radical site" + "j"

Peroxy ester radicals (e.g., md6o2):
Name = "name of ester" + "position of O-O group" + "o2"

Hydroperoxy alkyl ester radicals (e.g., md9d6ooh8j):
Name = "name of ester" + "position of O-OH group" + "ooh" + "position of radical" + "j"

OOQOOH ester radicals (e.g., md9d6ooh8o2):
Name = "name of ester" + "position of O-OH group" + "ooh" + "position of OO" + "o2"

Ketohydroperoxide ester molecules (e.g., mdket68):
Name = "name of ester" + "ket" + "position of carbonyl group" + "position of O-OH group"

Hydroperoxydes (e.g., md6ooh):
Name = "name of ester" + "position of O-OH group" + "ooh"

Alkenes (e.g., c7h14-1 = 1-heptane):
Name = c_xh_{2x} + "-" + "position of double bond"

Alkyl radicals (e.g., c7h15-1 = 1-heptane):
Name = c_xh_{2x+1} + "-" + "position of radical site".

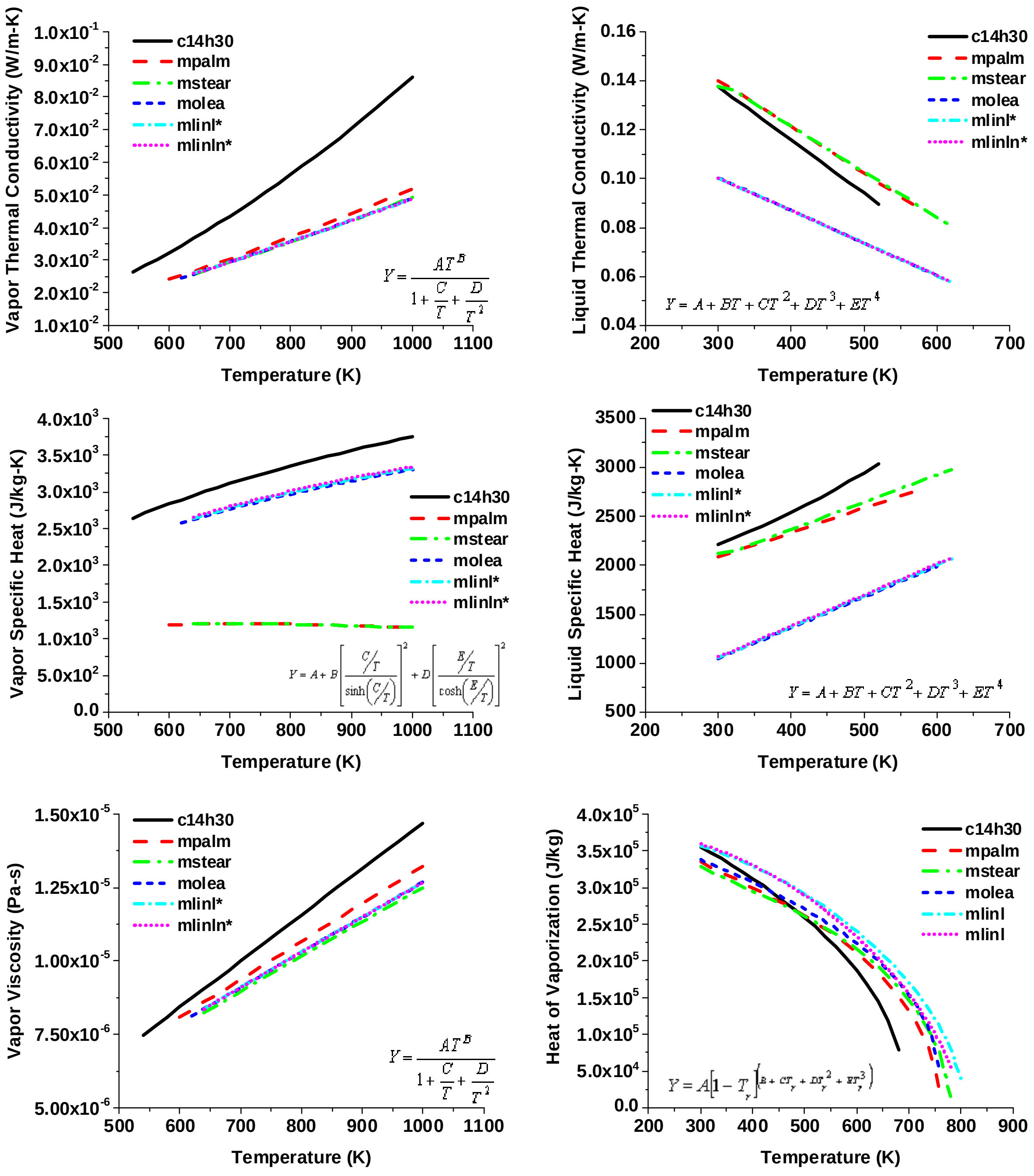

Figure A-1: Comparison of remaining physical properties required by the DMC code; also see corresponding Figure 4-1.

Table A-1: Reactions combined in ERC-MultiChem+MD/MD9D mechanism. *Italicized* species were removed in the assimilation. New reactions and parameters are ***bold/italicized***.

Combined reactions	**A**	**b**	**E**
md6ooh8j+o2<=>*md6ooh8o2*	.7450E+13	0.00	.0000E+00
md6ooh8o2<=>mdket68+oh	.1250E+11	0.00	.1785E+05
md6ooh8j+o2<=>mdket68+oh	***.7540E+13***	***0.00***	***.0000E+00***
mf5ooh3j+o2<=>*mf5ooh3o2*	.7540E+13	0.00	.0000E+00
mf5ooh3o2<=>mfket53+oh	.2500E+11	0.00	.2140E+05
mf5ooh3j+o2<=>mfket53+oh	***.7540E+13***	***0.00***	***.0000E+00***
md9d8ooh6j+o2<=>*md9d8ooh6o2*	.7540E+13	0.00	.0000E+00
md9d8ooh6o2<=>md9dket86+oh	.1250E+11	0.00	.1335E+05
md9d8ooh6j+o2<=>md9dket86+oh	***.7540E+13***	***0.00***	***.0000E+00***
md9d6ooh8j+o2<=>*md9d6ooh8o2*	.7450E+13	0.00	.0000E+00
md9d6ooh8o2<=>md9dket68+oh	.1250E+11	0.00	.1785E+05
md9d6ooh8j+o2<=>md9dket68+oh	***.7540E+13***	***0.00***	***.0000E+00***

Table A-2: Reaction rate adjustments made to the Arrhenius parameters in the ERC-MultiChem+MD/MD9D mechanism (adjusted parameters are ***bold/italicized***)

Adjusted reactions	**A**	**b**	**E**	**Notes**
md+oh=md6j+h2o	.4670E+08	1.61	-.3500E+02	
	.1401E+07	1.61	-.3500E+02	0.03A
md+ho2=md6j+h2o2	.5880E+05	2.50	.1486E+05	
	.1764E+04	2.50	***.8916E+03***	0.06E@2000K
md+o2=md6j+ho2	.4000E+14	0.00	.5016E+05	
	.4000E+13	0.00	***.4013E+05***	0.8E@2000K
md9d+oh=md9d6j+h2o	.4670E+08	1.61	-.3500E+02	
	.4670E+10	1.61	-.3500E+02	100A
md9dket68=oh+c2h3cho+ms6oxo7j	.1050E+17	0.00	.4160E+05	
	.2100E+13	0.00	***.3328E+05***	0.8E@500K

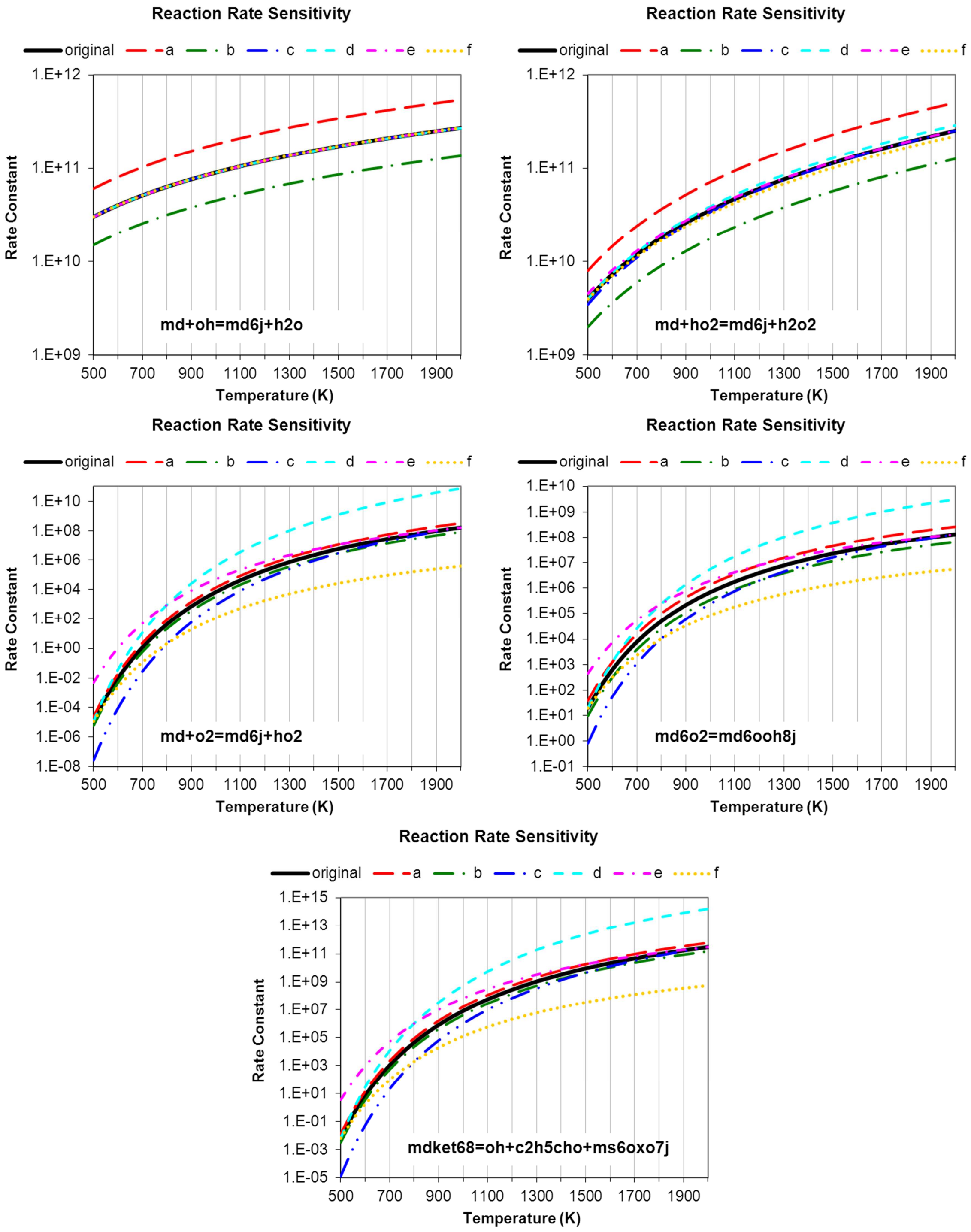

Figure A-2: Reaction rate constant changes observed during ignition delay sensitivity analysis for the ERC-MultiChem+MD/MD9D mechanism. See corresponding Figure 3-9 and Figure 3-10.

Table A-3: Reactions combined in ERC-MultiChem+bio mechanism. *Italicized* species were removed in the assimilation. New reactions and parameters are ***bold/italicized***.

Combined reactions	A	b	E
md6ooh8j+o2=*md6ooh8o2*	.7540E+13	0.00	.0000E+00
md6ooh8o2=mdket68+oh	.1250E+11	0.00	.1785E+05
md6ooh8j+o2=mdket68+oh	***.7540E+13***	***0.00***	***.0000E+00***
mdket68=*mdket68o*+oh	.1050E+17	0.00	.4160E+05
c2h5cho+ms6oxo7j=*mdket68o*	.3330E+11	0.00	.6397E+04
mdket68=oh+c2h5cho+ms6oxo7j	***.1050E+17***	***0.00***	***.4160E+05***
c2h4+*c6h13-1*=c8h17-1	.8800E+04	2.48	.6130E+04
c6h12-1+h=*c6h13-1*	.2500E+12	0.51	.2620E+04
c2h4+c6h12-1+h=c8h17-1	***.8800E+04***	***2.48***	***.6130E+04***
mb4j+*c6h13-1*=md	.8000E+13	0.00	.0000E+00
c6h12-1+h=*c6h13-1*	.2500E+12	0.51	.2620E+04
mb4j+c6h12-1+h=md	***.8000E+13***	***0.00***	***.0000E+00***
md9d6ooh8j+o2=*md9d6ooh8o2*	.7540E+13	0.00	.0000E+00
md9d6ooh8o2=md9dket68+oh	.1250E+11	0.00	.1785E+05
md9d6ooh8j+o2=md9dket68+oh	***.7540E+13***	***0.00***	***.0000E+00***
md9d=*ms7j*+c3h5	.2500E+17	0.00	.7100E+05
c2h4+mf5j=*ms7j*	.8800E+04	2.48	.6130E+04
___md9d=c2h4+mf5j+c3h5*___	***.2500E+17***	***0.00***	***.7100E+05***
mf5ooh3j+o2=*mf5ooh3o2*	7.54E+12	0	0.00E+00
mf5ooh3o2=mfket53+oh	2.50E+10	0	2.14E+04
mf5ooh3j+o2=mfket53+oh	***7.54E+12***	***0***	***0.00E+00***
mfket53=oh+*mfket53o*	1.05E+16	0	4.16E+04
ch2cho+mp3oxo=*mfket53o*	3.33E+10	0	6.40E+03
mfket53=oh+ch2cho+mp3oxo	***1.05E+16***	***0***	***4.16E+04***
mp3oxo+oh=*mp3oxo3j*+h2o	2.69E+10	0.76	-3.40E+02
co+me2j=*mp3oxo3j*	1.51E+11	0	4.81E+03
mp3oxo+oh=co+me2j+h2o	***2.69E+10***	***0.76***	***-3.40E+02***

* Rate also adjusted; see Table A-4

Table A-4: Reaction rate adjustments made to the Arrhenius parameters in the ERC-MultiChem+bio mechanism (adjusted parameters ***bold/italicized***)

Adjusted reactions	**A**	**b**	**E**	**Notes**
md+oh=md6j+h2o	.4670E+08	1.61	-.3500E+02	
	.1401E+07	1.61	-.3500E+02	0.03A
md+ho2=md6j+h2o2	.5880E+05	2.50	.1486E+05	
	.1764E+04	2.50	***.8916E+03***	0.06E@2000K
md+o2=md6j+ho2	.4000E+14	0.00	.5016E+05	
	.4000E+13	0.00	***.4013E+05***	0.8E@2000K
md9d+oh=md9d6j+h2o	.4670E+08	1.61	-.3500E+02	
	.2335E+08	1.61	-.3500E+02	0.5A
md9d+ho2=md9d6j+h2o2	.5880E+05	2.50	.1486E+05	
	.2954E+04	2.50	***.2972E+04***	0.2E@2000K
md9dket68=oh+c2h3cho+ms6oxo7j	.1050E+17	0.00	.4160E+05	
	.2100E+13	0.00	***.3328E+05***	0.8E@2000K
md9d=c2h4+mf5j+c3h5	.2500E+17	0.00	.7100E+05	*See note, Table A-3*
	.6250E+16	0.00	.7100E+05	0.25A, high T

Table A-5: Composition of neat methyl esters from LTC experiments of Tran [88]

Analyte	**Area %**		**Binned**		**Normalized**		**Simulated Species**
	SME	**PME**	**SME**	**PME**	**SME**	**PME**	
C8:0	0.00	0.18	-	-	-	-	
C10:0	0.00	0.24	-	-	-	-	
C12:0	0.06	0.77	-	-	-	-	
C14:0	0.12	1.25	-	-	-	-	
C15:1	0.00	0.24	-	-	-	-	
C16:0 (Palmitic Acid)	11.51	42.06	11.74	42.36	11.89	44.08	m. palmitate
C16:1 (Palmitoleic Acid)	0.23	0.30					
C18:0 (Stearic Acid)	4.53	4.70	4.53	4.70	4.59	4.89	m. stearate
C18:1 Trans	0.06	0.12	23.55	37.9	23.84	39.44	m. oleate
C18:1 Cis (Oleic Acid)	23.49	37.78					
C18:2 Trans	0.17	0.30	51.22	10.59	51.86	11.02	m. linoleate
C18:2 Cis (Linoleic Acid)	51.05	10.29					
C20:0	0.41	0.48	-	-	-	-	
C18:3 Trans	0.35	0.24	7.73	0.54	7.83	0.56	m. linolenate
C18:3 (Linolenic Acid)	7.38	0.30					
C20:1	0.06	0.03	-	-	-	-	
C20+ Unknown	0.58	0.73	-	-	-	-	

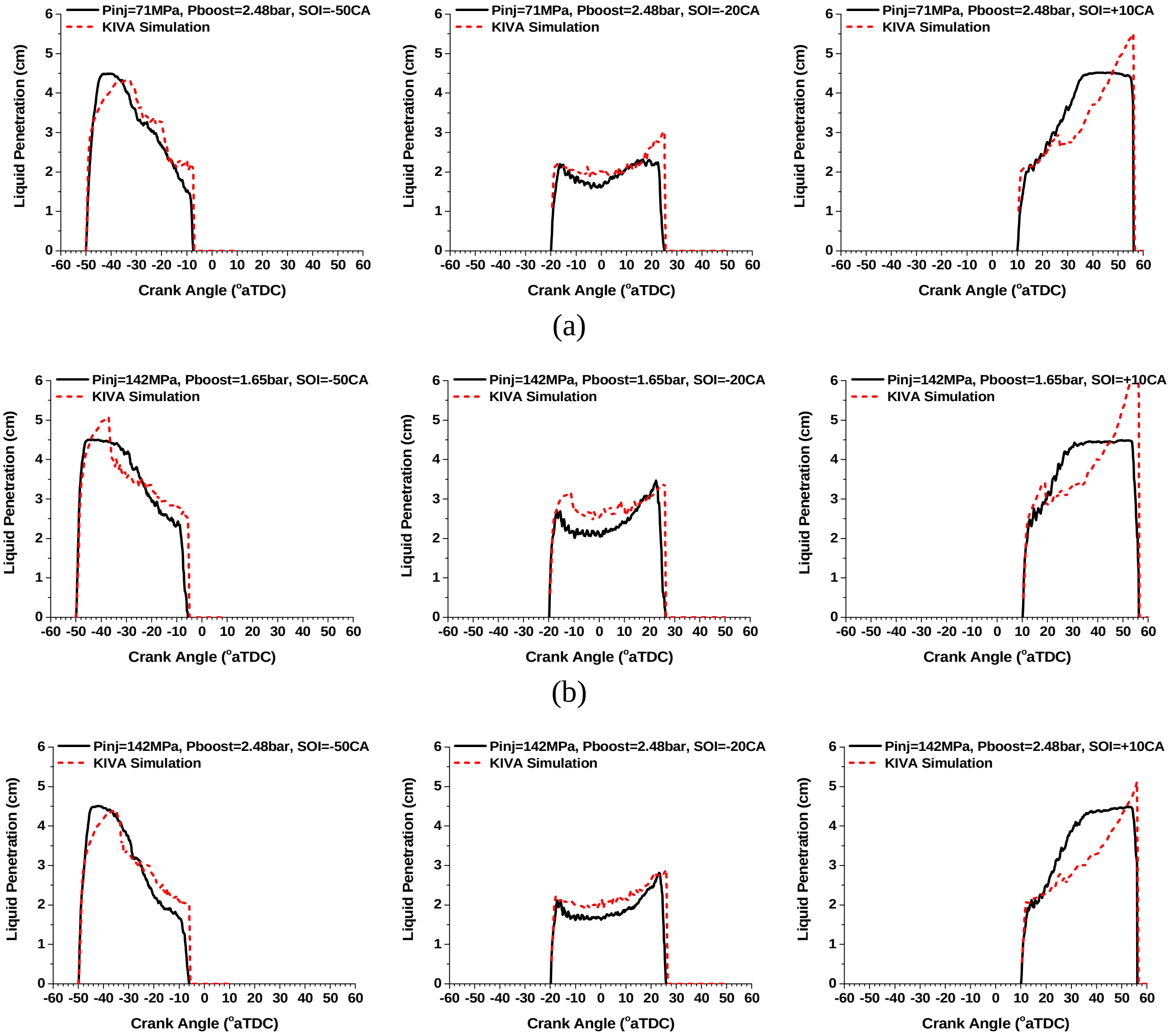

(a)

(b)

(c)

Figure A-3: Liquid lengths predicted for unsteady SCORE spray cases using spray break-up constants of cnst22=80, cnst3rt=0.025, and distant=4.5; (a) P_{inj}=71 MPa, P_{boost}=2.48 bar, (b) P_{inj}=142 MPa, P_{boost}=1.86 bar and (c) P_{inj}=142 MPa, P_{boost}=2.48 bar; see corresponding Figure 4-19.

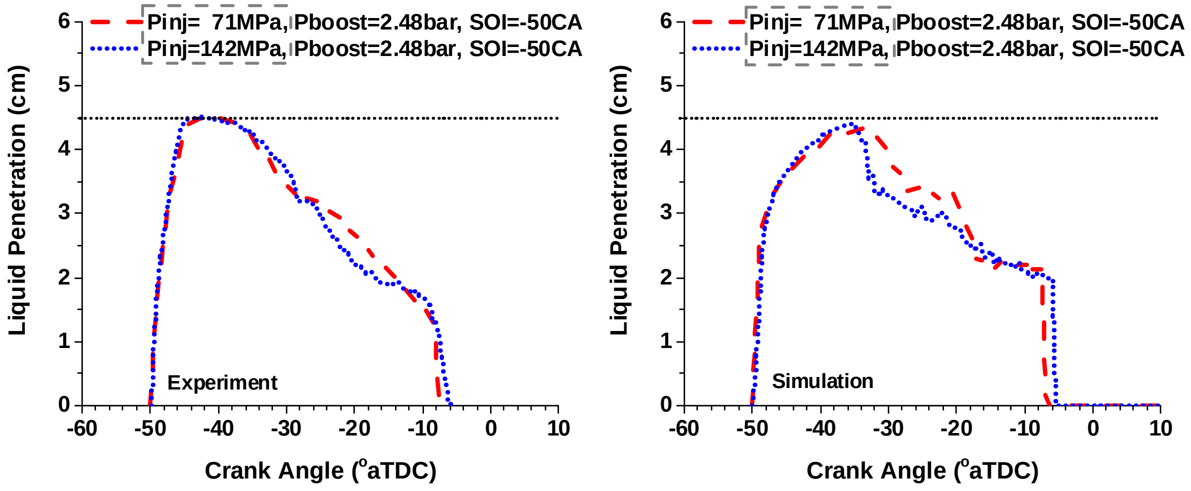

(a) (b)

Figure A-4: Effect of changing injection pressure at the high-boost condition for unsteady SCORE spray (a) experiment and (b) simulation

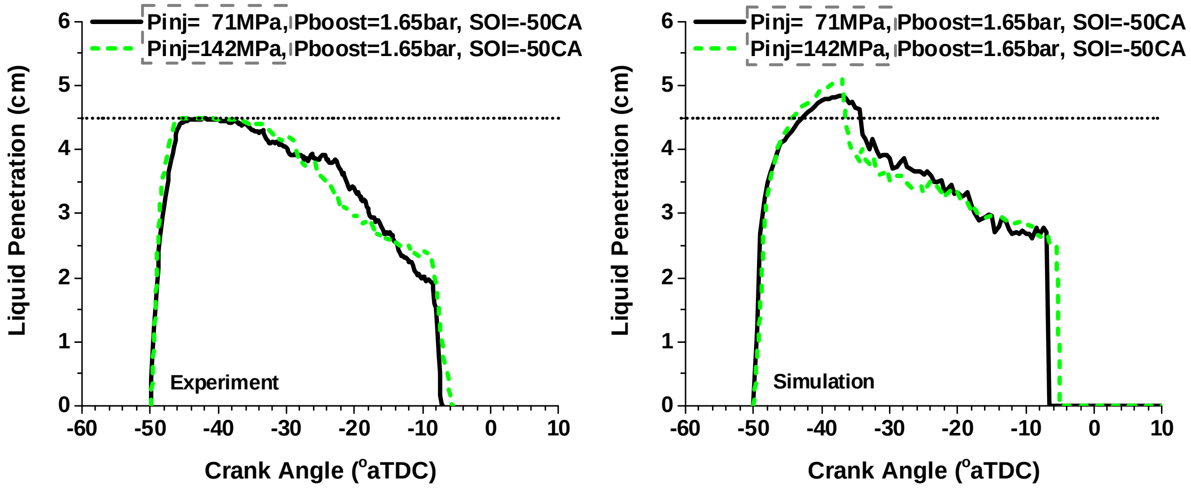

(a) (b)

Figure A-5: Effect of changing injection pressure at the low-boost condition for unsteady SCORE spray (a) experiment and (b) simulation

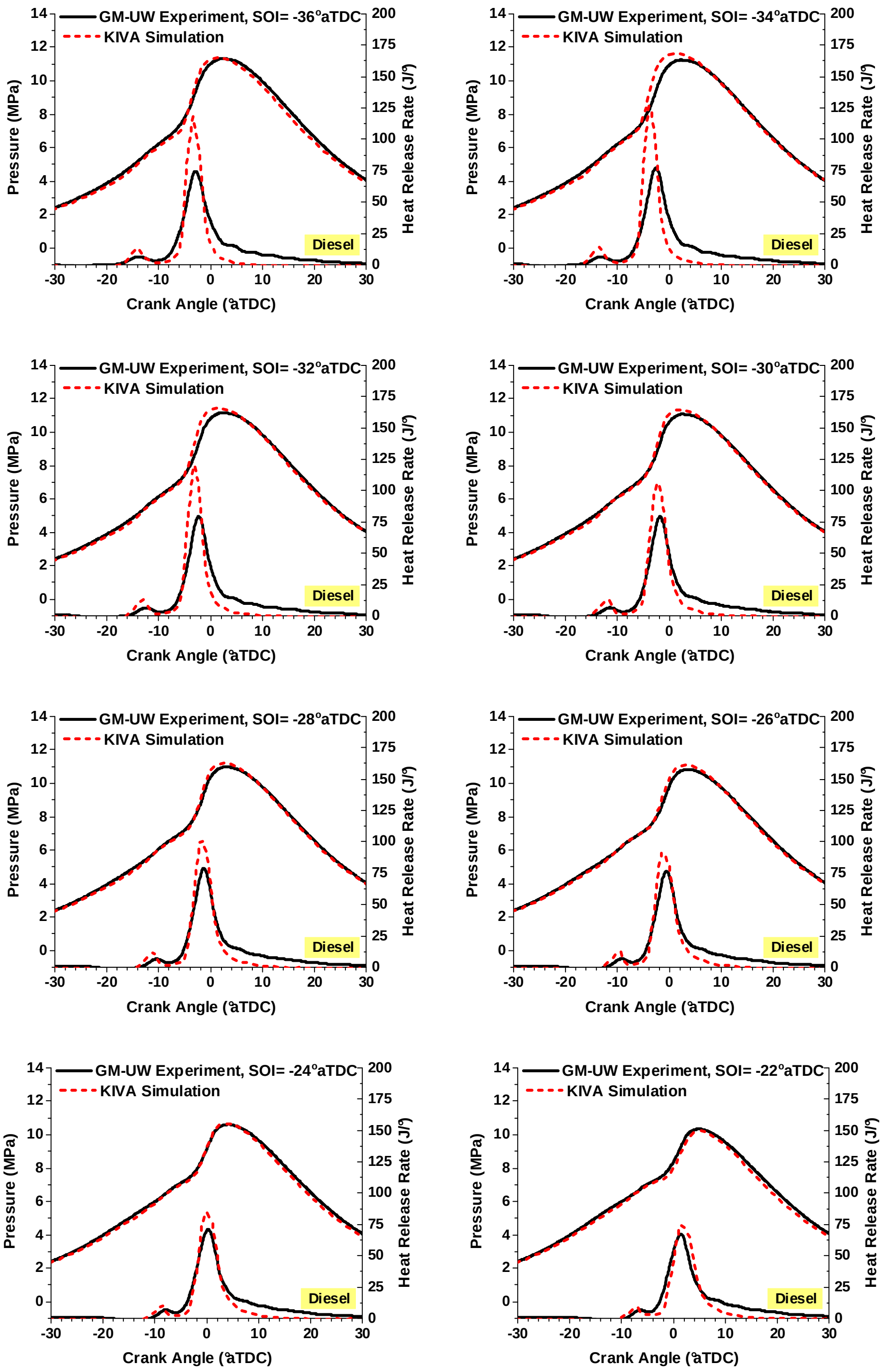

Figure A-6: Experimental (solid) and simulation (dashed) SOI timings pressure and heat release rate results for the LTC diesel fuel

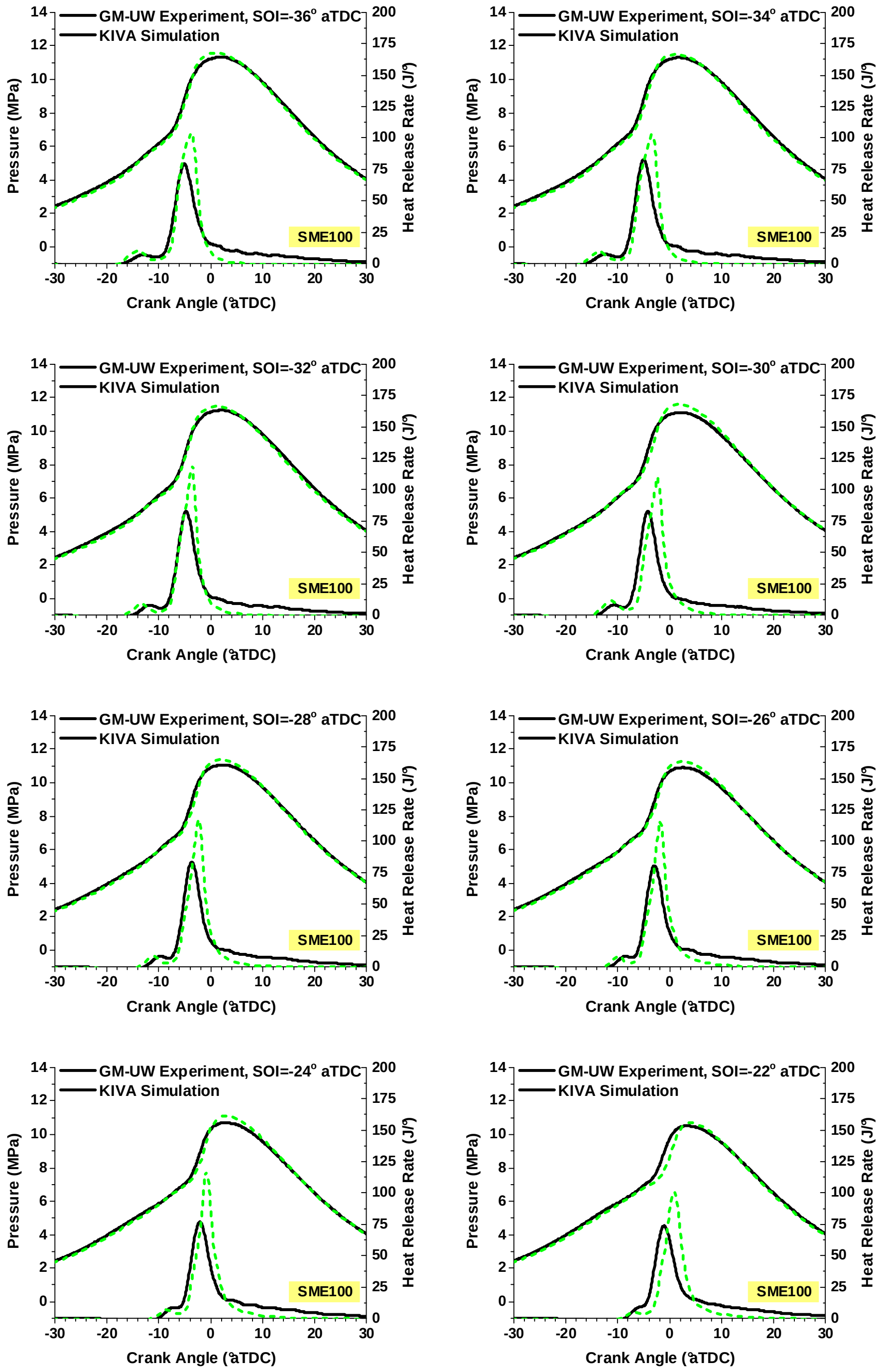

Figure A-7: Experimental (solid) and simulation (dashed) SOI timings pressure and heat release rate results for the LTC SME100 fuel

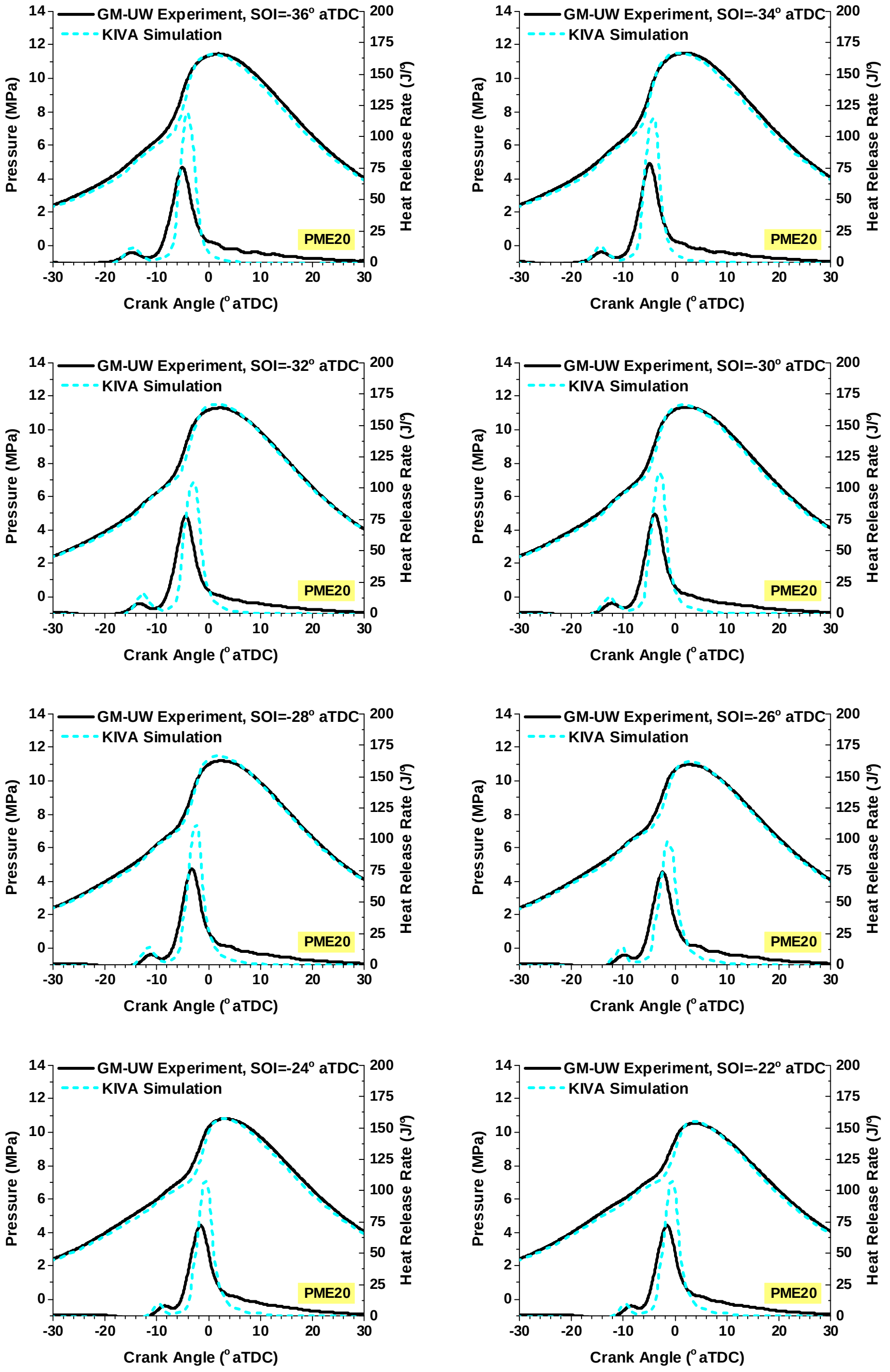

Figure A-8: Experimental (solid) and simulation (dashed) SOI timings pressure and heat release rate results for the LTC PME20 fuel

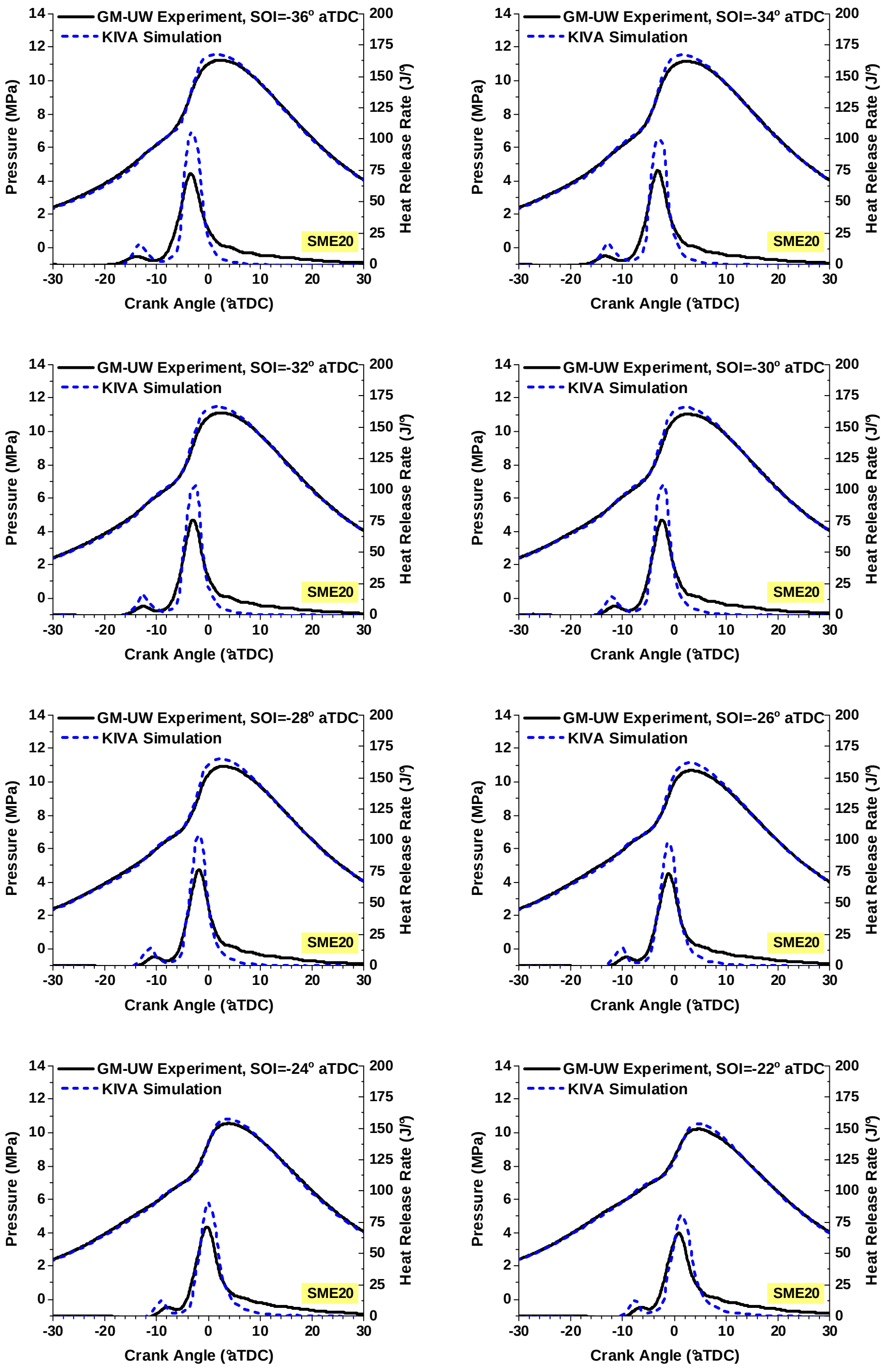

Figure A-9: Experimental (solid) and simulation (dashed) SOI timings pressure and heat release rate results for the LTC SME20 fuel

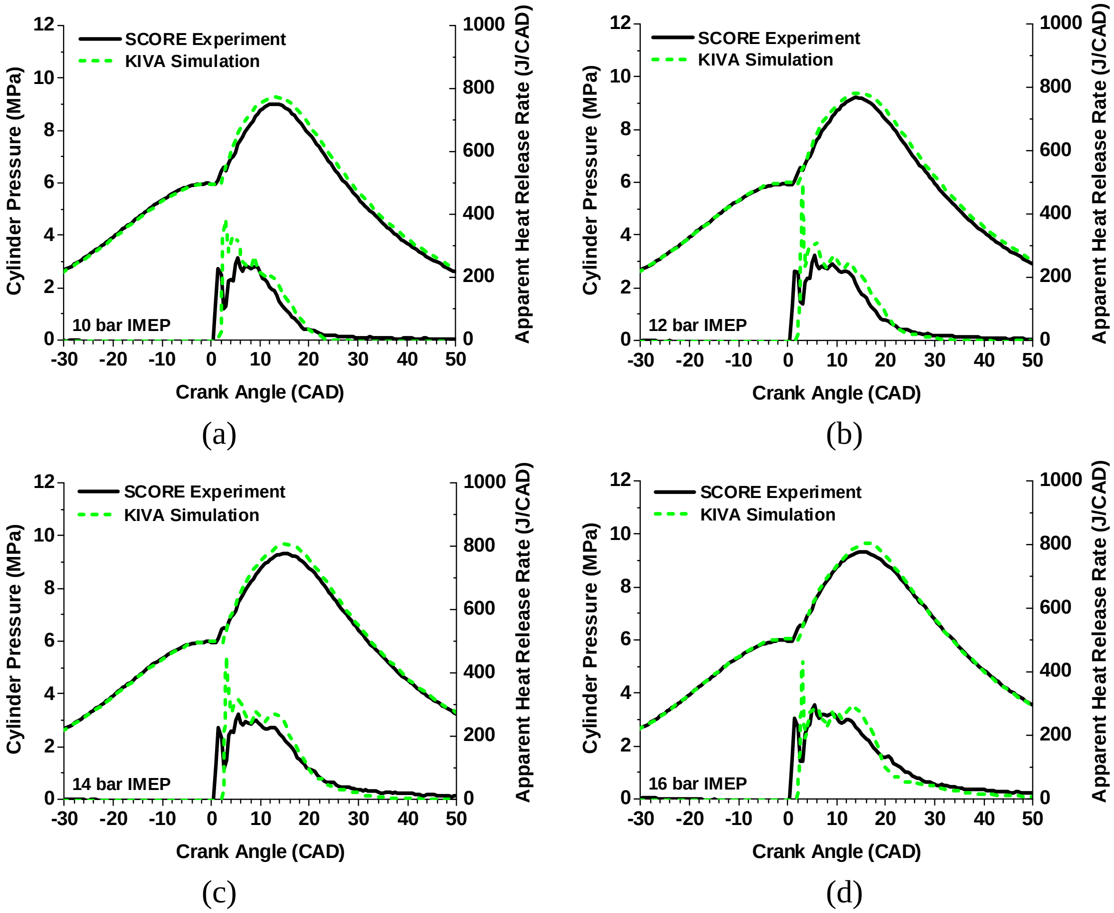

(a) (b)

(c) (d)

Figure A-10: SCORE conventional combustion pressure and heat release rate predictions using the new biodiesel strategy; load of (a) 10 bar, (b) 12 bar, (c) 14 bar, and (d) 16 bar IMEP

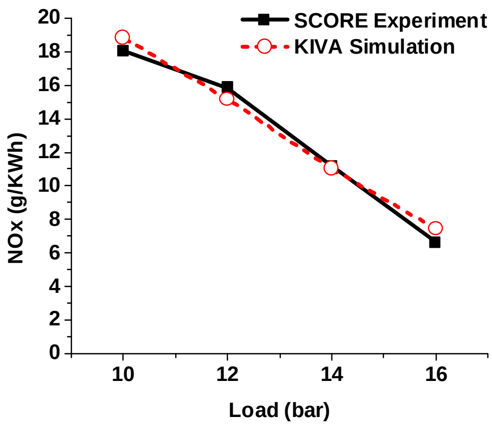

Figure A-11: NOx emissions predictions for the four SCORE conventional combustion loads

Appendix B: Mechanism Reduction Manual

Mechanism Reduction Manual

DRG Method and General Reduction Guidelines

Jessica Brakora
Engine Research Center
2012

This manual includes instructions for setting up and running the automated DRG reduction code and gives general guidelines for reducing mechanisms.

B.1 Introduction

The Directed Relation Graph (DRG) method is a way to identify important species and easily reduce very large detailed mechanisms. The concept is shown in Figure B-1. A control species, “A”, is chosen. This could be any key species of interest and is often important species such as fuel, CO, or HO_2. Once a ***control species*** is chosen, the DRG method will help identify which species in the mechanism are strongly coupled to that control species. In the figure, each species is a node on the graph and an edge is formed if a species significantly contributes to the production rate of a key species. Species B contributes to A, and would be kept. Also, species D is strongly coupled to B, and would therefore be linked to A as well. Species E and F are strongly coupled to each other, but since neither of them is a control species, they would be removed.

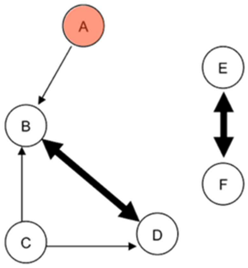

Figure B-1: Schematic of DRG concept

The DRG method determines a species’ contribution to the control species by considering its ***contribution factor,*** r_{AB}. The user specifies a given tolerance for the contribution factor. Species with contribution factors larger than this tolerance are considered significant and left in the mechanism. Species with lower contribution factors are removed.

$$r_{AB,PDP} \equiv \frac{\sum_{i=1,I} \left| \nu_{A,i} \omega_i \delta_{Bi} \right|}{\max(P_A, C_A)} \tag{B-1}$$

where

$$P_A = \sum_{i=1,I} \max(0, \nu_{A,i} \omega_i)$$

$$C_A = \sum_{i=1,I} \max(0, -\nu_{A,i} \omega_i)$$

The DRG method was applied in the Senkin program by ERC alumni, Dr. Yu Shi. More information regarding the inputs and structure of the Senkin program is available in the user manual on the ERC Wiki under the Computational Resources section:

https://info.erc.wisc.edu/twiki/pub/ERC/ComputationalResources/senkin3manual.pdf

B.2 Overview of Code

The automated code is run on Windows. Users can set up a constant volume, constant pressure, or HCCI engine Senkin case and the code automatically reduces very large detailed mechanisms at the given conditions. Intermediate reduced mechanisms are tested against results of the detailed mechanism. If specified error tolerances are not exceeded, a Senkin-DRG run is repeated with an increased DRG contribution factor. The larger contribution factor is more stringent, so fewer species will qualify as significant, resulting in a smaller intermediate mechanism. The reduction-check process continues until output error tolerances are violated or there are no more species to remove. Figure B-2 is a schematic of the process. The process is completely automated and described in detail in ***Energy Fuels* 24 (2010) pp 1646–1654**. More information can be found regarding the DRG reduction process in the following references:

- Lu and Law, *Proc Comb Inst* 30 (2005) pp1333-1341
- Lu and Law, *Combust Flame* 144 (2006) pp24-36
- Lu and Law, *Combust Flame* 146 (2006) pp472-483
- Pepiot and Pitsch, *Combust Flame* 154 (2008) pp67-81
- Liang, Stevens and Farrell, *Proc Comb Inst* 32 (2009) pp527-534
- Turanyi: *New J Chem*, 14 (1990) pp795-803

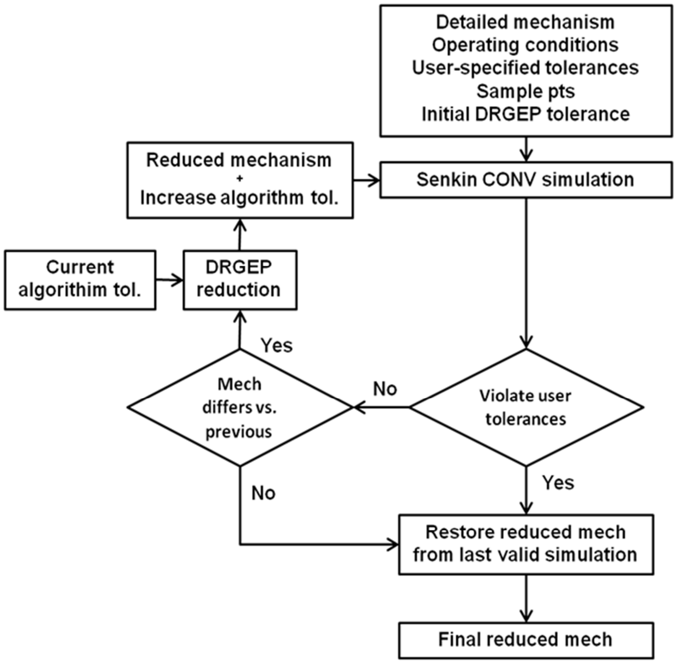

Figure B-2: Schematic of automated DRG reduction process

B.3 Preparation

The original code was designed for HCCI cases only. It was adapted to include constant volume (CONV), and constant pressure (CONP) as well. (*NOTE: the CONP case has not been thoroughly tested). HCCI has the benefit of time-dependent changes in pressure and temperature like those seen in an engine, but the CONP/CONV cases give results that are translatable to engine cases, can be applied over a greater range of conditions, and are easily compared resulting ignition-delay time against shock tube data, if it is available.

Step 1: Choose a case type: CONV, CONP, or HCCI

(Specified in *senk.inp* input file)

Once a case type is chosen, the test conditions must be chosen. Each DRG run creates a reduced mechanism that is accurate for the tested condition only. Strategically chosen DRG conditions can result in mechanisms that are valid for a wider range of conditions. High temperature combustion requires few reactions, and therefore fewer species are important in high temperature conditions. If high temperature conditions are chosen for the DRG reduction process, a very small mechanism will result, but it will be missing valuable species for low temperature combustion. The same can be said for rich conditions. Unless you are reducing a mechanism that will strictly be used under rich conditions (i.e., soot formation), it is beneficial to choose stoichiometric (ϕ=1) or leaner. Stoichiometric is a good place to start, unless you are specifically interested in optimizing for lean (i.e., LTC) conditions.

Step 2: Choose operating conditions

(Specified in *senk.inp* input file)
CONV/CONP: T=800-900K, P=40-60bar, ϕ=0.5-1.0
HCCI: ϕ=0.5-1.0, T and P are engine specific

Users have the ability to control what determines if an intermediate reduced mechanism is "acceptable". Ignition timing, as ignition delay time for CONV/CONP or CA50 for HCCI, is automatically chosen as a test parameter. The user can then choose a thermodynamic condition (peak pressure or peak temperature) and a chemistry condition (max heat release or peak species mole fraction). These two parameters are specified in the itapeCONST or itapeHCCI input file.

Step 3: Choose test paramters of interest

(Specified in *itapeCONST* or *itapeHCCI* input file)
"ikeytherm" thermodynamic property: 1=peakP, 2=peakT
"ikeychem" chemistry property: 1=maxHR, 2=peak species

It is recommended that you create one (1) directory on your computer for the mechanism (e.g., "Mechanism"), and two (2) directories on your computer for your DRG reduction runs. The first run directory is for the detailed mechanism results (e.g., "Detailed"). The second run directory will be for the reduction steps (e.g., "Reduced").

> *Note: Save a copy of ***all*** the initial input files somewhere in case you want to rerun from the beginning.

The next step is to run the detailed mechanism for the case and conditions chosen previously. Set up the input files according to the "**File Requirements and Input Descriptions**" section. Instructions for setting up and running the code on Windows are found in the "**Preparing and Running the Code on Windows**" section.

Step 4: Run the detailed mechanism for the given conditions

(See *Preparing and Running the Code on Windows* section)

It is now time to prepare to reduce the mechanism. Copy the *senk.inp, save.bin,* and *chem.bin* files from the ***Detailed*** directory into the ***Reduced*** directory. There should be a total of 10 files in the ***Reduced*** directory (see the **File Requirements…** section).

Step 5: Copy detailed *senk.inp, save.bin,* and *chem.bin* files for reduced run
(See *File Requirements…* section)

Two additional files must be changed for the reduction process. When the detailed mechanism is run, results for the three chosen test parameters are printed to the *keyreduce.out* file. These values should be copied to the *control.inp* file in the ***Reduced*** run directory. Also, error tolerances for these test parameters should be specified in the same *control.inp* file. These error tolerances are the percent error for the test parameters (i.e., ignition time, peak temperature/pressure, and max HR/species) that is deemed acceptable for the reduction process. Higher error tolerances will allow more species to be reduced, at the expense of accuracy.

Step 6: Copy/paste detailed output and set error tolerances
(Specified in *control.inp* input file)

The *drgpca.inp* file contains inputs for the DRG method. The first line is the DRG contribution factor tolerance. A suggested value for the DRG contribution factor tolerance is ***1.0e-4***. This is the initial tolerance value to decide if species are important in the DRG process. It is increased with successive DRG iterations allowing fewer species in the reduced mechanism. The two PCA method tolerances can be ignored.

Next, the user must choose key control species for the DRG method (species “A” from the **Introduction** section). Any species of interest can be used here, but it is recommended to use the fuel, CO, and HO_2 species. Other species may include soot precursor species (e.g., C_2H_2) for soot mechanisms, or other important intermediates.

Step 7: Choose control species for DRG analysis
(Specified in *drgpca.inp* input file)

Finally, users must specify sample points for the DRG analysis. Any number of temperature or time/CA points can be chosen. Figure B-3 depicts the two options. At each sample point DRG will be performed for each control species.

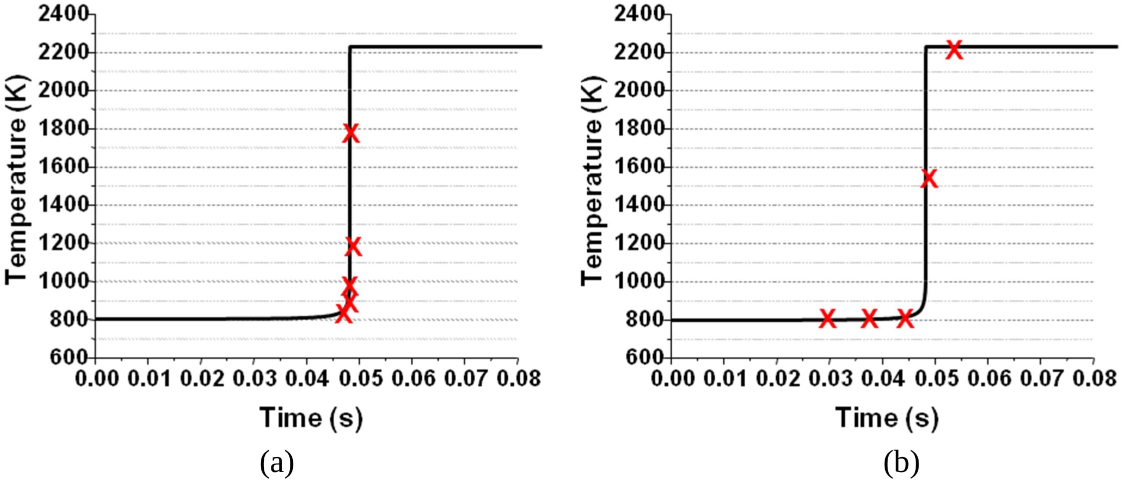

(a) (b)

Figure B-3: Identifying (a) temperature-based or (b) time-based sample points for DRG analysis

Step 8: Choose sample points for DRG analysis
(Specified in *drgpca.inp* input file)

Once all of the input files are ready, it is time to reduce the mechanism. In the ***Reduced*** directory, run the *autoreduct.exe* executable according to the steps outlines in the **Preparing and Running the Code on Windows** section. Depending on the size of the detailed mechanism, the reduction process can take a few minutes to an hour. A history of the reduction process is printed to the *history.dat* file. The species/reaction data can be plotted similar to Figure B-4. Error information is also available in this file.

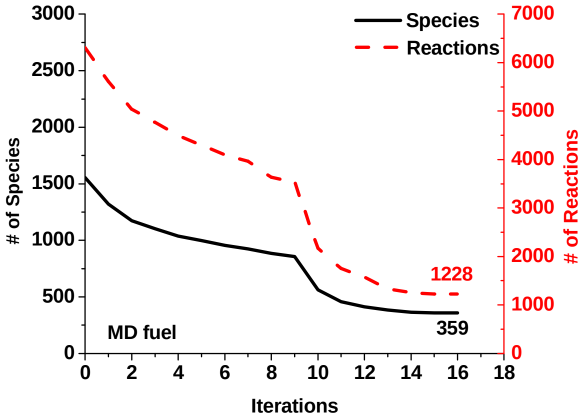

Figure B-4: History output from DRG analysis from *history.dat* output file

Once a reduced mechanism is created, it is important to check that the new mechanism continues to adequately predict other conditions. For example, if the initial CONV test was for 800K at 40bar, use the newly reduced mechanism at 1000K and 1300K, and make sure there are no large discrepancies at the other conditions. Small discrepancies, such as those shown in the ignition delay time plot in Figure B-5, are acceptable. As long as the general shape of the ignition profile is maintained, slight rate constant adjustments can eliminate small differences between the detailed and reduced mechanisms.

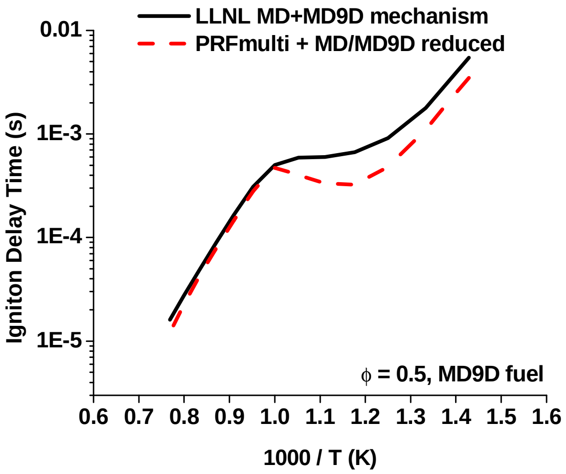

Figure B-5: Example ignition delay comparison of a detailed and DRG-reduced mechanism

*Notes:

1. If you want to rerun a case, make sure you replace the save.bin, chem.bin and drgpca.inp files. They are rewritten after each generation.
2. If you rerun a case with different conditions, you will need to start from the beginning and rerun the detailed case as well. Make sure to change the key property tolerances in control.inp file (from the detailed mechanism's new keyreduce.out file)

If users wish to further reduce the mechanism with manual techniques, more information is available in the Guidelines for Manual Mechanism Reduction section. This section will also cover rate constant adjustments.

B.4 File Requirements

Mechanism directory, 3 files needed:

- **Executable**
  - *ckintp.exe* - CHEMKIN interpreter executable to create mechanism
- **Input files**
  - *mech.dat* - detailed mechanism's species and reaction info (ASCII format)
  - *therm.dat* - thermodynamic data for each species (NASA format)

Detailed directory, 4 files needed:

- **Executable**
  - *senkauto.exe* - ERC single-zone Senkin code w/ DRG & PCA methods
- **Input files**
  - *senk.inp* - Senkin input parameters
  - *itapeHCCI* - HCCI engine parameters (HCCI cases only) -- or -- *itapeCONST* - CONV or CONP parameters (CONV or CONP cases only)
- **Output from Mechanism directory**
  - *chem.bin* - CHEMKIN linking file for detailed mechanism

Reduced directory, 10 files needed:

- **Executables**
  - *autoreduct.exe* - main driver
  - *senkauto.exe* - ERC single-zone Senkin code w/ DRG & PCA methods
  - *ckintp.exe* - interpretor executable (using CKLIB v4.2)
- **Input files**
  - *drgpca.inp* - inputs for DRG & PCA methods
  - *control.inp* - input tolerances for mechanism reduction DRG & PCA methods
  - *senk.inp* - Senkin input parameters
  - *therm.dat* - thermodynamic data to make new CK linking files
  - *itapeHCCI* - HCCI engine parameters (HCCI cases only) -- or -- *itapeCONST* - CONV or CONP parameters (CONV or CONP cases only)
- **Output copied from Detailed directory**
  - *save.bin* - simulation output file from detailed mechanism run
  - *chem.bin* - CHEMKIN linking file for detailed mechanism

B.5 File Descriptions

Input File: senk.inp

This file is used by Senkin to specify the initial conditions for the simulations.

```
CONV                    !case: CONV, CONP, VTIM=HCCI
PRES 60.0               !initial pressure (bar)
TEMP 700.0              !initial temperature (K)
REAC md    0.006776147  !species name, mole fraction
REAC o2    0.206717657
REAC n2    0.779945720
TIME 2.E-2              !amount of time to run simulation (s)
DELT 5.E-5              !timestep for simulation
END
#for phi=1.00 case      !note to keep track of input conditions
```

Input File: itapeHCCI (for HCCI cases only)

This file is used by Senkin in HCCI cases to specify the time-volume information, and the output needed for the DRG calculations and post-processing.

```
12.6          !CR
84.57         !TDC volume [cm^3]
-158.0        !IVC [deg. ATDC]
122.0         !EVO [deg. ATDC]
1200.         !rpm [rev/min]
10.2          !bore [cm]
12.0          !stroke
19.0          !conrod
0             !iskwallheat
0             !initial cond flag (iskegr): 0=senk.inp; 1=simple EGR;
2=fuel mass & PRF
1             !# of fuel species (list name(s) and mw below)
'fuelname' 46.06952
1.4e6         !P_bdc for isfc calc [dyne/cm^2]
2.2e6         !P_exh for isfc calc [dyne/cm^2]
0.5           !efficiency of expansion stroke, isfc calc [-]
0             !flag for DRGEP
0             !flag for PCA
1             !ikeytherm: thermo property; 1=peakP, 2=peakT
1             !ikeychem: chem property; 1=maxHR, 2=peakspec
h2o2          !key spec:  key species to monitor
2             !ispecies: 0=off,1=massfrac,2=mole frac,3=mass,4=mass/mass_f
```

Input File: itapeCONST (for CONP or CONV cases only)

This file is used by Senkin in CONV/CONP cases to specify the output needed for the DRG calculations and post-processing.

```
1        !nfuels: number of fuels in simulation
'fuelname' 186.29679
0        !iDRG
0        !iPCA
1        !ikeytherm: thermo prop; 1=peakP, 2=peakT
2        !ikeychem: chem prop; 1=maxHR (HCCI), 2=peak species
h2o2     !key species name
2        !ispecies: 0=off, 1=mass frac, 2=mole frac,
                          3=mass;      4=mass/mass_f
```

Input File: control.inp

This file is read by AutoReduct.exe to ensure the new mechanism is within given tolerances. *Note: The input file cannot contain comments - will produce an error

```
0                    !Beginning generation number
0.10                 !Ignition time tolerance, % of deg (HCCI) or sec
(CONV/CONP)
0.03                 !Thermo property tolerance (peak P or peak T), %
0.03                 !Chem property tolerance (max HR or peak spec), %
-11.167596           !ignition time from detailed mech simulation
12.875095            !thermo property from detailed mech simulation
2595.506453          !chem property from detailed mech simulation
0                    !0=DRGEP method only, 2=PCA method only, don't use 1
```

Input File: drgpca.inp

This file is required for the Senkin program to do DRG and PCA analyses. *Note: The tolerances are overwritten each generation (keep a copy of the original one for future restarts). This input file cannot contain comments - will produce an error.

```
1.0e-04    !Tolerance for DRGEP
1.0e-02    !Tolerance 1 for PCA
1.0e-02    !Tolerance 2 for PCA
3          !number of control species to consider (list names below)
fuel
ho2
co
6          !npoint, number of check points
3          !ncontrol, property of the check points, 1=time, 2=crank angle,
3=temperature
600.000000
800.000000
1000.000000
1200.000000
1500.000000
2000.000000
```

Output Files:
After the reduction process is complete, you will have the following output files

- *keyreduce.out* - output file needed for DRG
- *save.bin* - complete, binary output file (like otape9 in kiva)
- *rest.bin* - restart file
- *tign.out* - ignition output (information is also in summary.out)
- *summary.out* - summary of important information (below)
    - T_{intial} (K), $P_{initial}$ (MPa), Ignition Delay (s), P_{peak} (MPa) T_{peak} (K), Peak Species (mole fraction), Total Energy (J/cm3), Max HR (J/cm3)
- *history.dat* - history of reduction process;
    - iteration number, number of species and reactions, tolerances, key property outputs, and errors for each iteration
- *species.dat* - only output if ispecies>0 in itapeCONST/itapeHCCI;
    - outputs mass frac, mole frac, mass, or species mass/fuel mass for each species in the mechanism.

B.6 Preparing and Running the Code on Windows

The automatic DRG reduction program will only work on Windows. Use Compaq Visual Fortran to compile and debug the code

B.6.1 *Compiling Code with Compaq Visual Fortran*

1. Install MS Visual Studio for C complier environment in CVF
    a. Get from /plague/Microsoft_Visual_Studio_6.0 (disk1 "setup")
    b. You do not need MSDN library

2. CVF settings: Project > Settings... dropdown menu: "All Configurations"
    a. Fortran tab:
        i. "Fortran Data" (dropdown menu) set Default Real Kind = 8
        ii. "Run time" uncheck Array and String Bounds

3. In the AutoReduct directory, open autoreduct.dsw
    a. Under the FileView tab, highlight "autoreduct files"
    b. Go to Build > Build autoreduct.exe
    c. Copy autoreduct.exe in AutoReduct/debug to working directory

4. In the Interp directory, open ckintp.dsw
    a. Under the FileView tab, highlight "ckintp files"
    b. Go to Build > Build ckintp.exe
    c. Copy ckintp.exe in Interp/debug to working directory

5. In the SenkAuto directory, open driver.dsw
    a. Under the FileView tab, highlight "driver files"
    b. Go to Build > Rebuild All
        i. (2 errors may show up, but they can be ignored)
    c. Move senkauto.exe from SenkAuto/debug to working directory
        i. (may need to rename "SenkAutoOrig.exe" to senkauto.exe)

B.6.2 *Running the Code on Windows*

1. Open a command window
   a. Go to: Start > Run...
   b. Type "cmd" and hit [OK]

2. Create linking file in a separate Mechanism directory (start with the detailed mechanism)
   a. Ensure the mechanism file is named "mech.dat"
   b. Ensure the thermo data file is named "therm.dat"
   c. Run ckintp.exe using cmd
      i. In the command window move to your working directory (cd "directory path")
      ii. Type the executable name "ckintp.exe" to run
   d. Check mech.out to ensure no errors occurred

3. Create detailed mechanism output by running senkauto.exe with DRG & PCA turned off
   a. Create a separate directory for the detailed mechanism run
   b. Copy *senkauto.exe*, *chem.bin*, *senk.inp*, and *itapeCONST/itapeHCCI* to directory
   c. In *itapeCONST/itapeHCCI*, set the flags for DRGEP and PCA to zeros
   d. Run *senkauto.exe* in cmd
      i. In the command window move to your working directory (cd "directory path")
      ii. Type "***senkauto.exe 0***" to run *OR* "***senkauto.exe 0 >filename***" to run and save screen output to a file
          1. The "0" ensures that a new save.bin is generated

4. Create reduced mechanism by running autoreduct.exe with DRG
   a. Go to the Reduced run directory
   b. Copy *chem.bin*, *senk.dat*, and *save.bin* from Detailed directory to the Reduced directory
   c. Copy/paste the data from the detailed run's *keyreduce.out* file to *control.inp*
   d. ***Checks***: ensure that
      i. 10 files are present in the main directory
      ii. Tolerances are correct in *control.inp* and *drgpca.inp*
      iii. The last line in *control.inp* is set to use DRG ("0")
      iv. DRG flag in *itapeCONST/itapeHCCI* is turned on ("1")
      v. PCA flag in *itapeCONST/itapeHCCI* is turned off ("0")
   e. Run autoreduct.exe using cmd
      i. In the command window move to your working directory (cd "directory path")
      ii. Type the executable name "autoreduct.exe" to run

5. Further reduced the mechanism using the PCA method (optional -- not thoroughly tested)
    a. After the DRG case has finished, check the history.dat file
        i. Find the last generation number (e.g. 15)
    b. Rename chem_gen#.bin and save_gen#.bin from last generation to chem.bin and save.bin
    c. Change the first line in *control.inp* to the next gen number (e.g., if last generation is 15, this number would be 16)
    d. Change the last line in *control.inp* to use PCA ("2")
    e. Ensure that the DRG flag in *itapeCONST/itapeHCCI* is turned off ("0")
    f. Ensure that the PCA flag in *itapeCONST/itapeHCCI* is turned on ("1")
    g. Run autoreduct.exe using cmd
        i. In the command window move to your working directory (cd "directory path")
        ii. Type the executable name "autoreduct.exe" to run

B.6.3 *Troubleshooting*

If the code doesn't reduce (fails on first reduction)

1. Increase the % tolerances in *control.inp*
2. Make sure the property checkpoints in *drgpca.inp* are correct
3. Make sure you copied the detailed *keyreduce.out* to *control.inp*

B.7 Checking Output for a Range of Conditions

Once a reduced mechanism is generated, it is important to check the results against the detailed mechanism for a range of conditions. Convenient hades/elephant batch files are prepared to create ignition delay plots using Senkin and GNUPLOT.

The ***IgnitionDelay*** directory is the working directory for ignition delay runs. It contains several directories used for general ignition delay comparisons, as well as the rate constant sensitivity analysis that will be explained later. The following directories are available by default:

- ***Batch***: batch files for automatically running the code and plotting results
- ***Common***: the Senkin executables and itapeCONST files
- ***Detail***: ignition delay output for the detailed mechanism
- ***GNUPLOT***: GNUPLOT plotting files to used to plot the results
- ***Mech***: CHEMKIN interpreter, mechanisms and thermo data files
- ***P##***: Senkin input files (senk.inp) for P=## generated using the *matlabINP.m* batch file

B.7.1 *Setting up the Input Files using Matlab Script*

The first step is to set-up the senk.inp files for the conditions of interest. A matlab script is already set-up to create input files for a given fuel and T-P-ϕ conditions.

Note: Matlab is not on elephant, must be run from hades or condor

1. Copy the *matlabINP.m* file from ***Batch*** to ***P##*** (renamed to your pressure of interest).
2. Set up the *matlabINP.m* file for your fuel:
    a. Change the equivalence ratio and temperature range as needed
    b. Change the 'name' array to match the name of the fuel from mech.dat
    c. Change the nc, nh, no values to match your fuel composition
    d. Change the 'descrip' to your fuel name (can differ from mech.dat)
    e. Change the fracmix value for the fuel(s) of interest
3. To create senk.inp files:
4. From hades:
    a. Type: matlab (initiates Matlab GUI)
    b. From the command line, type: matlabINP
5. From condor:
    a. Type: ssh condor
    b. Login with user password
    c. Type: matlab (initiates Matlab command line only)
    d. From command line, type: matlabINP

B.7.2 *Change Input Files for the Fuels/Conditions of Interest*

The following batch files and plotting files are available:

- *batchID-2mech*: runs reduced/adjusted mechs for 3 equivalence ratios, plots vs. detailed
- *batchID-1mech*: runs reduced mechanism for 3 equivalence ratios, plots vs. detailed
- *batchID-detail*: creates output files for detailed mechanism
- *batchSENS-ab*: runs/plots results for 2 reaction rate adjustments (activation energy = 0)
- *batchSENS-af*: runs/plots results for six reaction rate adjustments
- *matlabINP.m*: creates senk.inp input files
- *ign-sensAB-FUELNAME.plt*: plotting file for use with *batchSENS-ab*
- *ign-sensAF-FUELNAME.plt*: plotting file for use with *batchSENS-af*
- *ign-FUELNAME-1mech.plt*: plotting file for use with *batchID-1mech*
- *ign-FUELNAME-2mech.plt*: plotting file for use with *batchID-2mech*

These files must be changed for the new fuel and operating conditions. For instance, the file *batchSENS-af* is currently set up for "MD" fuel at $\phi = 1.0$ (i.e., "PHI100") and P=40 bar (i.e., "P40").

> ***VI Tip:*** If using VI for text editing, it is easy to replace all instances word/phrase with new text. In the expression below, the "1,$" signifies replacing text in line 1 to the last line. These values can be changed to different numbers if a smaller range of lines need to be changed. The "g" signifies global replacement; if not included, the text will only be replaced to the cursor point.

```
:1,$s/oldtext/newtext/g
```

It is also necessary to change the *itapeCONST* file found in the ***Common*** directory for the given fuel. Copy the following *mech.dat* files to the ***Mech*** folder in the ***IgnitionDelay*** directory.

- detailed mechanism file: renamed *mech-detail.dat*
- original reduced mechanism file (no adjustments): renamed *mech-1.dat*
- adjusted reduced mechanism file (optional): renamed *mech-2.dat*

You will want to have results from the detailed mechanism to compare the reduced and adjusted mechanisms. There are two options. To create Senkin output similar to those of the reduced/adjusted mechanisms, simply submit the batch file named *batchID-detail* on hades or elephant. This may take several hours to run depending on the size of the detailed mechanism. It will create output for three equivalence ratios (0.5, 1.0, 2.0) and one pressure (default of P=40bar). Alternatively, if ignition delay information is already available, the GNUPLOT plotting file can be changed to read in a different format for the detailed mechanism.

B.7.3 *Running the code*

Once the input and mechanism files are created and the batch/plotting files are changed, the code is ready to be submitted. Figure B-6 shows example plots that are created using the *batchID-1mech* and *batchID-2mech* files. These are not high-quality, publishable plots, but can be used to quickly assess the quality of the reduced and/or adjusted mechanisms.

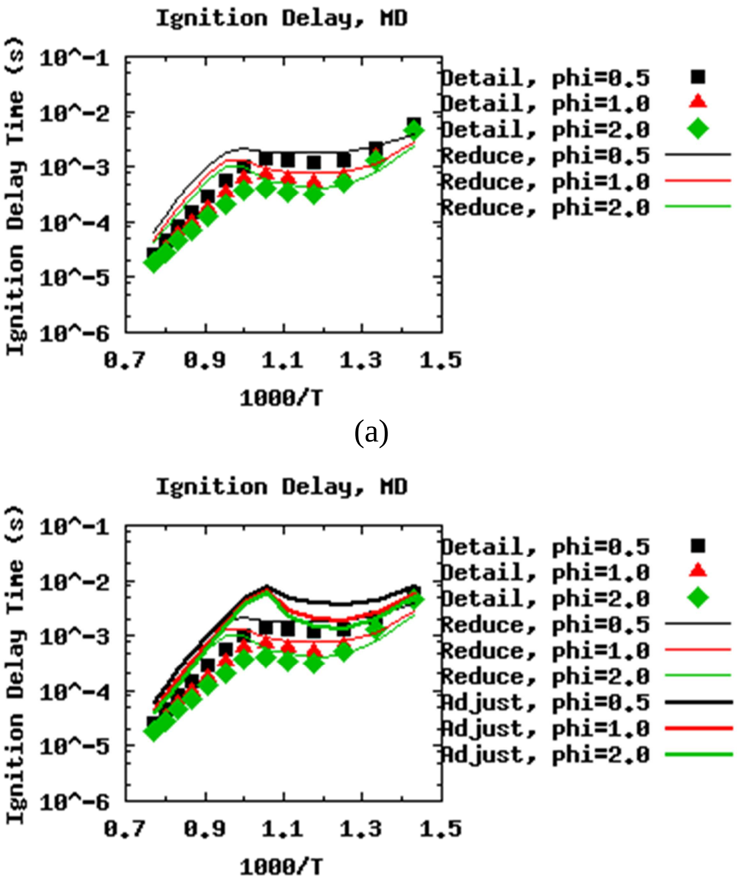

(a)

(b)

Figure B-6: Example ignition delay results from (a) *batchID-1mech* and (b) *batchID-2mech*

B.8 Guidelines for Manual Reduction

B.8.1 *Isomer Lumping*

Large-chain species often decompose into many different isomers. Isomers are species that share the same number of C-H-O elements and the only difference is the location of the radical site (where an H was abstracted). Often they share similar thermodynamic data as well. Figure B-7 depicts an example of fuel decomposition into 10 isomers.

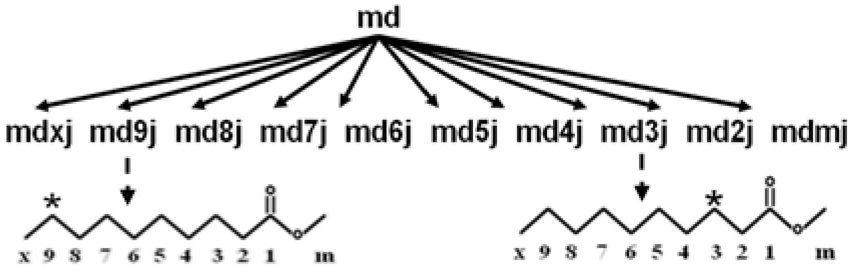

Figure B-7: Example of fuel decomposition to several isomer species

The DRG method above does not account for isomers, and often, after DRG is performed on large mechanisms, several isomers will remain. The first step in manual mechanism reduction is to identify isomers in the mechanism. The *mech.out* file is a good place to start. The top of the file lists the species and elements in each species. Isomers can be identified by their "element count" or molecular weight, and often have similar species names with numbers signifying the different radical sites (e.g., md9d**2**o2/md9d**6**o2 and c4h8ooh1-**2**/c4h8ooh1-**3**). Figure B-8 shows an example *mech.out* with three isomer groups highlighted.

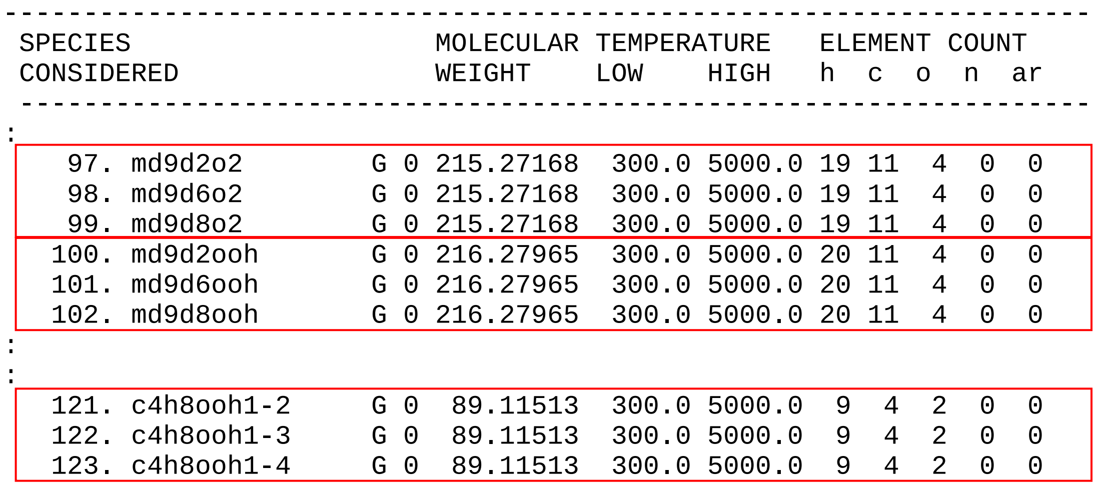

```
 -------------------------------------------------------------------
 SPECIES                          MOLECULAR TEMPERATURE   ELEMENT COUNT
 CONSIDERED                       WEIGHT    LOW    HIGH   h  c  o  n  ar
 -------------------------------------------------------------------
:
    97. md9d2o2         G 0 215.27168  300.0 5000.0 19 11  4  0  0
    98. md9d6o2         G 0 215.27168  300.0 5000.0 19 11  4  0  0
    99. md9d8o2         G 0 215.27168  300.0 5000.0 19 11  4  0  0
   100. md9d2ooh        G 0 216.27965  300.0 5000.0 20 11  4  0  0
   101. md9d6ooh        G 0 216.27965  300.0 5000.0 20 11  4  0  0
   102. md9d8ooh        G 0 216.27965  300.0 5000.0 20 11  4  0  0
:
:
   121. c4h8ooh1-2      G 0  89.11513  300.0 5000.0  9  4  2  0  0
   122. c4h8ooh1-3      G 0  89.11513  300.0 5000.0  9  4  2  0  0
   123. c4h8ooh1-4      G 0  89.11513  300.0 5000.0  9  4  2  0  0
```

Figure B-8: Head of mech.out file highlighting three isomer groups

B.8.2 *CHEMKIN Pro Reaction Pathway Visualization*

Once isomer groups are identified, a user can use CHEMKIN Pro to identify which isomers make the largest contribution to the rate of production of key species. CHEMKIN Pro is available in the software directory of the ERC's Plague server.

Set up a "Closed_Homogeneous (C1)" run with the conditions of interest. Once the run is performed, a pop-up screen will ask how you want to analyze the results. Choose "Analyze Reaction Paths" and "Next Step…" A new screen, shown in Figure B-9, will display the results in graphical format, with several important functions. More information about the functions is available in the CHEMKIN Pro Visualization User Manual.

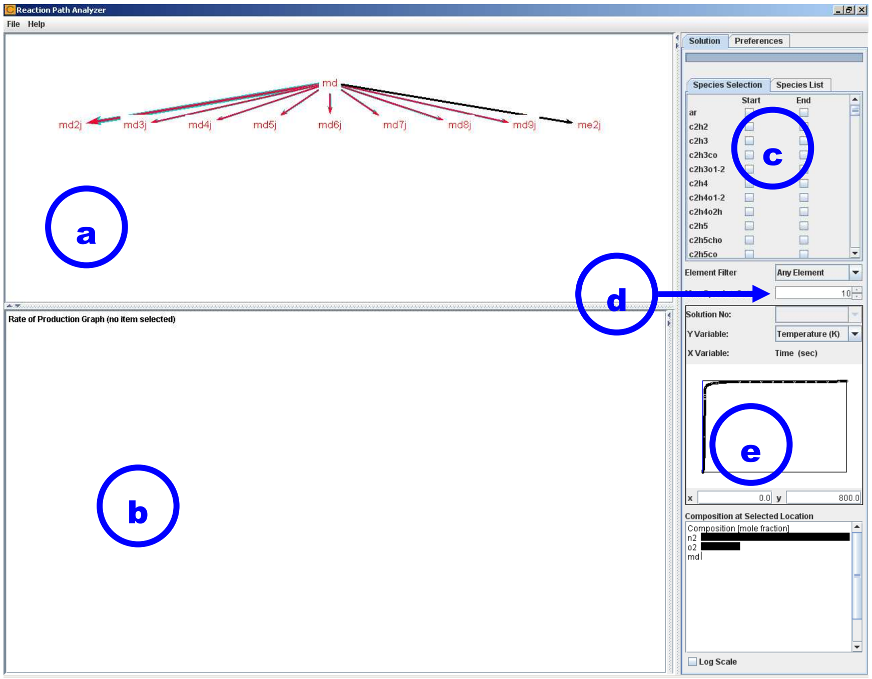

Element Filter: Any Element

10

Solution No:

Y Variable: Temperature (K)

X Variable: Time (sec)

x 0.0 y 800.0

Figure B-9: The Analyze Reaction Pathways window in CHEMKIN Pro

The five main elements of interest are described as follows:

a. Reaction Path Diagram: shows the connection of species of interest
b. Rate of Production (ROP): displays ROP for species highlighted in the diagram window
c. Species Selection: choose the beginning and ending species in the diagram window
d. Max Species Count: limit/expand the number of species shown in the diagram window
e. Data Point Display Graph: shows the reaction history and allows users to choose a different point to view in the diagram window

On the Display Graph, choose a time or temperature closer to ignition by clicking on the graph itself, or entering a new time/temperature in the boxes below. The Reaction Path Diagram will change accordingly. Then highlight (click on) the fuel species in the Reaction Path Diagram window to display its Rate of Production information at the bottom of the page. As seen in Figure B-10, the ROP section becomes a bar graph showing the consumption and production of the fuel species, with all of the reactions related to the fuel shown to the left.

The first 10 reactions (with pink bars) listed in Figure B-10 are reactions of the isomers of the fuel MD. It is seen that many of them have identical ROP values and one species is clearly the dominant pathway. This species should be kept. The user can then test removing several of the other isomers by commenting them out in the mechanism (*mech.dat* file). To start, one isomer should be kept from each group of identical ROP values.

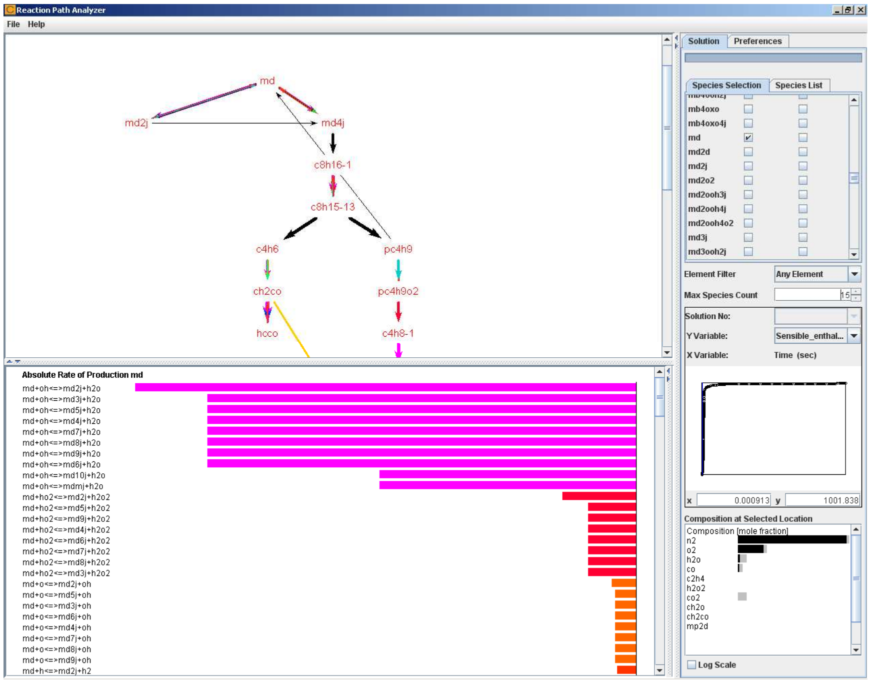

Absolute Rate of Production md

```
md+oh<=>md2j+h2o
md+oh<=>md3j+h2o
md+oh<=>md5j+h2o
md+oh<=>md4j+h2o
md+oh<=>md7j+h2o
md+oh<=>md8j+h2o
md+oh<=>md9j+h2o
md+oh<=>md6j+h2o
md+oh<=>md10j+h2o
md+oh<=>mdmj+h2o
md+ho2<=>md2j+h2o2
md+ho2<=>md5j+h2o2
md+ho2<=>md9j+h2o2
md+ho2<=>md4j+h2o2
md+ho2<=>md6j+h2o2
md+ho2<=>md7j+h2o2
md+ho2<=>md8j+h2o2
md+ho2<=>md3j+h2o2
md+o<=>md2j+oh
md+o<=>md5j+oh
md+o<=>md3j+oh
md+o<=>md6j+oh
md+o<=>md4j+oh
md+o<=>md7j+oh
md+o<=>md8j+oh
md+o<=>md9j+oh
md+h<=>md2j+h2
```

Element Filter: Any Element
Max Species Count: 15
Solution No:
Y Variable: Sensible_enthal...
X Variable: Time (sec)
x 0.000913 y 1001.838
Composition [mole fraction]

Figure B-10: Rate of production analysis using CHEMKIN Pro

When the isomers are commented, the ignition delay comparison should be repeated over a range of conditions to ensure there are no major changes with the isomer removal. If the user is satisfied, the DRG process can be repeated with this new mechanism as the “detailed” mechanism. This will eliminate many of the intermediate species that were once connected by the removed isomers. This process of removing isomers, checking ignition delay, and rerunning DRG can be repeated until a mechanism of desired size or accuracy is found.

B.8.3 *Reformatting the Mechanism*

Most mechanisms, particularly those developed by Lawrence Livermore National Lab (LLNL), have a very consistent structure. Henry Curran, who developed one of the first detailed n-heptane mechanisms, identified 25 reaction classes. That mechanism, along with many others and their respective papers, can be found on the LLNL website:

https://www-pls.llnl.gov/?url=science_and_technology-chemistry-combustion-mechanisms

It is advisable to rearrange the mechanism and group the reactions into these classes. It will be easier to see the reaction flow from fuel-decomposition to lower-level intermediate species. It may also be helpful in identifying other redundant species (non-isomers) that can be removed. An unlimited amount of comments can be included in the *mech.dat* file to make it clearer. Use a “!” to make a comment.

B.8.4 *Reaction Rate Constant Adjustments*

Removing a significant amount of species and reactions from a mechanism can change the ignition delay time and species histories. Reduced mechanisms have the advantage of being “engineering tools” and it is understood that there is some degree of estimation. We are able to adjust rate constants for some reactions to account for the removed species/reactions. This section describes a strategic method for identifying key reactions and adjusting reaction rates.

Early work of Charles Westbrook, in the paper ***Chemical Kinetics of Hydrocarbon Ignition in Practical Combustion Systems***, outlined important reactions for low-, intermediate-, and high-temperature combustion kinetics.

High Temperatures (>1200K)
H + O2 = O + OH

Intermediate Temperatures (850K>T>1200K)
H + O2 + M = HO2 + M
RH + HO2 = R + H2O2
H2O2 + M = OH + OH + M

Low Temperature (<850K)
R + O2 + M = RO2 + M
RO2 = QOOH
QOOH = Q + HO2
QOOH = QO + OH
QOOH + O2 = O2QOOH

Reactions for lower-level carbon species (C_3 and lower) and the H-O species should not be adjusted. These sub-mechanisms have been widely validated. Rate constants related to the fuel of interest are open for adjustment. The reactions listed above from Westbrook are a good start, but there are several other options. Also, it is important establish a systematic way to identify and adjust reactions.

CHEMKIN uses an Arrhenius expression to determine the forward rate constant, $k_{f,i}$. In Equation 1, A_i is the pre-exponential factor, b_i is the temperature exponent, and E_i is the activation energy for the i^{th} reaction. The variables T and R_c are the temperature and universal gas constant, respectively.

$$k_{f,i} = A_i T^{b_i} e^{\frac{-E_i}{R_c T}} \tag{B-2}$$

The three parameters, A, b, and E, are given in the *mech.dat* file. The pre-exponential factor, A, is directly related to the rate constant, and increasing A will increase the reaction rate equally over the entire temperature range. Figure B-11(a) shows the effect of increasing and decreasing A by an order of magnitude. The activation energy, E, is essentially an energy barrier, and is therefore negative in the Arrhenius expression. It is also temperature dependent. As a result, changes to E, indirectly effect the rate constant, and change the slope of the curve so that its effect is greater under different temperature conditions. Figure B-11(b) shows the effect of increasing and decreasing the activation energy by 20%. Note that the reaction rate is increased/decreased by over an order of magnitude at 500K, and less at high temperatures.

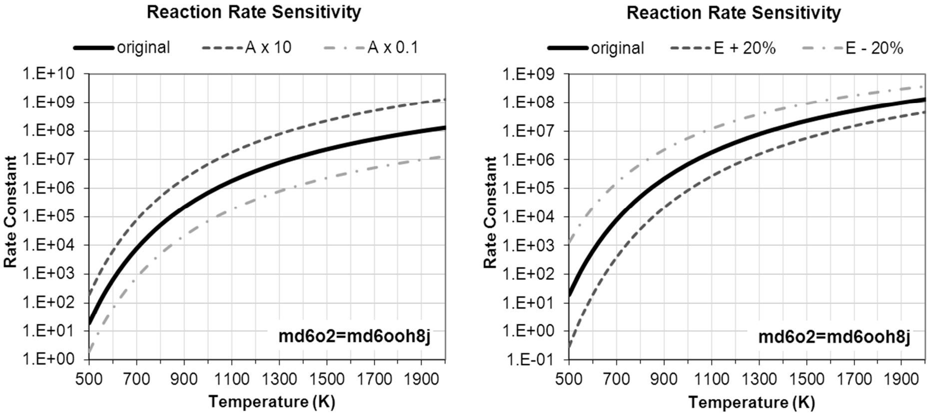

(a) (b)

Figure B-11: Effect of adjusting the (a) pre-exponential factor and (b) activation energy rate parameters.

To assess the sensitivity of a given reaction, six rate adjustments will be made according to Table 1. Figure B-12 displays how the rate constant of an example reaction is affected by these adjustments. The pre-exponential factor is doubled and halved and Figure B-12(a) shows that the entire rate constant shifts up and down equally. The activation energy is increased and decreased by 20% in Figure B-12(b) and (c), respectively. For activation energy adjustments, the two extreme values of A (matching the original rate constant at the 500K and 2000K temperature points) provide suggested limits for the pre-exponential value. These limits allow some change to the rate constant slope, but keep the rate constant within about an order of magnitude of its original value. Any value of A can be used within these two limits. In general, there is less confidence in the pre-exponential factor value, and therefore a larger range of adjustment is allowed.

Table B-1: Rate parameter adjustments for rate constant sensitivity analysis

	Pre-Exponential (A)	**Activation Energy (E)**
a	x 2.0	-
b	x 0.5	-
c	adjust to match base at 2000K	x 1.2
d	adjust to match base at 500K	x 1.2
e	adjust to match base at 2000K	x 0.8
f	adjust to match base at 500K	x 0.8

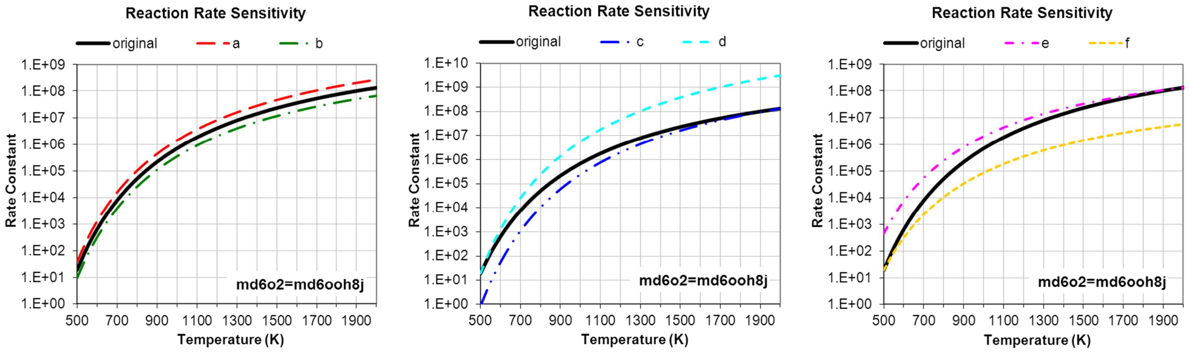

(a) (b) (c)

Figure B-12: Effect of reaction rate parameter adjustments from Table 1

The Excel file *ReactionRateSensitivity.xlsx* (found in the ***SourceCode*** directory) is set-up to automatically calculate new reaction rate parameter values to assess the sensitivity of a given reaction. Simply copy/paste the reaction rate parameters into the *RateSensitivity* tab and copy the new parameter values into the *mech.dat* file. Then, rename the mech.dat file according to the adjustment made (e.g., *mech-a.dat*) and repeat the process for the other adjustments.

Once all of the adjusted mech.dat files are created, the sensitivity batch file (*batchSENS-af*) can be used to create ignition delay plots that show the effect of the parameter adjustments. Note that some reactions have very small or zero activation energy values. In these cases, only the “a” and “b” adjustments to the pre-exponential factor need to be performed.

Directories are already set-up in the ***IgnitionDelay*** directory. Copy the following *mech.dat* files to the ***Mech*** folder in the *IgnitionDelay* directory.

- original reduced mechanism file (no adjustments): renamed *mech-1.dat*
- six adjusted mechanism files: renamed *mech-a.dat* to *mech-f.dat*

Change the batch files, as mentioned previously, to account for the new fuel/conditions of interest. Then submit *batchSENS-af* (or *batchSENS-ab* if the reaction of interest has E=0). Figure B-13 shows an example plot of the sensitivity of tested reaction rate constant parameters. It can be seen that this particular reaction is very important for low temperatures. Repeat this process for several other reactions to identify which rate parameters should be adjusted, and how much to adjust them to achieve the desired ignition delay time.

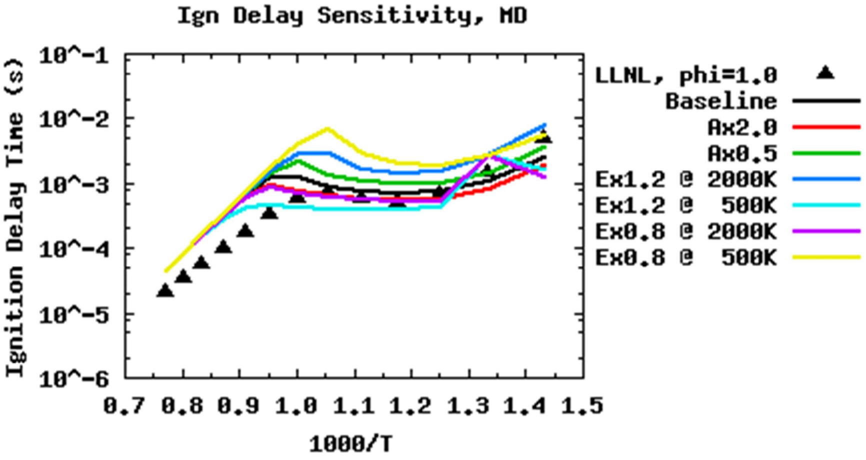

Figure B-13: Example ignition delay curve showing reaction rate parameter sensitivity according to the adjustments shown in Table 1.

Appendix C: Gasjet Inconsistencies

This appendix is dedicated to the inconsistencies observed using the Gasjet model. This model was applied throughout this work and only later found to cause excessive vaporization. The conclusions made throughout the previous analysis do not change, however, different input conditions are required to overcome the decreased vaporization. In the cases that were repeated, the simulations with the Gasjet model turned off produced results that were closer to expectations. Particularly with respect to fuel impingement in the LTC cases using the GM engine.

The in-cylinder images shown previously did not indicate any fuel on the piston. However, once the Gasjet model was turned off, a notable amount of fuel impingement occurred. Figure C-1 shows in-cylinder spray images for the SOI timing of -30^{o} aTDC. Vaporization was very poor from the wall, as seen in Figure C-2, and fuel remained on the piston into the expansion stroke for both SME100 and diesel fuel. It should be noted that the experiments reported that a film developed in the combustion chamber throughout the runs with the SME100 fuel, requiring that the chamber be cleaned. This suggests that a notable amount of impingement was occurring.

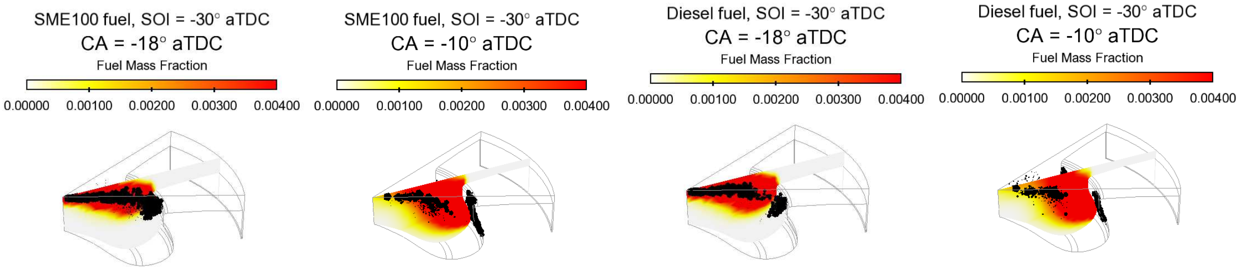

(a) (b)

Figure C-1: In-cylinder depiction of fuel impingement for (a) SME100 and (b) diesel fuels at the -30^o aTDC SOI timing condition

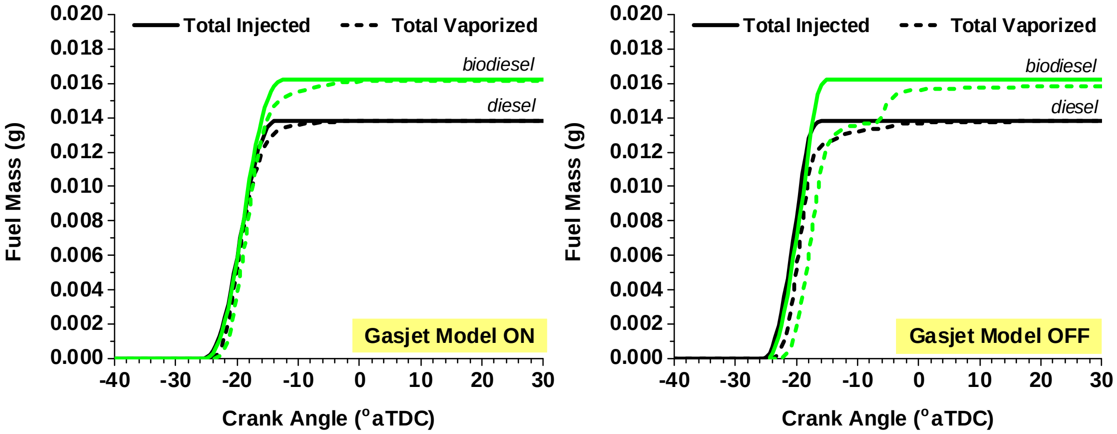

Figure C-2: Fuel vaporization from the -30^o aTDC SOI timing with (a) Gasjet model on and (b) Gasjet model off

The same SOI timing case was repeated with chemistry turned off to investigate the spray. While the problem is exaggerated for the biodiesel, the issue is not restricted to the multi-component model. The same effect is seen for single-component diesel fuel as well. Figure C-3 compares the effect of the Gasjet model on injection characteristics. For each fuel, the total number of parcels remains low when the Gasjet model is used, and the parcels are very small (below 2 μm) for each fuel. These small parcels vaporize quickly, which results in decreased liquid penetration.

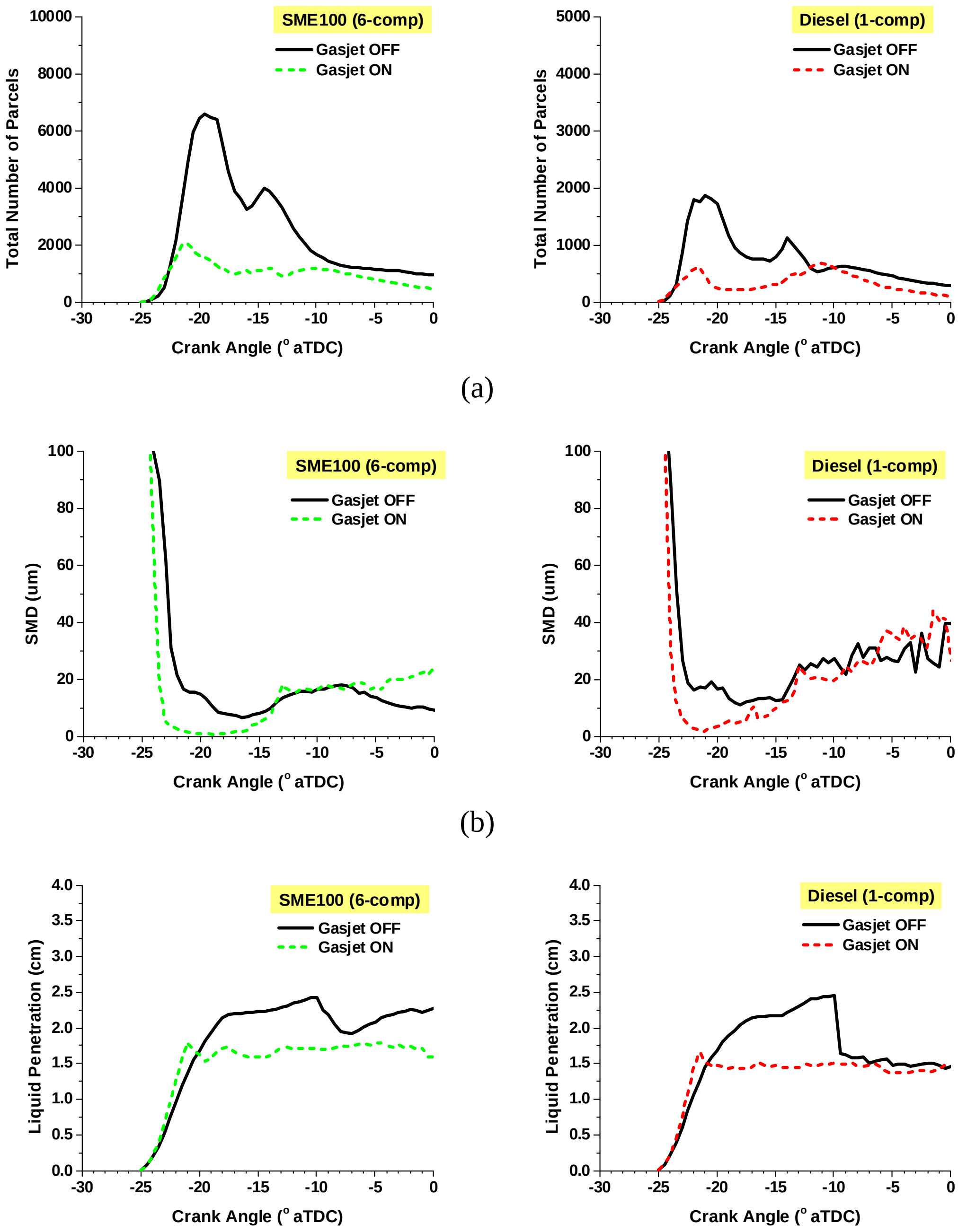

(a)

(b)

(c)

Figure C-3: Effect of Gasjet model on (a) fuel parcel count, (b) parcel SMD, (c) and liquid penetration for non-reacting injections into the GM engine for SME100 and diesel fuels

When the Gasjet model was turned off, a new set of input conditions was required for both fuels in order to reproduce the ignition and performance of the experiments. The new inputs for diesel and SME100 are listed in Table C-1 and Table C-2, respectively. The most notable difference is in the EGR %. The simulations with Gasjet on required high EGR to reduce the reactivity of the excessively vaporized fuels. When Gasjet is turned off, less EGR is needed. It should be noted, however, that the biodiesel cases required much more O_2 (lower EGR) in order to improve the reactivity and overcome the much decreased vaporization. The emissions and fuel consumption results did not significantly change with these new conditions.

Table C-1: Initial conditions for diesel LTC SOI timings with Gasjet model turned off

SOI Timing (° aTDC)	IVC Pressure (bar)	IVC Temperature (K)	EGR Percent %
-36	1.919	360	73
-34	1.915	360	70
-32	1.909	360	69
-30	1.912	360	69
-28	1.917	360	69
-26	1.918	355	70
-24	1.909	360	70
-22	1.909	355	70

Table C-2: Initial conditions for SME100 LTC SOI timings with Gasjet model turned off

SOI Timing (° aTDC)	IVC Pressure (bar)	IVC Temperature (K)	EGR Percent %
-36	1.918	370	68
-34	1.926	360	66
-32	1.933	360	63
-30	1.920	360	62
-28	1.922	360	62
-26	1.922	360	63
-24	1.918	365	64
-22	1.930	365	64

It was later noted that the standard Gasjet constants were used in the GM engine cases, including a “dismax” value of 2.25. The dismax constant specifies the distance (in cm) that the Gasjet model is applied and it should not exceed the distance that the spray would travel from the nozzle to the bowl. Since the bowl radius is only slightly longer than 2.25 cm, a smaller value of 1.0 cm was applied to see if this would improve some of the Gasjet inconsistencies described previously. Figure C-4 compares the fuel penetration predictions using the two dismax values. The shorter value does improve the penetration, allowing some fuel to hit the piston bowl as expected.

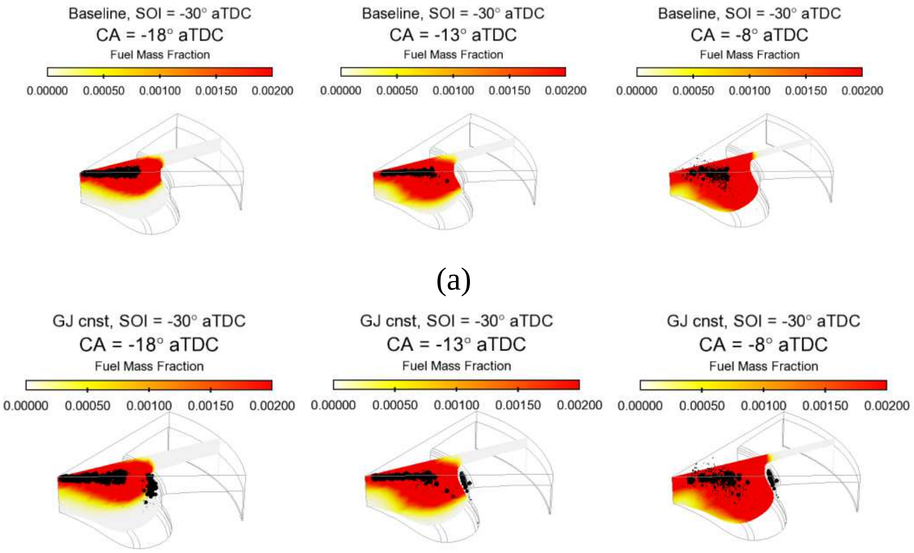

(b)

Figure C-4: In-cylinder fuel penetration predictions for the -30^{o} aTDC SOI timing for SME100 fuel (a) using the standard Gasjet constants and (b) reducing the *dismax* constant from 2.25 to 1.0

As shown in below, the injection characteristics were improved by providing a more appropriate dismax parameter. The parcel diameter (as SMD) is still excessively small at early crank angles, but the number of parcels and liquid penetration are closer to the predictions of simulations with the Gasjet model off.

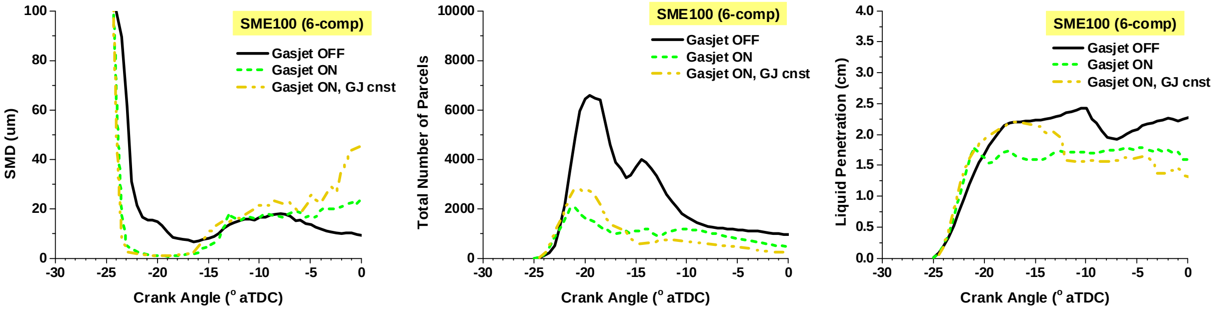

(a) (b) (c)

Figure C-5: Effect of decreased Gasjet model constant *dismax* on (a) fuel parcel count, (b) parcel SMD, (c) and liquid penetration for non-reacting injections into the GM engine for SME100 and diesel fuels

These improvements only apply to the injection, however. The combustion performance was not changed with the new dismax, as shown in Figure C-6. As such, the SOI timing sweep was not repeated with Gasjet on and the new GJ constant. However, future simulations should include this more appropriate value. Additionally, the drastic reduction in parcel diameter caused by the use of the Gasjet model should be investigated.

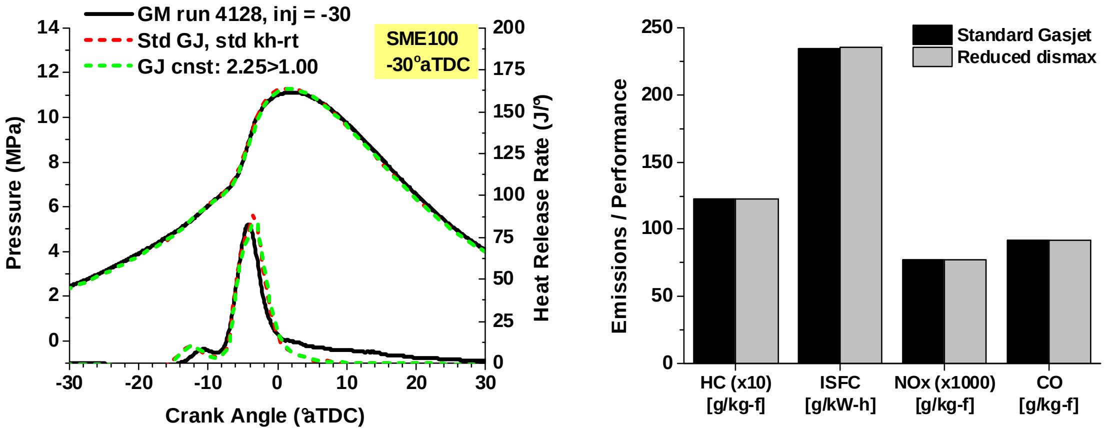

Figure C-6: Comparison of (a) pressure and heat release rate and (b) emissions and fuel consumption for -30^o aTDC SOI timing using the standard Gasjet constants and a reduced *dismax*

Appendix D: ERC-MultiChem+Bio Mechanism

```
!Combination of ERC-MultiChem and reduced MD/MD9D mechanism
!2012 PhD thesis, Jessica L. Brakora
!University of Wisconsin-Madison

elements
 h   c    o   n
end

species

!-main fuel species--------------------------------------------------
nc7h16

!-common KIVA species------------------------------------------------
         o2        n2        co2       h2o
co       h2        oh        h2o2      ho2
h        o         ch3o      ch2o      hco
ch2      ch3       ch4       c2h2      c2h3
c2h4     c2h5      c3h4      c3h5      c3h6
c3h7

!-nheptane species---------------------------------------------------
c7h15-2   c7h15o2   c7ket12   c5h11co

!-isooctane species--------------------------------------------------
!jlb ic8h18
!jlb c8h17     c8h17oo   ic8ket21  c6h13co
!jlb c4h9

!-soot model complimentary-------------------------------------------
c2h6

!-toluene species----------------------------------------------------
!jlb toluene
!jlb c4h4      c6h6      c4h6      c4h3
!jlb c5h4o    c6h5oh    oc6h4o    c6h5cho
!jlb hcco      c4h5      c6h5      c5h5      c5h3o
!jlb c5h5o    c5h4oh    c6h5o    c6h4oh    benzyl
!jlb oc6h4ch3

!-cyclo-hexane species-----------------------------------------------
!jlb chx       chxrad      chxro2     chxro
!jlb ochxrro   oc5h8cho    choco       chxdooh   chxdo
!jlb hooc5h8cho  cyc6h9     cyc6h8   c6h11   c4h6ooh
!jlb c2h3cho   c3h6cho   cychexene

!-ethanol species----------------------------------------------------
!jlb c2h5oh   ch3choh   ch3ch2o   ch3cho
```

```
!-dme species--------------------------------------------------------
!jlb ch3och3  ch3och2    ch3och2o2  ch3och2o  ho2ch2ocho
!jlb hoch2o    hco2h     hco2

!-prf+mb species-----------------------------------------------------
!jlb ch2cho   ch2co   ch3o2    ch3o2h

!-mb species---------------------------------------------------------
ch2cho   ch2co   ch3oco   c2h3co
!jlb ch3oco   c2h5cho  c2h3co
!jlb mb        mb2j       mb2o       mb2oo
!jlb mb2ooh4j  me2*o    me2j*o
!jlb mp2d      mp3j2*o

!-c14 pathways species-----------------------------------------------
!jlb c14h30  c14h29  c14h29o2  c14ket12  c12h25co
!jlb c5h10 c4h7 c4h7o  ch3co
!jlb c12h25  c12h23

!-soot species-------------------------------------------------------
!soot c7h8 c10h22 c12h26 c16h34 c18h38

!-md+md9d (biodiesel) species----------------------------------------
!-- md species  --
 md
 md6j   md6o2   md6ooh8j   mdket68   c2h5cho c6h12-1  c8h17-1

!-- md9d species --
 md9d
 md9d6j md9d6o2 md9d6ooh8j md9dket68 c2h3cho c6h10-15 ms6d

!-- common biodiesel species --
 mf5j  mf5o2  mf5ooh3j  mfket53  mp3oxo
 ms6oxo7j  mb4j  me2j

!-- generic biodiesel species for DMC --
 mpalm  mstear  molea  mlinl  mlinln  nc7bio

!-emissions species--------------------------------------------------
n         n2o       no        no2
nox
soot
end
```

```
reactions
!====================================================================
! octane reactions
!====================================================================
! #1
!jlb ic8h18+h=c8h17+h2                     4.380e+07  2.0    7760.0
! #2
!jlb ic8h18+oh=c8h17+h2o                   3.471E+07  1.8     278.2
! #3
!jlb ic8h18+ho2=c8h17+h2o2                 2.228e+14  0.0   18950.0
! #4
!jlb ic8h18+o2=c8h17+ho2                   2.219e+15  0.0   42904.0
! #5
!jlb c8h17+o2=c8h17oo                      1.053e+11  0.0       0.0
! #6
!jlb c8h17oo+o2=ic8ket21+oh                1.740E+16  0.0   21233.0
! #7
!jlb ic8ket21=ch2o+c6h13co+oh              1.784e+14  0.0   39100.0
! #8
!jlb c6h13co=c4h9+c2h4+co                  4.920E+16  0.0   40200.0
! #9
!jlb c4h9=c3h6+ch3                         4.560e+13  0.0   36900.0
! #10
!jlb c8h17=c3h7+c2h4+c3h6                  2.161E+16  0.0   36600.0
! #11
!c8h17=c2h5+c3h5+c3h7                      1.409E+16  0.0   36600.0

!- connect fuels ----------------------------------------------------
!jlb ic8h18+c7h15-2=nc7h16+c8h17           5.012e+10  0.0       0.0
!--------------------------------------------------------------------

!====================================================================
! heptane reactions
!====================================================================
!#1
 nc7h16+h=c7h15-2+h2                       4.380e+07  2.0    4760.0
!nhep/diesel
!#2
! nc7h16+oh=c7h15-2+h2o                     0.478e+10  1.3     690.0 !nhep
 nc7h16+oh=c7h15-2+h2o                     1.355e+10  1.3     690.0
!diesel
!#3
! nc7h16+ho2=c7h15-2+h2o2                   1.220e+14  0.0   16950.0 !nhep
 nc7h16+ho2=c7h15-2+h2o2                   3.300e+14  0.0   16950.0
!diesel
!#4
! nc7h16+o2=c7h15-2+ho2                     0.706e+14  0.0   37904.0 !nhep
 nc7h16+o2=c7h15-2+ho2                     1.250e+14  0.0   37904.0
!diesel
!#5
```

```
 c7h15-2+o2=c7h15o2                        2.340e+12  0.0       0.0
!nhep/diesel
!#6
! c7h15o2+o2=c7ket12+oh                     1.535E+14  0.0   18232.712
!nhep
 c7h15o2+o2=c7ket12+oh                     3.290E+14  0.0   18232.712
!diesel
!#7
! c7ket12=c5h11co+ch2o+oh                   9.008e+14  0.0   4.110e+4
!nhep
 c7ket12=c5h11co+ch2o+oh                   6.005e+14  0.0   4.110e+4
!diesel
!#8
 c5h11co=c2h4+c3h7+co                      9.840E+15  0.0   4.02E+04
!nhep/diesel
!#9
! c7h15-2=c2h5+c2h4+c3h6                    1.648E+15  0.0   3.46E+04
!nhep
 c7h15-2=c2h5+c2h4+c3h6                    4.038E+15  0.0   3.46E+04
!diesel

!====================================================================
! lower-level reactions
!====================================================================
 c3h7=c2h4+ch3                             9.600e+13  0.0   30950.0
 c3h7=c3h6+h                               1.250e+14  0.0   36900.0
 c3h6+ch3=c3h5+ch4                         9.000e+11  0.0    8480.0
 c3h5+o2=c3h4+ho2                          9.49E+29   -5.6    15540.0
!-- added to PRF ----------------------------------------------------
 c3h5+o2=c2h2+ch2o+oh                      9.720E+29  -5.71  2.145E+04
   rev /  0.000E+00  0.00  0.000E+00 /
 c3h5+o2=ch2cho+ch2o                       7.140E+15  -1.21  2.105E+04
   rev /  4.944E+16  -1.40  8.862E+04 /
 c3h5+o2=ch3+hco+hco                       1.00E+12    0.0    22150.0
 c3h5+ho2=c2h3+ch2o+oh                     2.028E+12  0.09  2.356E+04
 c3h5+h=c3h4+h2                            1.232E+03 3.035 2.582E+03
   rev/ 2.818E+00 3.784 4.722E+04 /
!--------------------------------------------------------------------
 c3h4+oh=c2h3+ch2o                         1.000e+12  0.0       0.0
 c3h4+oh=c2h4+hco                          1.000e+12  0.0       0.0
!-- added to PRF ----------------------------------------------------
 c3h4+o=c2h2+ch2o                          3.00E-03    4.6    -4243.0
   rev /2.32E+02    3.2    81190.0/
 c3h4+o=c2h3+hco                           3.20E+12    0.0     2010.0
   rev /2.55E+12   -0.4    32350.0/
 c3h4+ho2=c2h4+co+oh                       3.00E+12    0.0    19000.0
 c3h4+oh=c2h2+hco+h2                       7.07E+06    1.75    1000.0
 c3h4+o2=ch2co+hco+h                       1.50E+09    0.0     2870.0
!--------------------------------------------------------------------
 ch3+ho2=ch3o+oh                           5.000e+13  0.00      0.
```

```
 ch3+oh=ch2+h2o                            7.500e+06  2.00   5000.
 ch2+oh=ch2o+h                             2.500e+13  0.00      0.
 ch2+o2=hco+oh                             4.300e+10  0.00   -500.
 ch2+o2=co2+h2                             6.900e+11  0.00    500.
 ch2+o2=co+h2o                             2.000e+10  0.00  -1000.
 ch2+o2=ch2o+o                             5.000e+13  0.00   9000.
 ch2+o2=co2+h+h                            1.600e+12  0.00   1000.
 ch2+o2=co+oh+h                            8.600e+10  0.00   -500.
 ch3o+co=ch3+co2                           3.925e+13  0.00  11800.
 co+oh=co2+h                               0.474e+07  1.30   -758.
 o+co(+m)=co2(+m)                          1.800e+10  .000   2385.00 !gri
mech 3
   low/ 6.020e+14     .000    3000.00/
   h2/2.00/ o2/6.00/ h2o/6.00/ co/1.50/ co2/3.50/
 o2+co=o+co2                               2.500e+12  0.000 47800.00 !gri
mech
 ho2+co=oh+co2                             4.760e+13  0.000 23600.00 !gri
mech 1.5e14
 o+oh=o2+h                                 4.000e+14 -0.50      0.
 h+ho2=oh+oh                               1.700e+14  0.0     875.
 oh+oh=o+h2o                               6.000e+08  1.30      0.
 h+o2(+m)=ho2(+m)                          1.475E+12 0.60  0.000E+00
   low/3.500e+16 -4.10E-01 -1.1160E+03 /
   troe/5.0000E-01  1.0000E-30  1.0000E+30/
   h2/2/ h2o/12/ co/1.9/ co2/3.8/
 oh+oh(+m)=h2o2(+m)                        1.236E+14   -.37  0.000E+00
   low /3.041E+30 -4.63 2049./
   troe /0.47 100. 2000. 1.0e+15/
   h2/2/ h2o/12/ co/1.9/ co2/3.8/
 h2o2+h=ho2+h2                             1.98e+06    2.0      2435.0
!marinov 1995a
 h2o2+h=oh+h2o                             3.07e+13    0.0      4217.0
!marinov 1995a
 h2o2+o=oh+ho2                             9.55e+06    2.0      3970.0
!marinov 1995a
 h2o2+oh=h2o+ho2                           2.40e+00    4.042   -2162.0
!marinov 1995a
 h2+oh=h2o+h                               1.170e+09  1.30   3626.
 ho2+ho2=h2o2+o2                           3.000e+12  0.00      0.
 ch2o+oh=hco+h2o                           5.563e+10  1.095 -76.517
 ch2o+ho2=hco+h2o2                         3.000e+12  0.00   8000.
 hco+o2=ho2+co                             3.300e+13 -0.40      0.
 hco+m=h+co+m                              1.591E+18  0.95  56712.329
 ch3+ch3o=ch4+ch2o                         4.300e+13  0.00      0.
 c2h4+oh=ch2o+ch3                          7.59e+12  0.0     960.
 c2h4+oh=c2h3+h2o                          8.020e+13  0.00   5955.
!-- added to PRF ----------------------------------------------------
 c2h4+o2=c2h3+ho2                          4.000e+13 0.000 4.820e+04
 c2h4+o=ch3+hco                            8.564e+06 1.880 1.830e+02
 c2h4+h=c2h3+h2                            5.070e+07 1.930 1.295e+04
```

```
 c2h4(+m)=c2h2+h2(+m)                       8.000e+12 0.440 7.777e+04
   low / 1.5800e+51 -9.3000e+00 9.7800e+04 /
   troe / 7.3500e-01 1.8000e+02 1.0350e+03 5.4170e+03 / !Troe Fall-off
reaction
   h2/2/ h2o/6/ co/1.5/ co2/2/ ch4/2/ c2h6/3/
!---------------------------------------------------------------------
 c2h3+o2=ch2o+hco                           4.000e+12  0.00   -250.
 c2h3+hco=c2h4+co                           6.034e+13  0.0       0.
 c2h5+o2=c2h4+ho2                          15.000E+10  0.00  3.000E+03
!-- added to PRF -----------------------------------------------------
 c2h5+o2=ch3+co+h2o                         3.000E+12 0.00 2.066E+04
 c2h5+o2=ch3+hco+oh                         3.63E+13    0.0    37200.0
 ch3+c2h5=ch4+c2h4                          1.180e+04 2.450 -2.921e+03
   rev/ 2.390e+06 2.400 6.669e+04 /
 c2h5+h=ch3+ch3                             9.690e+13 0.000 2.200e+02
   rev/ 2.029e+09 1.028 1.051e+04 /
 c2h5+h=c2h4+h2                             2.000e+12 0.000 0.000e+00
   rev/ 4.440e+11 0.396 6.807e+04 /
 c2h5+o=ch3+hco+h                           1.100e+14 0.000 0.000e+00
!---------------------------------------------------------------------
 ch4+o2=ch3+ho2                             2.02E+07   2.1   53210.0
 oh+ho2=h2o+o2                              7.50E+12   0.0       0.
 ch3+o2=ch2o+oh                             3.80E+11   0.0    9000.
 ch4+h=ch3+h2                               6.600e+08  1.60  10840.
 ch4+oh=ch3+h2o                             5.830e+04  2.6    2190.0
 ch4+o=ch3+oh                               1.020e+09  1.50   8604.
 ch4+ho2=ch3+h2o2                           1.130e+01  3.7   21010.0
 ch4+ch2=ch3+ch3                            2.460e+06  2.0    8270.0
 c3h6=c2h3+ch3                              3.150e+15  0.0   85500.0
 ch2+ch2=c2h2+h2                            1.200e+13  0.0     800. !with
c2h2
 ch2+ch2=c2h2+h+h                           1.200e+14  0.0     800.
 c2h2+o2=hco+hco                            4.000e+12  0.00  28000.
 c2h2+o=ch2+co                              1.020e+07  2.00   1900.
 c2h3+m=c2h2+h+m                            2.289e+12 0.023 3.672e+04
 c2h3+h=c2h2+h2                             4.000e+13  0.00      0.
 c2h3+oh=c2h2+h2o                           3.000e+13  0.00      0.
 c2h3+ch2=c2h2+ch3                          3.000e+13  0.00      0.
 c2h3+c2h3=c2h2+c2h4                        1.450e+13  0.0       0.0
 c2h3+o=c2h2+oh                             1.000e+13  0.0       0.0
 c2h2+oh=ch3+co                             4.830e-04  4.00  -2000.

!=====================================================================
! NOx reactions (from GRI-Mech)
!=====================================================================
 n+no=n2+o                                  3.500e+13  0.00    330.0
 n+o2=no+o                                  2.650e+12  0.00   6400.0
 n+oh=no+h                                  7.333e+13  0.00   1120.0
 n2o+o=n2+o2                                1.400e+12  0.00  10810.0
 n2o+o=2no                                  2.900e+13  0.00  23150.0
```

```
 n2o+h=n2+oh                              4.400e+14  0.00  18880.0
 n2o+oh=n2+ho2                            2.000e+12  0.00  21060.0
 n2o(+m)=n2+o(+m)                         1.300e+11  0.00  59620.0
   low  /  6.200e+14     .000  56100.00/
   h2/2.00/ h2o/6.00/ ch4/2.00/ co/1.50/ co2/2.00/
 ho2+no=no2+oh                            2.110e+12  0.00   -480.0
 no+o+m=no2+m                             1.060e+20 -1.410     0.0
   h2/2.00/ h2o/6.00/ ch4/2.00/ co/1.50/ co2/2.00/
 no2+o=no+o2                              3.900e+12  0.00   -240.0
 no2+h=no+oh                              1.320e+14  0.00    360.0

!====================================================================
! lower-level reactions (cont.)
!====================================================================
 c3h6+h=c3h5+h2                           5.000e+12  0.0    1500.0! 40
 c3h6+o2=c3h5+ho2                         4.000e+12  0.0   39900.0! 42
!-- added to PRF ---------------------------------------------------
 c3h6+oh=c3h5+h2o                         3.120E+06  2.00 -2.980E+02
   rev /  6.194E+06  2.01  3.188E+04 /
 c3h6+o=c2h5+hco                          1.580E+07  1.76 -1.216E+03
   rev /  1.402E+05  1.88  2.651E+04 /
 c3h6+ho2=c3h5+h2o2                       1.500E+11  0.00  1.419E+04
   rev /  5.867E+05  1.33  9.759E+03 /
 c3h6+o=c3h5+oh                           5.240e+11 0.700 5.884e+03
   rev/ 1.104e+11 0.697 2.015e+04 /
!--------------------------------------------------------------------
 ch2cho+h=ch3+hco                         2.200e+13  0.0       0.0
! ch3o (+m)=ch2o+h (+m)                    5.000e+11  0.00  27420.0! 74
 ch3o (+m)=ch2o+h (+m)                    5.000e+09  0.00  27420.0! 74
!jlb
   low /2.344e+25 -2.7  3.060e+04/
 ch2o+o2=hco+ho2                          6.200e+13  0.00  39000. !139
 ch2o+o=hco+oh                            4.100e+11  0.57   2760. !140
 ch2o+h=hco+h2                            2.190e+08  1.80   3000. !141
 ch2o+m=co+h2+m                           6.250e+15  0.00  69540. !144
 ch2o+m=hco+h+m                           3.300e+16  0.00  81000. !145
 hco+oh=h2o+co                            1.000e+14  0.00      0. !147
 hco+o=oh+co                              3.000e+13  0.00      0. !149
 hco+o=h+co2                              3.000e+13  0.00      0. !150
 hco+ho2=co2+oh+h                         3.000e+13  0.00      0. !153

!====================================================================
! soot model complimentary
!====================================================================
 c2h6+ch3=c2h5+ch4                        1.510E-07  6.00  6.047E+03
   rev /  9.649E-10  6.56  1.022E+04 /
 c2h6+h=c2h5+h2                           5.370E+02  3.50  5.200E+03
   rev /  9.720E+02  3.50  2.732E+04 /
 c2h6+oh=c2h5+h2o                         5.125E+06  2.06  8.550E+02
   rev /  1.010E+07  2.06  2.298E+04 /
```

```
 c2h6+o=c2h5+oh                            1.130E+14  0.00  7.850E+03
   rev /  2.080E+13  0.00  1.272E+04 /
 ch3+ch3(+m)=c2h6(+m)                      7.371E+16 -1.17  6.358E+02
   low/9.088E+35 -5.246  1.705E+03/
   troe/0.405 1120. 69.6 1.e+15/
 c2h6+o2=c2h5+ho2                          4.000E+13  0.00  5.090E+04
   rev /  3.000E+11  0.00  0.000E+00 /
 c2h6+ho2=c2h5+h2o2                        1.700E+13  0.00  2.046E+04
   rev /  1.069E+11  0.24  7.842E+03 /
 c2h6+c2h4=c2h5+c2h5                       5.000E+11  0.00  6.000E+04
   rev /  5.000E+11  0.00  0.000E+00 /
 c2h6+m=c2h5+h+m                           8.851E+20 -1.22  1.022E+05
   rev /  1.148E+13  0.34 -1.550E+03 /
 c2h6+ch2=c2h5+ch3                         2.200E+13  0.00  8.670E+03
   rev /  2.665E+10  0.56  1.706E+04 /
!jlb  c2h6+ch3o2=c2h5+ch3o2h                 1.700E+13  0.00  2.046E+04
!jlb   rev /  7.500E+11  0.00  1.280E+03 /
 c3h6+c2h5=c3h5+c2h6                       1.000E+11  0.00  9.800E+03
   rev /  5.369E+05  1.33  1.644E+04 /
 c3h5+c2h5=c2h6+c3h4                       4.000E+11  0.00  0.000E+00
   rev /  1.802E+12  0.05  4.033E+04 /

!=====================================================================
! addition for MB mech
!=====================================================================
!-- ch2cho --
 c2h4+o=ch2cho+h                           3.390E+06  1.88    179.0
 c2h3+o2=ch2cho+o                          3.500E+14 -0.61   5260.0
!jlb  ch2cho+o2=ch2o+co+oh                  2.000E+13  0.00  42000.0 !jlb
*key rxn*

!-- ch2co --
 c2h2+oh=ch2co+h                           1.00e+11    0.0    12000.0
 ch2co+h=ch3+co                            1.100E+13 0.00 3.400E+03
 ch2co+o=ch2+co2                           1.750E+12 0.00 1.350E+03
 ch2co(+m)=ch2+co(+m)                      3.000E+14 0.00 7.098E+04
   low / 3.600E+15 0.00  5.927E+04 /
 c3h6+o=ch2co+ch3+h                        1.500E+07 1.76 7.600E+01
 ch2cho=ch2co+h                            3.094E+15 -0.26 5.082E+04
 ch2co+oh=ch3o+co                          6.00e+12    0.0    -1010.0

!-- ch3o2 --

!-- ch3o2h --

!-- ch3o2 to ch3o2h conversion --

!=====================================================================
! Tolune reactions
!=====================================================================
```

```
!====================================================================
! Ethanol reactions
!====================================================================

!====================================================================
! DME reactions
!====================================================================

!====================================================================
! MB reactions
!====================================================================

!-- c2h3co --
 c2h3co=c2h3+co                            2.040E+14 -0.40 3.145E+04

!-- ch3oco --
 ch3oco=ch3o+co                            7.451E+12  -1.76  1.715E+04
   rev /  1.500E+11   0.00  3.000E+03 /
 ch3oco=ch3+co2                            1.514E+12  -1.78  1.382E+04
   rev /  1.500E+11   0.00  3.673E+04 /

!-- c2h5cho --
 c2h5cho=c2h5+hco                          9.850E+18 -0.73 8.171E+04

!====================================================================
!  Cyclo-hexane oxidation reactions
!====================================================================

!-- c3h6cho --

!-- c2h3cho --
  c2h3cho+oh=c2h3+co+h2o                   9.240E+05  1.50 -9.620E+02
  c2h3cho+h=c2h3+co+h2                     1.340E+12  0.00  3.300E+03
  c2h3cho+o=c2h3+co+oh                     5.940E+11  0.00  1.868E+03
  c2h3cho+ho2=c2h3+co+h2o2                 3.010E+11  0.00  1.193E+04
  c2h3cho+ch3=c2h3+co+ch4                  2.608E+05  1.78  5.911E+03
!jlb  c2h3cho+ch3o2=c2h3+co+ch3o2h             3.010E+11  0.00  1.193E+04

!====================================================================
! cyclo-hexene to bezene
!====================================================================

!====================================================================
! MD reactions
!====================================================================

!#1
 md+h=md6j+h2                    0.1300E+07      2.4000  0.4471E+04
```

```
!#2
! md+oh=md6j+h2o                  0.4670E+08      1.6100  -.3500E+02
 md+oh=md6j+h2o                  0.1401E+07      1.6100  -.3500E+02 !0.03A

!#3
! md+ho2=md6j+h2o2                0.5880E+05      2.5000  0.1486E+05
 md+ho2=md6j+h2o2                0.1764E+04      2.5000  0.8916E+03
!0.06E@2000K

!#4
! md+o2=md6j+ho2                  0.4000E+14      0.0000  0.5016E+05
 md+o2=md6j+ho2                  0.4000E+13      0.0000  0.4013E+05
!0.8E@2000K

!#5
 md6j+o2=md6o2                   0.7540E+13      0.0000  0.0000E+00

!#6
 md6o2=md6ooh8j                  0.2500E+11      0.0000  0.2085E+05

! md6ooh8j+o2=md6ooh8o2           0.7540E+13      0.0000  0.0000E+00
! md6ooh8o2=mdket68+oh            0.1250E+11      0.0000  0.1785E+05
!-------------------------combo
 md6ooh8j+o2=mdket68+oh           0.7540E+13      0.0000  0.0000E+00 !jlb

!#7
! mdket68=mdket68o+oh             0.1050E+17      0.0000  0.4160E+05
! c2h5cho+ms6oxo7j=mdket68o       0.3330E+11      0.0000  0.6397E+04
!-----------------------------combo
 mdket68=oh+c2h5cho+ms6oxo7j     0.1050E+17      0.0000  0.4160E+05 !jlb

!#8
!c2h5cho rxn above

!#9
 c6h12-1+mb4j=md6j               0.8800E+04      2.4800  0.6130E+04
 c6h12-1=2c3h6                   0.3980E+13      0.0000  0.5763E+05
 c6h12-1=c3h5+c3h7               0.2500E+17      0.0000  0.7100E+05 !
rev LLNL


!-- extra rxns --
 md6j+h=md                       0.1000E+15      0.0000  0.0000E+00
 md+o=md6j+oh                    0.5946E+06      2.4400  0.2846E+04
 md+c2h3=md6j+c2h4               0.4000E+12      0.0000  0.1680E+05

!-- c8h17-1 --
 me2j+c8h17-1=md                 0.8000E+13      0.0000  0.0000E+00
! c2h4+c6h13-1=c8h17-1            0.8800E+04      2.4800  0.6130E+04
 c2h4+c6h12-1+h=c8h17-1          0.8800E+04      2.4800  0.6130E+04 !combo
```

```
!-- c6h13-1 --
! mb4j+c6h13-1=md                 0.8000E+13      0.0000  0.0000E+00
 mb4j+c6h12-1+h=md               0.8000E+13      0.0000  0.0000E+00 !combo

! c6h13-1+o2=c6h12-1+ho2          0.1600E+13      0.0000  0.5000E+04
! c6h12-1+h=c6h13-1               0.2500E+12      0.5100  0.2620E+04


!====================================================================
! MD9D reactions
!====================================================================

!#1
 md9d6j+h=md9d                   0.1000E+15      0.0000  0.0000E+00

!#2
! md9d+oh=md9d6j+h2o              0.4670E+08      1.6100  -.3500E+02
! md9d+oh=md9d6j+h2o              0.4670E+10      1.6100  -.3500E+02 !100A
 md9d+oh=md9d6j+h2o              0.2335E+08      1.6100  -.3500E+02 !red2:
0.5A

!#3
! md9d+ho2=md9d6j+h2o2            0.5880E+05      2.5000  0.1486E+05
 md9d+ho2=md9d6j+h2o2            0.2954E+04      2.5000  0.2972E+04 !red2:
0.2E@2000K

!#4
 md9d+o2=md9d6j+ho2              0.4000E+14      0.0000  0.5016E+05

!#5
 md9d6j+o2=md9d6o2               0.7540E+13      0.0000  0.0000E+00

!#6
 md9d6o2=md9d6ooh8j              0.1250E+11      0.0000  0.1635E+05

! md9d6ooh8j+o2=md9d6ooh8o2       0.7540E+13      0.0000  0.0000E+00
! md9d6ooh8o2=md9dket68+oh        0.1250E+11      0.0000  0.1785E+05
!----------------------------combo
 md9d6ooh8j+o2=md9dket68+oh      0.7540E+13      0.0000  0.0000E+00 !jlb

!#7
! md9dket68=oh+c2h3cho+ms6oxo7j   0.1050E+17      0.0000  0.4160E+05
 md9dket68=oh+c2h3cho+ms6oxo7j   0.2100E+13      0.0000  0.3328E+05
!0.8E@2000K

!#8
 c2h3cho=c2h3+hco                0.2003E+25     -2.1400  0.1034E+06

!#9
```

```
 c6h10-15+mb4j=md9d6j            0.8800E+04      2.4800  0.6130E+04
 c6h10-15=2c3h5                  0.2500E+17      0.0000  0.7100E+05


!-- extra reactions --
 md9d+o=md9d6j+oh                0.5946E+06      2.4400  0.2846E+04
 md9d+c2h3=md9d6j+c2h4           0.4000E+12      0.0000  0.1680E+05

!-- ms7j --
! md9d=ms7j+c3h5                  0.2500E+17      0.0000  0.7100E+05
! md9d=ms7j+c3h5                  0.2500E+16      0.0000  0.7100E+05 !0.1A
! c2h4+mf5j=ms7j                  0.8800E+04      2.4800  0.6130E+04
!-----------------combo
! md9d=c2h4+mf5j+c3h5              0.2500E+17      0.0000  0.7100E+05 !jlb
 md9d=c2h4+mf5j+c3h5              0.6250E+16      0.0000  0.7100E+05
!highT: 0.25A

! ms7j+o2=ms6d+ho2                0.1600E+13      0.0000  0.5000E+04
! ms6d+h=ms7j                     0.2500E+12      0.5100  0.2620E+04

!-- ms6d --
 md9d6j=c3h5+ms6d                0.3310E+14      0.0000  0.2146E+05
! md9d6j=c3h5+c3h5+mb4j          0.3310E+14      0.0000  0.2146E+05
!combo/HCCI

 md9d=c3h6+ms6d                  0.3980E+13      0.0000  0.5763E+05

 ms6d=c3h5+mb4j                  0.2500E+17      0.0000  0.7100E+05


!====================================================================
! connect MD & MD9D mechanisms
!====================================================================

 ch2co+mf5j=ms6oxo7j             0.1510E+12      0.0000  0.4810E+04


 mf5j+o2=mf5o2                   0.4520E+13      0.0000  0.0000E+00

 mf5o2=mf5ooh3j                  0.2500E+11      0.0000  0.2085E+05

! mf5ooh3j+o2=mf5ooh3o2           0.7540E+13      0.0000  0.0000E+00
! mf5ooh3o2=mfket53+oh            0.2500E+11      0.0000  0.2140E+05
!------------------------combo
 mf5ooh3j+o2=mfket53+oh          0.7540E+13      0.0000  0.0000E+00 !jlb

! mfket53=oh+mfket53o             0.1050E+17      0.0000  0.4160E+05
! ch2cho+mp3oxo=mfket53o          0.3330E+11      0.0000  0.6397E+04
!-------------------------combo
 mfket53=oh+ch2cho+mp3oxo        0.1050E+17      0.0000  0.4160E+05 !jlb
```

```
! mp3oxo+oh=mp3oxo3j+h2o           0.2690E+11      0.7600  -.3400E+03
! co+me2j=mp3oxo3j                 0.1510E+12      0.0000  0.4810E+04
!-------------------------combo
 mp3oxo+oh=co+me2j+h2o            0.2690E+11      0.7600  -.3400E+03 !jlb


 c2h4+me2j=mb4j                   0.2000E+12      0.0000  0.7600E+04

 ch2co+ch3o=me2j                  0.5000E+12      0.0000  -.1000E+04


!-- important ch2cho reaction --
 ch2cho+o2=ch2o+co+oh             0.2000E+14      0.0000  0.4200E+04
!replace MB rate


end
```